NEUTRAL PION PRODUCTION IN p+p AND d+Au COLLISIONS AT RHIC

by

ALEXANDER STOLPOVSKY

DISSERTATION

Submitted to the Graduate School

of Wayne State University,

Detroit, Michigan

in partial fulfillment of the requirements

for the degree of

DOCTOR OF PHILOSOPHY

2005

MAJOR: PHYSICS (Nuclear)

Approved by:

_____
Advisor   Date

_____

_____

_____

DEDICATION

To my mother for teaching me to see the beauty of physics,

and to my father, who taught me to hear the elegance of music.

ACKNOWLEDGEMENTS

LIST OF TABLES

LIST OF FIGURES

CHAPTER 1

INTRODUCTION

The *standard model* postulates that matter is made of leptons, quarks, and force mediators. Quarks and leptons are elementary particles with spin 1/2. There are three generations of these fundamental fermions (Table 1.1). Each generation contains a charged lepton (e, μ, or τ), the corresponding neutrino, which only interacts weakly, and a pair of strongly interacting quarks. Quarks carry *color*, a property that plays the role of "charge" in the strong interaction. The theory that describes the forces between colored objects and is thought to be the correct theory of strong interactions is called quantum chromodynamics (QCD). In QCD, just as the electromagnetic force is carried by photons which couple to charge, the color force (or strong force) is the result of the exchange of colored massless vector gluons that couple to colored quarks. Figure 1.1a shows a lowest order Feynman diagram for the annihilation process $q\bar{q} \rightarrow q\bar{q}$. Each vertex in the diagram contributes a factor of $\sqrt{\alpha_s}$ to the scattering matrix element. Processes occurring on smaller distance scales, e.g. $g \rightarrow q\bar{q} \rightarrow g$ fluctuation (Figure 1.1b), can be resolved by using higher energy probes. Higher order diagrams result in non-negligible contributions to the scattering matrix element and create divergencies in the perturbative calculation. The strong coupling constant, α_s is a *running constant* dependent on the energy scale of the interaction:

$$\alpha_s(Q^2) \simeq \frac{\alpha_s}{1 + (\alpha_s b_0/4\pi)\log(Q^2/\mu^2)} \equiv \frac{1}{(b_0/4\pi)\log(Q^2/\Lambda^2)} \qquad (1.1)$$
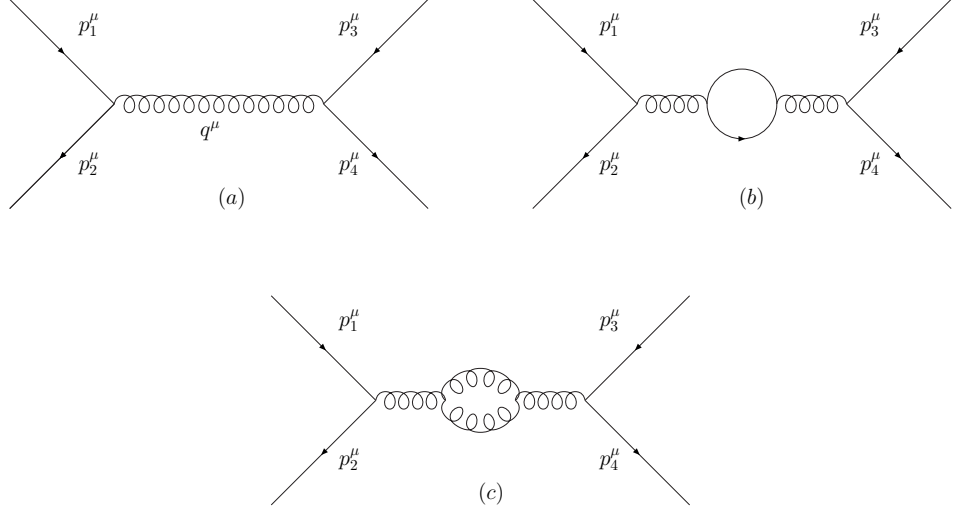
Figure 1.1: Feynman diagram for $q\bar{q} \to q\bar{q}$ annihilation (a) and some lowest order corrections to quark-gluon coupling (b), (c). Momentum conservation requires $(p_1^\mu + p_2^\mu)^2 = (p_3^\mu + p_4^\mu)^2 = q^2 \equiv -Q^2$. Each vertex contributes a factor of $\sqrt{\alpha_s}$ to the matrix element.

$$\Lambda^2 \equiv \mu^2 \exp\left(-4\pi/\alpha_s b_0\right) \tag{1.2}$$

where $Q^2 \equiv -q^2$, q is a four-momentum transfer between the interacting particles, μ^2 is the value of Q^2 at which α_s is measured, and $b_0 \equiv \frac{11}{3}N_c - \frac{2}{3}N_f$ where N_c is the number of colors ($= 3$) and N_f is the number of flavors of quark ($= 6$) [1]. Parameter Λ in Eq. 1.2 defines the "scale" in QCD. The strong coupling constant becomes small at large values of momentum transfer ($\alpha_s \to 0$ as $Q^2 \to \infty$), which implies that quarks and gluons appear almost like free particles when looked at with very high-energy probes, an effect known as *asymptotic freedom*. This behavior is exactly opposite of that observed in quantum electrodynamics (QED) where coupling constant e^2 increases as $Q^2 \to \infty$.

Unlike photons that are electrically neutral, gluons carry color charge so they can interact directly with each other (Figure 1.1c). An important consequence of the gluon-gluon coupling is that α_s increases as the separation between the quarks becomes larger. The quarks are confined to a small (1 fm^3) region in colorless groups

of two (mesons) or three (baryons). This is because the exchanged gluons attract each other, and the color lines of force are constrained to a tube-like region between the quarks. These gluon flux tubes have a constant energy density per unit length, so the potential energy of the interaction increases with the separation, and the quarks (gluons) can never escape the confining hadron, an effect known as *color confinement.*

	Quarks							Leptons	
Flavor	Mass (GeV)[1]	Q	S	C	B	T		Mass (GeV)	Q
Down, d	0.008	$-\frac{1}{3}$	0	0	0	0	e^-	0.0005	-1
Up, u	0.004	$+\frac{2}{3}$	0	0	0	0	ν_e	$< 3 \cdot 10^{-9}$	0
Strange, s	0.15	$-\frac{1}{3}$	-1	0	0	0	μ^-	0.105	-1
Charm, c	1.2	$+\frac{2}{3}$	0	1	0	0	ν_μ	< 0.00019	0
Bottom, b	4.7	$-\frac{1}{3}$	0	0	-1	0	τ^-	1.8	-1
Top, t	174	$+\frac{2}{3}$	0	0	0	1	ν_τ	< 0.018	0

Table 1.1: The flavor quantum numbers of three different generations of quarks and leptons. Q, S, C, B, T are charge, strangeness, charm, beauty and truth. Free quarks are not seen and the mass represents the current quark mass felt via electromagnetic or weak interactions. All quarks and leptons have antiparticles (with opposite Q, S, ...). Each flavor of quark comes in three colors (red, green, blue).

Perturbation theory can be used to calculate QCD processes only when the effective coupling constant is small, a regime achieved in reactions involving large momentum transfers (*hard processes*). Hard-scattered quarks and gluons (partons) carrying a color charge will fly apart with a large relative momentum. Due to color confinement, these partons will result in two back-to-back jets of hadrons. Perturbative QCD (pQCD) is in excellent agreement with experimental data from hard processes as shown in Figure 1.2.

The behavior of colored objects, in the regime where pQCD is not a valid approximation, can be understood in the framework of numerical path integrals of the QCD Lagrangian on a discretized lattice in four-dimensional Euclidian space-time.

---

[1] Throughout this dissertation, the system of units is used in which the speed of light is a dimensionless quantity equal to unity.
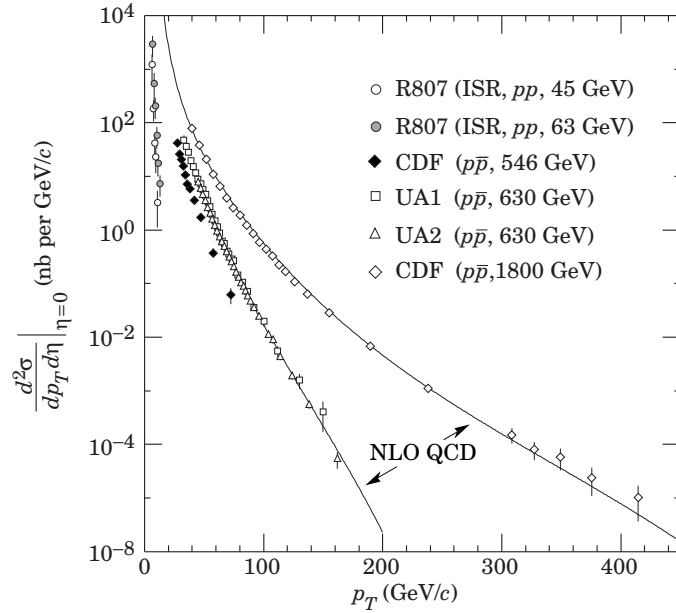
Figure 1.2: Differential cross sections for the observation of a single jet of pseudo-rapidity $\eta = 0$ as a function of the transverse momentum of the jet. The lines through the data are next-to-leading order (NLO) QCD curves for 630 GeV and 1800 GeV p+$\bar{\text{p}}$ collisions. Figure taken from the Particle Data Book [2].

Lattice QCD can be used to perform numerical calculations for all physics regimes. However there are regimes where approximations used to simplify the calculations fail and computations become technically extremely challenging.

Deconfined quarks have never been observed because the force between colored objects increases linearly with the distance between them. A deconfined quark is one that can move in a volume much larger than that of a proton. QCD predicts that at sufficiently large temperature and density a regime can be reached where quarks and gluons become deconfined, so that color degrees of freedom become manifest over *nuclear*, rather than merely nucleonic, volumes.

The new state of matter where quarks and gluons are deconfined, was suggested to exist within the cores of neutron stars [3]. A neutron has a density of about 1×10^{14} g/cm^3, whereas the density in the center of a neutron star can be as much as $10^{16} - 10^{17}$ g/cm^3 [3]. In this case hadrons overlap and the nuclear matter may become a quark-gluon plasma or QGP. While the high energy experiments with hadron

beams are capable of creating conditions in which quarks, gluons and various symmetries of QCD reveal themselves, high energy nuclear experiments add the additional condition of high density. The behavior of nuclear matter at high temperature and density is especially interesting because the combination of high energy density and high temperature can lead to the formation of QGP.

The Relativistic Heavy-Ion Collider (RHIC) was built with the aim of creating and studying bulk matter made of deconfined quarks and gluons. The temperature and density in high energy heavy-ion collisions are expected to be similar to those that prevailed in the early universe, before the protons and neutrons were formed. The study of the properties of the matter created in these collisions enables physicists to answer important questions of nuclear physics, astrophysics and high-energy physics.

As hard-scattered partons propagate through hot and dense medium, they lose energy via gluon radiation at a rate proportional to the gluon density in the medium. Fragmentation of hard-scattered partons gives rise to production of particles with large transverse momenta (p_T). These high p_T particles can be used to probe the density of the medium produced in relativistic heavy-ion collisions. In addition, results from inclusive neutral pion (π^0) production may provide meaningful constraints on the gluon-to-pion fragmentation [4]. Transverse momentum dependence of the ratio of π^0 yield in p+p to that in d+Au is important for understanding how π^0 yield scales with the number of nucleons participating in the collision. This understanding is essential for disentangling the initial and final state effects of the A+A collisions.

This dissertation presents the analysis of the experimental data taken by the STAR detector at RHIC during the years 2003 and 2004 (experimental runs 3 and 4). Transverse momentum dependence of neutral pion yield is measured in proton-proton (p+p) and deuteron-gold (d+Au) collisions at center-of-mass energy per nucleon $\sqrt{s_{NN}} = 200$ GeV.

The remainder of the dissertation is organized as follows. In Chapter 2, the un-

derlying physics is discussed in more detail. In Chapter 3, the experimental setup is presented with the emphasis on the STAR Barrel Electromagnetic Calorimeter (BEMC). The data analysis methods and results are presented in Chapter 4. Chapter 5 is dedicated to the discussion of the experimental results.

CHAPTER 2

PHYSICS

In this chapter we give a brief review of the QCD treatment of large p_T processes. We continue with a discussion of the theoretical models incorporating nuclear medium effects that affect high p_T particle production in nuclear collisions. In connection to the results on π^0 production, presented in this dissertation, we give a motivation for this analysis along with a review of earlier experimental measurements.

2.1 Perturbative QCD, Structure Functions, and Fragmentation Functions

Since hadrons are made of partons (quarks and gluons), it must be possible to describe hadronic interactions in terms of the interactions of their constituent partons. This approach is most useful for those reactions in which the parton scattering is separated in time from the more complex confinement effect. Such conditions are satisfied in hadronic reactions where a hadron with large momentum p_T in the direction transverse to the beam axis is produced.

The basic diagram for $AB \rightarrow CX$, where C is a hadron with large p_T (say $p_T > 2$ GeV) while X represents all the other particles in the final state, is shown in Figure 2.1 [1]. The incoming hadrons A and B contain partons a and b which scatter and produce partons c and d which have a large transverse momentum component q_T. Large q_T implies short interaction distance, and therefore small α_s, so the perturbative approach is applicable. Hadron C is produced from c via the confinement mechanism.
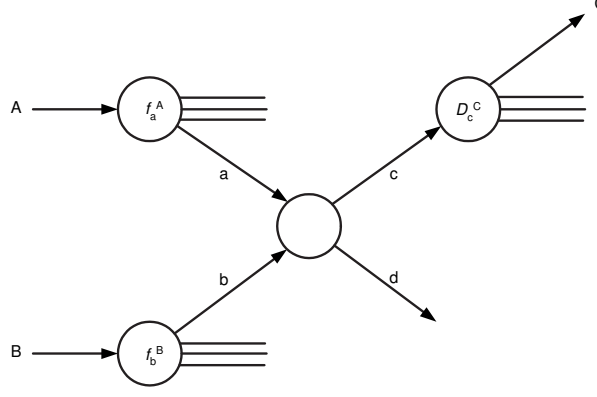
Figure 2.1: Hadronic interaction $AB \to CX$ in terms of the parton sub-process $ab \to cd$, the structure functions f_A^a, f_B^b, and the fragmentation function D_c^C.

The *structure functions*[1] $f_A^a(x_a)$ of A are defined as the probability that hadron A contains a parton a which is carrying a fraction $x_a = q_a/p_A$ of the hadron momentum p_A, $0 \le x_a \le 1$. Similarly, the *fragmentation functions* $D_c^C(z_C)$ are defined as the probability that a parton c produces a hadron C carrying a momentum fraction $z_c = p_C/q_c$, $0 \le z_c \le 1$.

Using the formalism introduced above, the invariant cross-section for $AB \to CX$ can be expressed as the weighted sum of differential cross-sections, $d\sigma/d\bar{t}$ of all possible parton scatterings that can contribute:

$$E_C \frac{d\sigma_{AB \to CX}}{d^3 p_C} = \sum_{abcd} \int_0^1 dx_a \int_0^1 dx_b f_A^a(x_a) f_B^b(x_b) \frac{1}{\pi z_c} \frac{d\sigma_{ab \to cd}}{d\bar{t}} D_c^C(z_c), \qquad (2.1)$$

where $\bar{t} \equiv (q_a - q_c)^2$ is the invariant momentum transfer from parton a to parton c [1]. Given the structure functions, the fragmentation functions, and the cross-sections for all the parton sub-processes, cross-section (Eq. 2.1) can be calculated for any given hadronic reaction.

However, *scaling violation* complicates matters by introducing the Q^2 dependence of fragmentation functions and structure functions. The origin of this behavior is

---

[1]The *structure functions* are frequently referred to as *"parton distribution functions"*.

similar to that responsible for α_s being a logarithmically decreasing function of Q^2 (Eq. 1.1). The result,

$$\alpha_s(Q^2) = \frac{4\pi}{b_0 \log{(Q^2/\Lambda^2)}} \ , \tag{2.2}$$

depends on the scale parameter Λ, which determines when α_s becomes large and results in the confinement of quarks within hadrons.

Similarly, the distributions of partons within a hadron, determined by the structure functions $f_A^a(x_a)$, will depend on the resolving power of the probe with which these distributions are measured. At higher Q^2 one becomes sensitive to finer details of the probed structure, e.g. brief fluctuations of gluons into quark-antiquark pairs. The effective number of partons seen by the probe depends on Q^2. *Factorization* is a procedure that sets an arbitrary scale, separating the regimes governed by the structure functions (non-perturbative soft regime) and hard scattering (pQCD regime). Once the structure functions are known at a given scale μ, pQCD enables their prediction for any other scale μ', as long as both μ and μ' are large enough so that both $\alpha_s(\mu)$ and $\alpha_s(\mu')$ are small. The Q^2 dependence of structure functions is called the *evolution of structure functions*, and allows pQCD predictions to be tested at different energies.

Perturbative description is not applicable to the soft processes responsible for the momentum distributions of partons within a hadron. Therefore, the structure functions cannot be calculated theoretically and must be determined from experiments. Structure functions of nucleons are determined in deep inelastic lepton-nucleon scattering processes such as $eA \rightarrow eX$, $\mu A \rightarrow \mu X$, $\nu_\mu A \rightarrow \mu^- X$ and $\bar{\nu}_\mu A \rightarrow \mu^+ X$ with large momentum transfer between the lepton and the nucleon, A. Figure 2.2 shows proton structure functions from the CTEQ (Coordinated Theoretical-Experimental Project on QCD) collaboration [5] at two different scales $Q = 2$ GeV and 100 GeV. It is evident that the proton structure is dominated by gluons at $x \lesssim 10^{-1}$.

The fragmentation of partons, produced at short distance of order $1/Q$, into
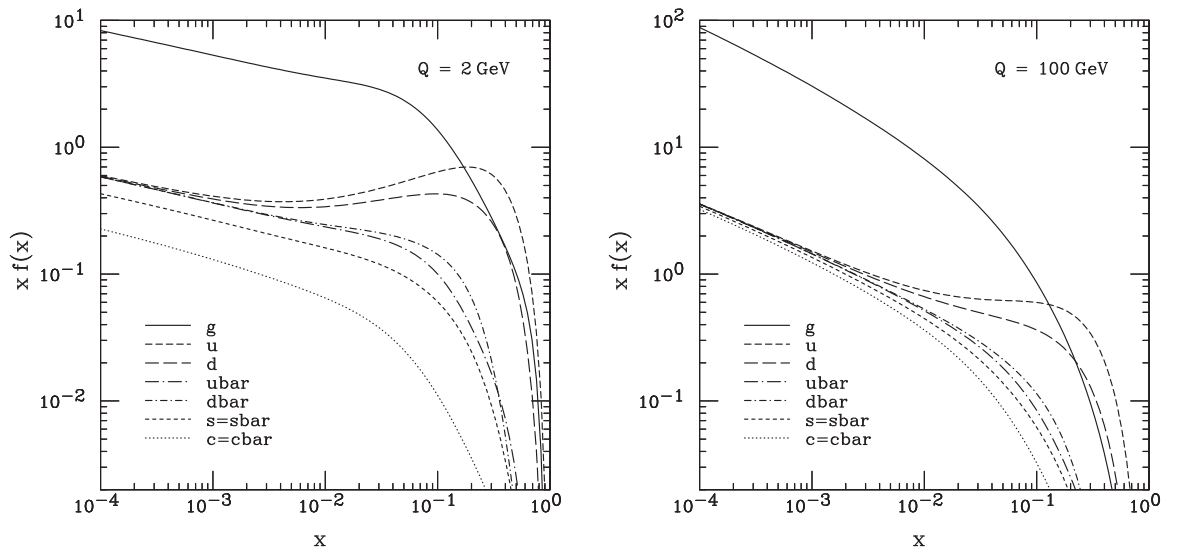
Figure 2.2: CTEQ6M proton structure functions evaluated at $Q = 2$ GeV and 100 GeV.

hadrons, is described by the fragmentation functions $D_c^C(z_c)$. This process is inverse to that described by the structure functions. Here one essentially evaluates the distribution of hadrons *within* a parton [6]. The fragmentation function $D_c^C(z_c)$ has the interpretation of a probability density that some final state parton c fragments into a mean number $D_c^C(z_c)dz_c$ of hadrons C per dz_c [7]. Hadronization occurs at the energy scale ~ 1 GeV, which is too small for the perturbative treatment to be valid. An approach, very similar to that developed for the structure functions (computation of *evolution* by applying *factorization*), applies to the fragmentation functions as well. Given the z dependence at some scale Q_0^2, the evolution of the fragmentation functions with Q^2 can be calculated perturbatively and is determined by the DGLAP equations [8, 9, 10].

The inclusive production of a single charged hadron, h, in the annihilation process

$$e^+e^- \to (\gamma, Z) \to hX, \qquad (2.3)$$

is especially suitable in order to study the fragmentation of quarks and gluons into hadrons. Here, h may either refer to a specific hadron species, e.g., pion, kaon, or proton, or to the sum over all charged-hadron species. The information from fixed-target, hadron-collider, and *ep*-scattering experiments is less useful, since it is obscured by theoretical uncertainties from the parton distribution functions and the choice of factorization scales connected with the initial states [11]. Hadron production has been measured at many different e^+e^- colliders over a wide range of center-of-mass energies between 3 and 183 GeV [12, 13].

The partonic cross sections pertinent to process (Eq. 2.3) can be entirely calculated in perturbative QCD with no additional input, except for the strong coupling constant α_s [11]. They are known at next-to-leading order (NLO) [14] and next-to-next-to-leading order (NNLO) [15].

Typically, the z dependence of the fragmentation functions at Q_0^2 is parametrized as

$$D(z, Q_0^2) = N z^\alpha (1 - z)^\beta, \tag{2.4}$$

where parameters N, α, and β are determined from fits to the experimental data (Figure 2.3). According to the *factorization theorem*, the fragmentation functions are independent of the process in which they have been determined. They can be used for quantitative predictions of inclusive single hadron cross sections in other processes, like $p\bar{p}$, ep, γp, and $\gamma\gamma$ scattering.

The partonic cross sections for the basic $ab \to cd$ sub-process of Figure 2.1 can be calculated in perturbative QCD. The leading order diagrams are shown in Figure 2.4.

The upshot of the preceding ultra-compact review of the pQCD treatment of the hadronic process $AB \to CX$, is that the *scaling violations* can be included in a very simple and elegant way. Eq. 2.1 now takes the form:

$$E_C \frac{d\sigma_{AB \to CX}}{d^3 p_C} = \sum_{abcd} \int_0^1 dx_a \int_0^1 dx_b f_A^a(x_a, Q^2) f_B^b(x_b, Q^2) \frac{1}{\pi z_c} \frac{d\sigma_{ab \to cd}}{d\bar{t}} D_c^C(z_c, Q^2), \tag{2.5}$$

where the parton distributions are those measured in deep inelastic lepton scattering experiments, and the Born diagrams of Figure 2.4 (and higher orders) are used to calculate the hard-scattering amplitudes for the partonic sub-process $ab \to cd$.

2.2 High p_T particle ratios

High p_T hadrons created in relativistic heavy ion collisions arise from fragmentation of quarks and gluons (partons) scattered with large momentum transfer, Q^2, in initial parton-parton interactions [19]. In the absence of nuclear medium effects, a collision of two nuclei would look like a superposition of nucleon-nucleon collisions [20]. High p_T particle yields in nuclear collisions would be the same as those in p+p
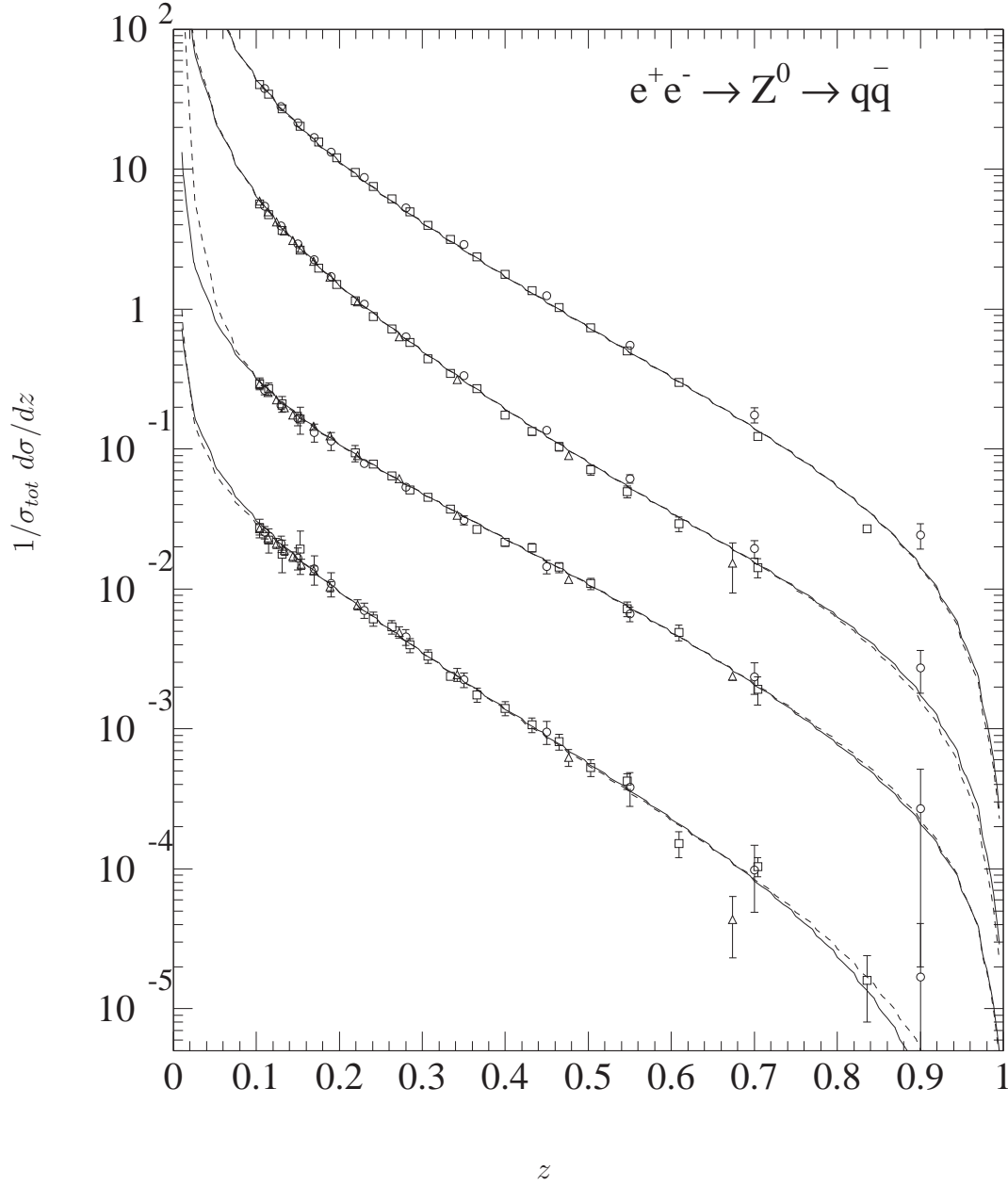
Figure 2.3: Normalized differential cross section of inclusive hadron production at $\sqrt{s} = 91.2$ GeV as a function of z. The LO (dashed lines) and NLO (solid lines) fit results are compared with data from ALEPH [16] (triangles), DELPHI [17], and SLD [18]. The upmost, second, third, and lowest curves refer to charged hadrons, $\pi^{\pm}$, $K^{\pm}$, and $p/\bar{p}$, respectively. Each pair of curves is rescaled relative to the nearest upper one by a factor of 1/5. Figure taken from [11].
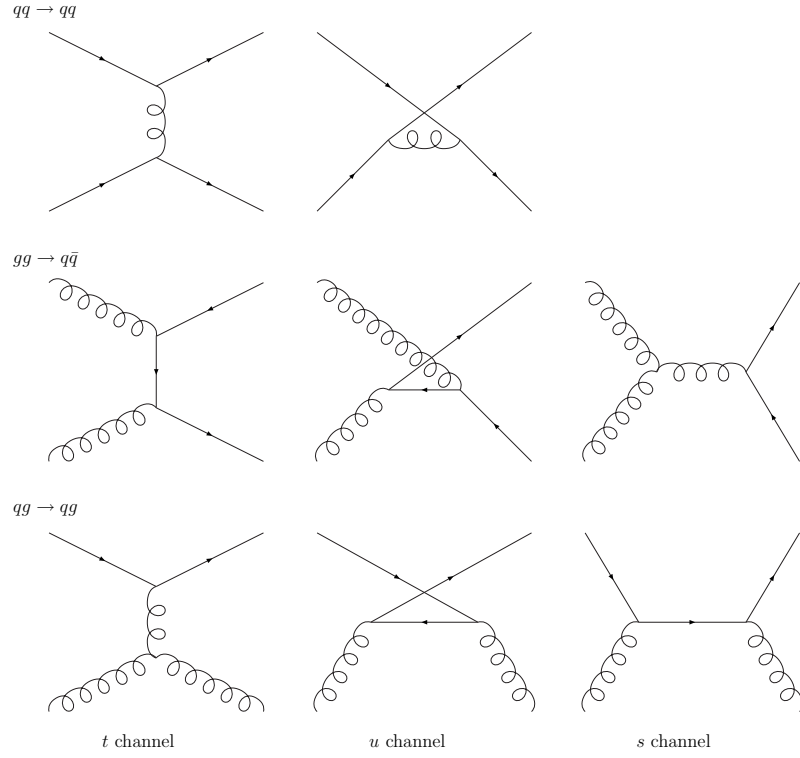
Figure 2.4: Leading order QCD diagrams for $qq \rightarrow qq$, $gg \rightarrow q\bar{q}$, and $qg \rightarrow qg$. The process $q\bar{q} \rightarrow q\bar{q}$ has an s channel, but no u channel contribution. In addition, there are $gg \rightarrow gg$ diagrams.

collisions (neglecting the isospin effects responsible for the difference between protons and neutrons), scaled by the average number of inelastic nucleon-nucleon collisions (binary scaling). One of the most interesting results from the experiments at the BNL Relativistic Heavy Ion Collider is the significant suppression of high p_T particle yields in Au+Au collisions compared to p+p collisions at the same center-of-mass energy, scaled with the number of binary collisions [21, 22, 23, 24].

Gyulassi and Plumer [25] argue that as partons propagate through the hot and dense matter created in nuclear collisions, they lose energy via gluon radiation (gluon bremsstrahlung). This process is also known as *jet quenching*. Theoretical calculations predict this energy loss (dE/dl) to be in the range of 1 to 3 GeV/fm [26]. In the context of this model, high p_T partons lose a significant portion of their momenta in the medium, resulting in suppression of high p_T hadron yields. Jet quenching is of great interest because it is sensitive to the final-state interactions, that may lead to thermal and chemical equilibrium in the produced dense partonic system, and provides a direct measure of the gluon density [25, 27].

Hard processes responsible for high-p_T parton production are also sensitive to initial state nuclear effects. A nucleon has contributions to its wavefunction from the constituent partons (gluons, quarks, and antiquarks). Each parton carries a fraction x of the momentum of the nucleon. Inelastic cross-sections, obtained from scattering of leptons off target nuclei, can be used to derive the individual parton distribution functions. Results from inelastic lepton-nucleus scattering experiments are typically presented as a ratio of lepton-nucleus cross section per nucleon for different nuclei relative to that for deuterium. Deuterium is used as a reference in order to average out the effects of the isospin on the nuclear structure function. A change in the ratio of nuclear structure functions implies a change in the underlying parton distributions, which has a direct impact on the particle production.

Transverse momentum of the leading hadron, produced by the fragmentation of

the hard-scattered parton, can be estimated by

$$x \approx \frac{2p_T}{\sqrt{s_{NN}}}, \qquad (2.6)$$

where x is the fractional momentum of the parton (derivation is given in Appendix A.3). At RHIC energy $\sqrt{s_{NN}} = 200$ GeV and particle transverse momenta up to 10 GeV the region $x < 0.1$ is most important. It is known from deep-inelastic scattering experiments that the quark structure functions with small fractional momenta ($x < 0.1$) are suppressed in a nucleus compared to a free nucleon [28]. This depletion (Figure 2.5), known as *nuclear shadowing*, leads to suppression of high p_T single-particle inclusive spectra.

One explanation of nuclear shadowing, offered by Arneodo et al. [28], is that shadowing arises because, at small x, partons from different nucleons overlap in space and interact, leading to a redistribution of parton momenta. Nuclear shadowing is of interest because it significantly influences the initial conditions in high-energy nucleus-nucleus collisions.

Another initial state process that affects high p_T particle yield is soft scattering of the incident parton prior to its hard scattering, usually referred to as the *Cronin effect*. It was first shown by Cronin et al. in 1974 that cross sections measured in p+A collisions do not simply scale with the number of target nucleons A, when compared to p+p collisions [29]. Cronin et al. parametrized the observed p_T dependence of the cross section by introducing the exponent α:

$$E\frac{d^3\sigma}{dp^3}(p_T, A) = E\frac{d^3\sigma}{dp^3}(p_T, 1) \cdot A^{\alpha(p_T)}. \qquad (2.7)$$

It was found that for cross sections measured for several different particles, the exponent α is greater than unity above $p_T \sim 2$ GeV (Figure 2.6).

Both nuclear shadowing and jet quenching result in the suppression of single-
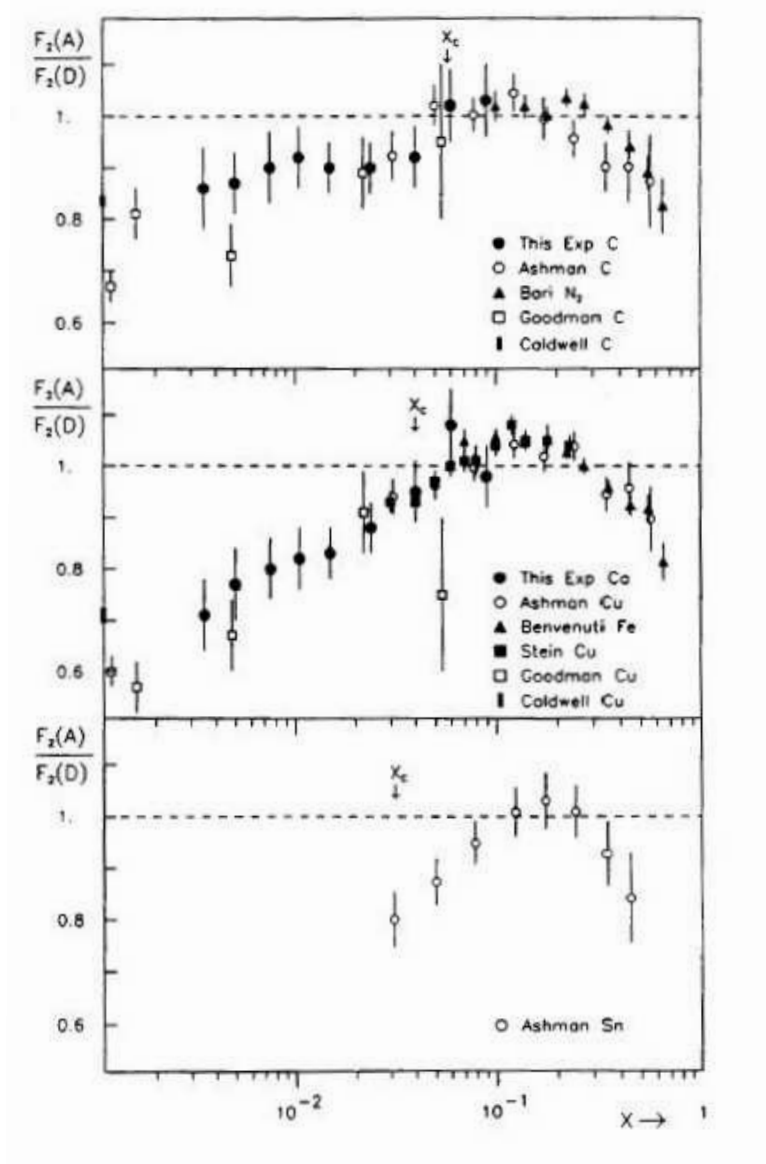
Figure 2.5: Structure function ratios for different nuclei, and for $0.3 < Q^2 < 3.2\,\mathrm{GeV^2}$, as a function of fractional momentum x. Figure is taken from [28] and combines data from several high-energy charged lepton scattering experiments.
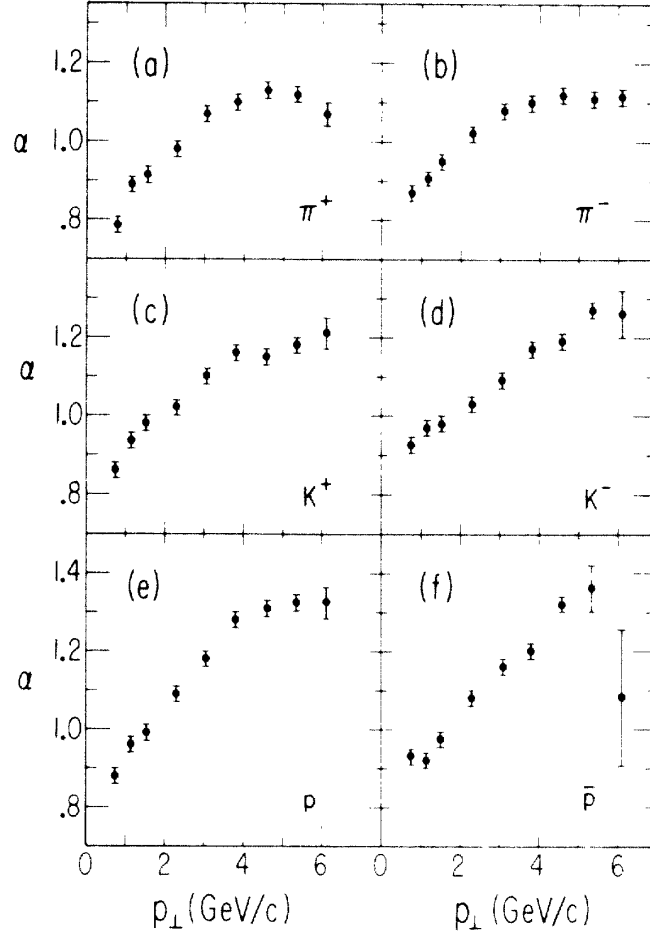
Figure 2.6: Plots of the power α of the A dependence versus p_T for the production of hadrons by 300-GeV protons; (a) π^+, (b) π^-, (c) K^+, (d) K^-, (e) p, and (f) $\bar{\text{p}}$

particle inclusive spectra. A vital question for the interpretation of the experimental nucleus-nucleus (A+A) data is whether suppression of high p_T hadrons is due to the initial or final state effects. In order to disentangle and quantitatively describe these effects, it is necessary to create experimental conditions in which one class of effects is present while the other is not. Such conditions can indeed be satisfied in proton-nucleus (p+A) and deuteron-nucleus (d+A) collisions. Initial state effects, including nuclear modifications to the parton structure functions and soft scatterings, should be present in p+A, d+A and A+A collisions, whereas only high p_T partons resulting from A+A collisions are subject to the final-state jet quenching. Hence, to gain access to information about jet quenching from high-energy A+A collisions, it is imperative to experimentally determine the modification (if any) of high p_T hadron yields due to initial-state nuclear effects for a system in which a hot, dense medium is not produced in the final state [20]. The absence of such modification would indicate that the observed suppression in high p_T particle yields in A+A collisions is due to jet quenching, providing important information about the system produced.

Medium effects on high p_T production in d+Au collisions are quantified by the modification factor R_{dA} defined as a ratio of invariant yield measured in d+Au and p+p as follows:

$$R_{dA}(p_T) = \frac{(1/N_{dA}^{evt})d^2 N_{dA}/d\eta dp_T}{\left(\langle N_{coll}\rangle/\sigma_{pp}^{inel}\right) \times d^2\sigma_{pp}/d\eta dp_T}, \tag{2.8}$$

where $\langle N_{coll}\rangle$ is the average number of inelastic nucleon-nucleon collisions per event in d+Au minimum bias collisions, and $\langle N_{coll}\rangle/\sigma_{pp}^{inel}$ is the nuclear overlap function $\langle T_{dA}(b)\rangle$. Using a Glauber model $\langle N_{coll}\rangle$ is 7.5 ± 0.4 in minimum bias d+Au collisions [20].

The inclusive charged hadron yield in d+Au measured by the STAR collaboration [30] indicates that there is no suppression of high p_T particles relative to binary-scaled p+p collisions (Figure 2.7). The enhancement at $p_T > 2$ GeV is due to *Cronin effect*,
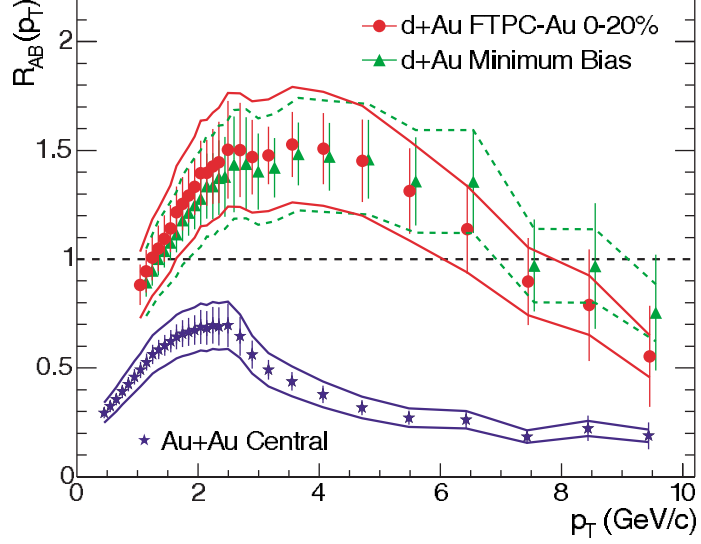
Figure 2.7: $R_{AB}(p_T)$ for minimum bias and central d+Au collisions, and central Au+Au collisions. The minimum bias d+Au data are displaced 100 MeV/c to the right for clarity. The bands show the systematic normalization uncertainties.

and was observed in earlier p+A experiments [31].

2.3   Neutral Pions

The invariant cross section for a given process is an important observable to help establish the dynamical origin of particle production [32].   One of the most well-defined and understood hadronic interactions is the production of neutral pions from p+p collisions.   In this reaction the simplest possible (stable) hadronic target and projectile react and form the simplest possible hadronic product (π^0).   For experimental reasons the outgoing pion can be measured over a wider energy range than any other particle, thus providing a commensurably larger kinematic range for comparison with theory.   The history of pion cross section measurements and their comparison with theory is illustrated in Figure 2.8.   These data, spanning some 11 orders of magnitude, summarize the results from major proton experiments over the past 25 years.   The center-of-mass energy of these experiments increases an order of magnitude from about 20 GeV to 200 GeV. While next-to-leading order perturbative QCD

(NLO pQCD) calculations underpredict the measured π^0 production cross section by nearly an order of magnitude for the lowest center-of-mass energy $\sqrt{s} = 19.4$ GeV, the agreement becomes increasingly better at higher $\sqrt{s}$.

The ratio Data/Theory suggests that at lower $\sqrt{s}$, the neutral pion production mechanism is dominated by soft processes. The relative size of the soft contributions increases in the forward direction, where the disagreement between data and pQCD gets larger [33]. However, the neutral pion cross section at large rapidity in $\sqrt{s} = 200$ GeV p+p collisions measured by STAR (Figure 2.9) is in a good agreement with the NLO pQCD calculation. This agreement suggests that particle production at large forward rapidity at $\sqrt{s} = 200$ GeV is predominantly due to partonic scattering, rather than soft mechanisms presumed responsible for beam fragmentation.

The ratio R_{dA} for π^0 measured by the PHENIX collaboration (Figure 2.10) shows that there is no suppression of high p_T neutral pion production in d+Au relative to binary-scaled p+p collisions [20]. Thus, final state nuclear medium effects are not present in d+Au collisions. This suggests that the suppression of high p_T particle production, observed in Au+Au reactions, is due to the presence of the hot and dense medium produced in the collisions.
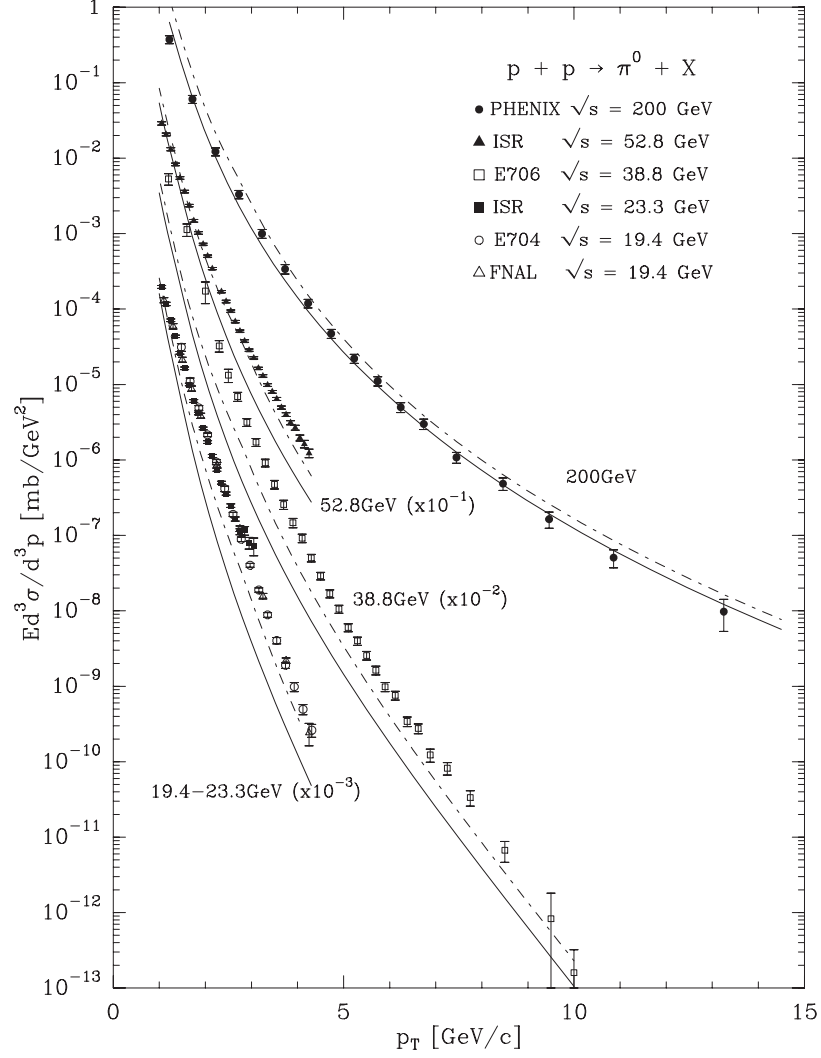
Figure 2.8: $Ed^3\sigma/d^3p$ at 90° and various energies, as a function of p_T. The curves are the corresponding NLO pQCD calculations with $\mu = p_T$ (solid lines) and $\mu = p_T/2$ (dotted-dashed lines), where μ is a factorization scale associated to the running strong coupling constant α_s. Figure taken from [33].
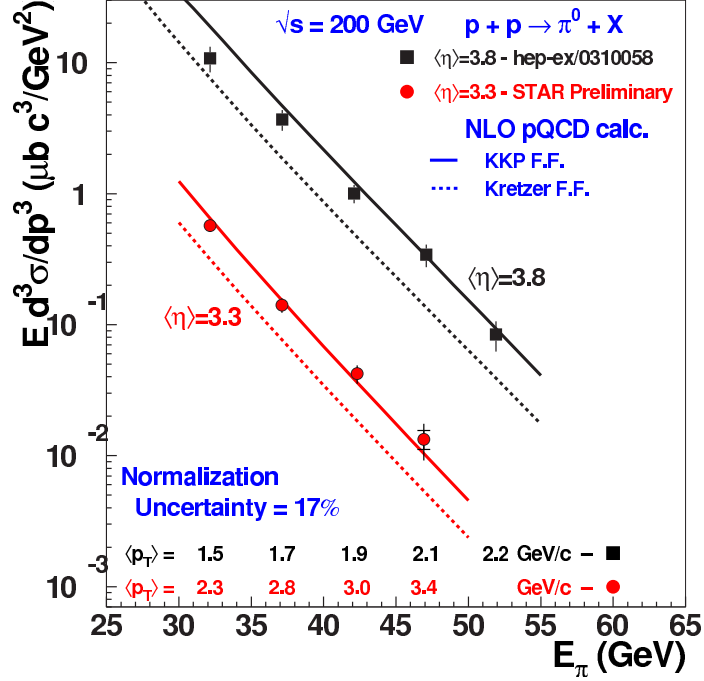
Figure 2.9: Invariant cross section for neutral pions produced in p+p collisions at $\sqrt{s} = 200$ GeV as a function of the average energy of the pion, detected at fixed pseudorapidity by the Forward Pion Detector (FPD) at STAR. Figure taken from [32].
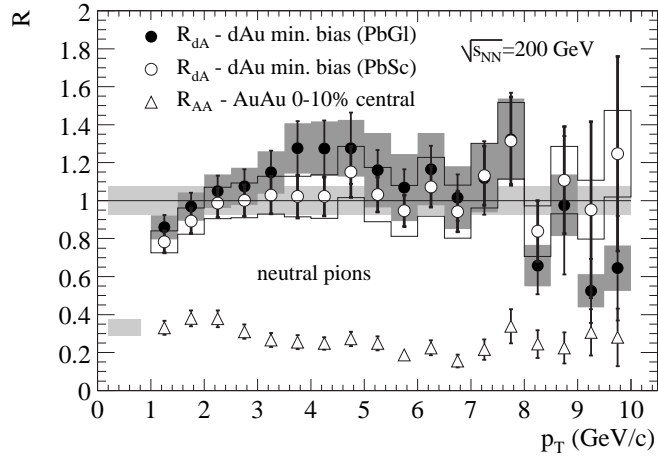
Figure 2.10: R_{dA} for π^0 in the PbGl and PbSc calorimeters in minimum bias d+Au measured by PHENIX collaboration [20]. The bands around data show systematic errors which can vary with p_T, while the shaded band around unity indicates the normalization uncertainty. The nuclear modification factor R_{AA} in 10% most central collisions is also shown.

CHAPTER 3

THE EXPERIMENT

In this chapter we give an overview of the experimental setup that was used to collect the data for the analysis presented in this dissertation. We begin with an overview of the accelerator complex at Brookhaven National Laboratory. In the overview of the STAR detector, we will focus mainly on the Barrel Electromagnetic Calorimeter, which is the key subsystem for π^0 detection. We will conclude this chapter with an overview of the STAR trigger system components essential for π^0 analysis.

3.1   RHIC

The Relativistic Heavy Ion Collider is located at Brookhaven National Laboratory (BNL). It is designed to accelerate and collide two beams of heavy ions, deuterons, protons, or any combination of them. This diversity allows the study of colliding systems as a function of both energy and system size. RHIC characteristics are summarized in Table 3.1.

RHIC is a large step forward in terms of energy per nucleon, compared to previously built machines capable of accelerating beams of heavy ions. The summary of existing and future heavy ion colliders and their key characteristics is given in Table 3.2.

The accelerator complex at BNL, required to produce, accelerate and store the

Physical Parameters		
RHIC circumference (m)	3833.845	
No. Intersection Regions	6	
No. Bunches/ring	60	
Bunch Spacing (nsec)	213	
Collision Angle	0	
Free Space at Crossing Point (m)	± 9	
Performance Specifications	Au	p
No. Particles/Bunch	1×10^9	1×10^{11}
Top Energy (GeV/u)	100	250
Luminosity, average $(cm^{-2}sec^{-1})$	$\sim 2 \times 10^{26}$	$\sim 1 \times 10^{31}$

Table 3.1: Physical parameters and performance specifications for the Relativistic Heavy Ion Collider (RHIC).

	AGS	AGS	SPS	SPS	SPS	RHIC	RHIC	LHC
Start year	1986	1992	1986	1994	1999	2000	2001	2006
A_{max}	^{28}Si	^{197}Au	^{32}S	^{208}Pb	^{208}Pb	^{197}Au	^{197}Au	^{208}Pb
E_P^{max} [GeV]	14.6	11	200	158	40	0.91E4	2.1E4	1.9E7
$\sqrt{s_{NN}}$ [GeV]	5.4	4.7	19.2	17.2	8.75	130	200	6000
$\sqrt{s_{AA}}$ [GeV]	151	934	614	3.6E3	1.8E3	2.6E4	4E4	1.2E6
$\Delta y/2$	1.72	1.58	2.96	2.91	2.22	4.94	5.37	8.77

Table 3.2: RHIC compared to existing and future facilities; A_{max} is the maximum species mass number, E_P^{max} is the maximum (equivalent) fixed-target beam energy per nucleon, $\sqrt{s_{NN}}$ is the maximum center of mass energy, and $\Delta y/2$ is the rapidity gap from the beam to mid-rapidity [34].

heavy ion beam, consists of the Tandem Van de Graaff accelerators, the Booster Synchrotron and the Alternating Gradient Synchrotron (AGS) (Figure 3.1). Gold (Au) atoms with a charge $Q = -1$ are generated in the Pulsed Sputter Ion Source in the Tandem Van de Graaff facility. These negative ions, with charge -1, are accelerated from ground to $+15$ MV potential. They pass through a stripping foil in the high voltage terminal yielding partially stripped ions, with a positive charge, Q_T, which is a function of the element being accelerated. The partially stripped ions are accelerated back to ground potential, increasing their energy by $15 \times Q_T$ MeV. For the gold beams, the ions exit the Tandem at the kinetic energy of 1 MeV/u and with $Q = +12$ charge state. Exiting from the Van de Graaff, the ions are further stripped to charge state $+32$. The Au beam of 1 MeV/u energy is transferred to the booster where it is accelerated to 95 MeV/u. In the Booster-to-AGS (BtA) transfer line, the ions are stripped once again to charge state $+77$ (only K-shell electrons remaining) and then enter the AGS. Four such Tandem/Booster cycles fill the circumference of the AGS. The Booster bunches are injected into matching AGS RF buckets (harmonic number $h = 16$). After the fourth transfer, the beam is accelerated enough to allow a merge from 16 to 8 bunches, accelerated to full energy (10.8 GeV/u for gold), and is merged again from 8 to 4. Each bunch contains 1×10^9 ions. Finally, the beam is extracted into the AGS-to-RHIC (AtR) transfer line. A final stripping from $+77$ to $+79$ takes place at the start of this line. For protons the acceleration strategy is simplified; the merges are unnecessary, since intensity is not a problem. A nominal total of 60 bunches are injected into each collider ring in the bunch-to-bucket fashion. The AGS extraction system allows single-bunch transfer of the four AGS bunches into one of the two collider rings. This cycle is repeated 2×15 times in order to fill each collider ring with 60 bunches. Filling both rings requires about 1 minute. The bunches are captured in stationary buckets of the so-called acceleration RF system operating at 28.15 MHz, corresponding to a harmonic $h = 360$. Then the process of acceleration
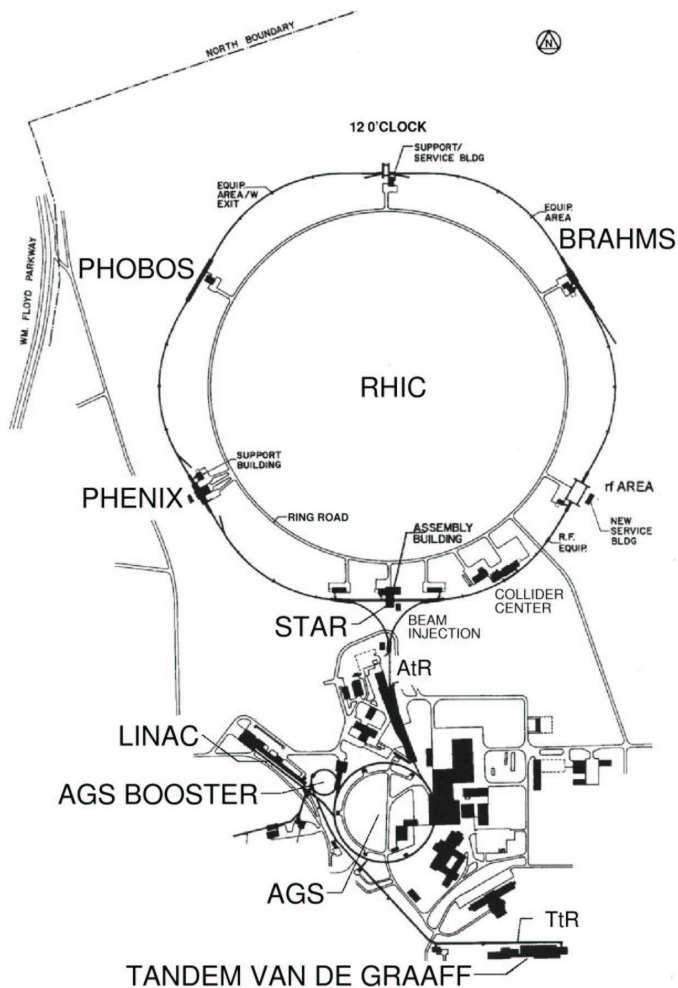
Figure 3.1: Brookhaven National Laboratory collider complex including the accelerators that bring the nuclear ions up to RHIC injection energy (10.8 GeV/u for $^{197}Au^{79}$

begins. After having reached the operating kinetic energy which takes about 1 min, the bunches are transferred from the acceleration (28.15 MHz) to the storage RF system at 197 MHz. The harmonic number of the storage RF is $h = 360 \times 7 = 2520$, resulting in a bucket length of 1.52 m. the resulting RMS diamond length is less than 18 cm. The stored beam lifetime for gold in the energy range of 30 to 100 GeV/u is approximately 10 hours.

RHIC consists of two rings of superconducting magnets (Figure 3.2), each with a circumference of 2.4 miles. The magnets are cooled by circulating liquid helium to a temperature of less than 4.6 K. Extremely good vacuum inside the beam pipes is nec-
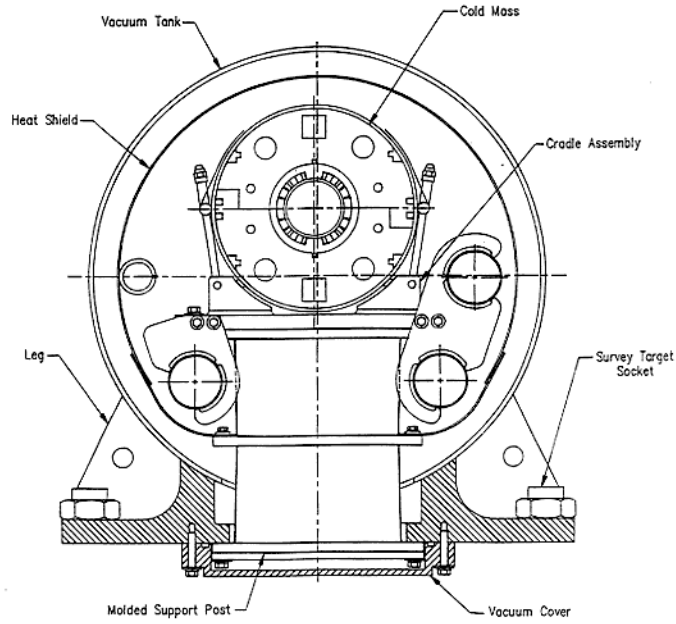
Figure 3.2: Cross section of an arc dipole. The outer diameter of the vacuum vessel is 610 millimeters.

essary to minimize beam losses and radiation background. Vacuums achieved in the cold and warm sections of RHIC are about 10^{-11} mbar and 10^{-10} mbar respectively.

RHIC provides particle collisions at 6 intersection regions located around the collider ring, with 4 of them presently occupied by two large (STAR, PHENIX) and two smaller (BRAHMS, PHOBOS) experiments.

3.2 STAR Detector Overview

STAR stands for "Solenoidal Tracker at RHIC" (Figure 3.3) and gets its name from the large tracking detector (Time Projection Chamber, or TPC) located in the center of the detector. STAR is an azimuthally symmetric, large acceptance, solenoidal detector designed to measure many observables simultaneously in high multiplicity heavy ion collisions. The detector consists of several subsystems, many of which are located inside a 0.5 Tesla solenoidal magnet (Figure 3.4).
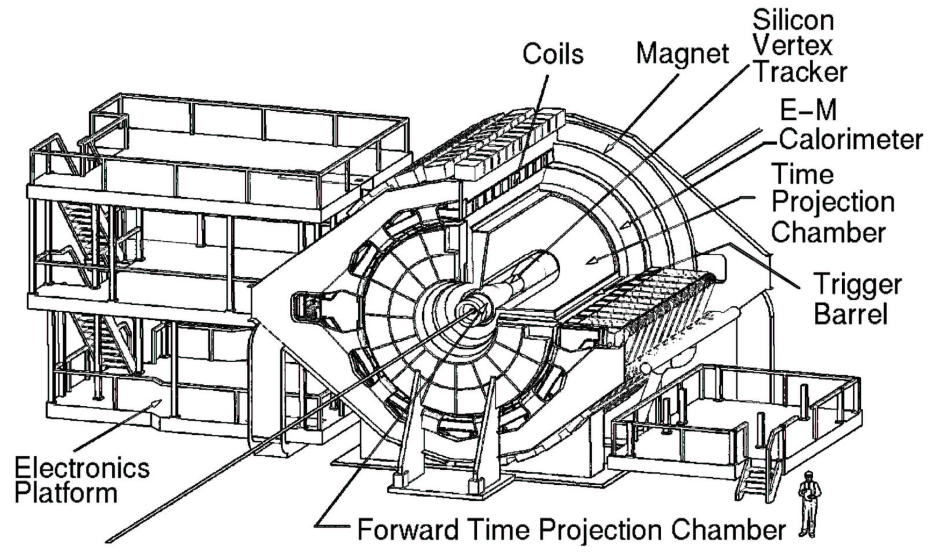
Figure 3.3: View of the STAR detector. Figure taken from [35].
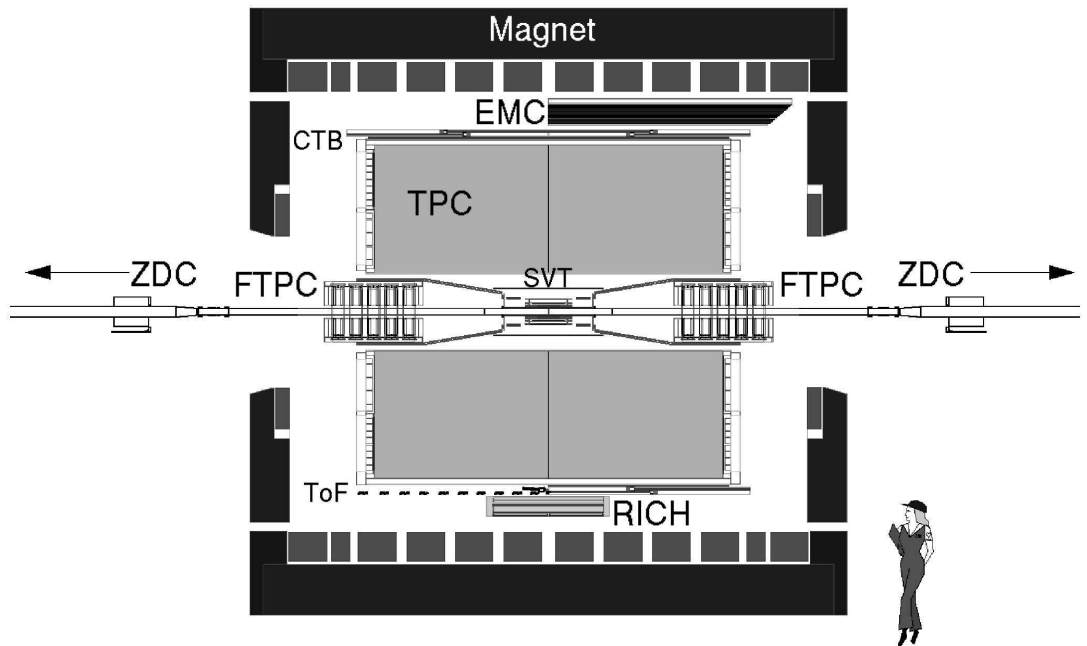
Figure 3.4: Cutaway of the STAR detector in its year 2001 configuration; including a partial installation of the electromagnetic calorimeter (EMC), the temporary ring-imaging Cherenkov detector (RICH), and a time-of-flight detector (ToF) prototype. Figure taken from [35].

3.2.1 TPC

The STAR detector uses the TPC as its primary tracking device [36]. The TPC records the tracks of particles, measures their momenta, and identifies the particles by measuring their ionization energy loss (dE/dx). Its acceptance covers the pseudo-rapidity region $-1.8 < \eta < 1.8$, the full azimuthal angle and the full range of multiplicities up to $\sim 4 \times 10^3$ particles per event. Particles are identified over a momentum range from about 100 MeV to 1 GeV. The TPC can measure particle p_T within the approximate range $0.07 < p_T < 30$ GeV. The momentum resolution depends on η and p_T of the track but for most tracks $\delta p/p \approx 0.02$.

The STAR TPC is shown schematically in Figure 3.5. It measures 4.2 m in length and 4 m in diameter. It sits in a large solenoidal magnet that operates at fields up to 0.5 T. It is an empty volume filled with P10 gas (10% methane, 90% argon) in a well defined, uniform electric field of ≈ 135 V/cm. As a charged particle goes through the gas volume, it ionizes gas atoms and molecules on average every few tenths of a millimeter along its path and leaves behind a cloud of electrons. The electron clusters then drift at a constant average velocity to the readout electronics located at the end caps of the TPC, where their drift time and position are recorded. This information is sufficient for reconstructing the original track position with better than a millimeter precision. The uniform electric field required to drift the electrons is defined by a thin conductive Central Membrane at the center of the TPC which is held at -28 kV, and concentric inner and outer field-cage cylinders.

The readout system is based on Multi-Wire Proportional Chambers (MWPC's) with readout pads. The MWPC's consist of three planes of wires and a pad plane (Figures 3.6, 3.7) connected to the front end electronics.

The three planes of wires are the gating grid, the ground grid and the anode grid. The anode wires are held at a high voltage and provide the necessary electric field to avalanche the electrons from the track ionization. The avalanche leaves a cloud of
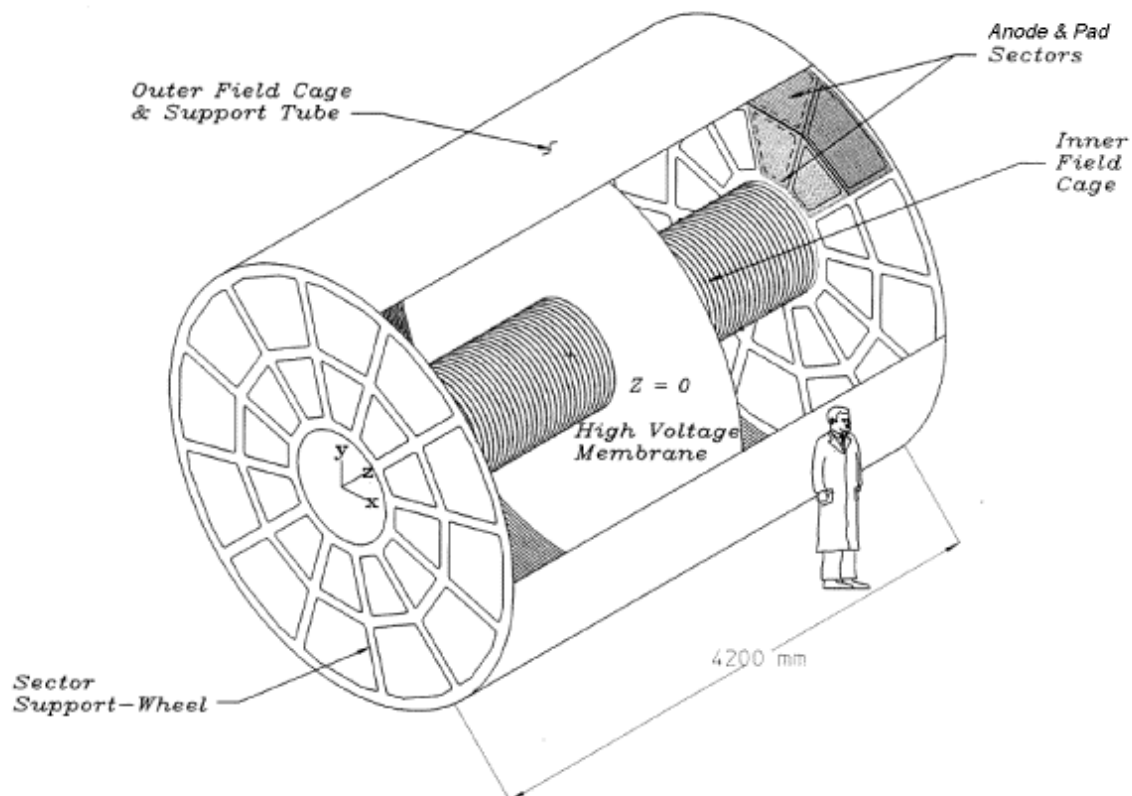
Figure 3.5: Sectioned view of STAR TPC. The STAR TPC surrounds a beam-beam interaction region at RHIC. The collisions take place near the center of the TPC.
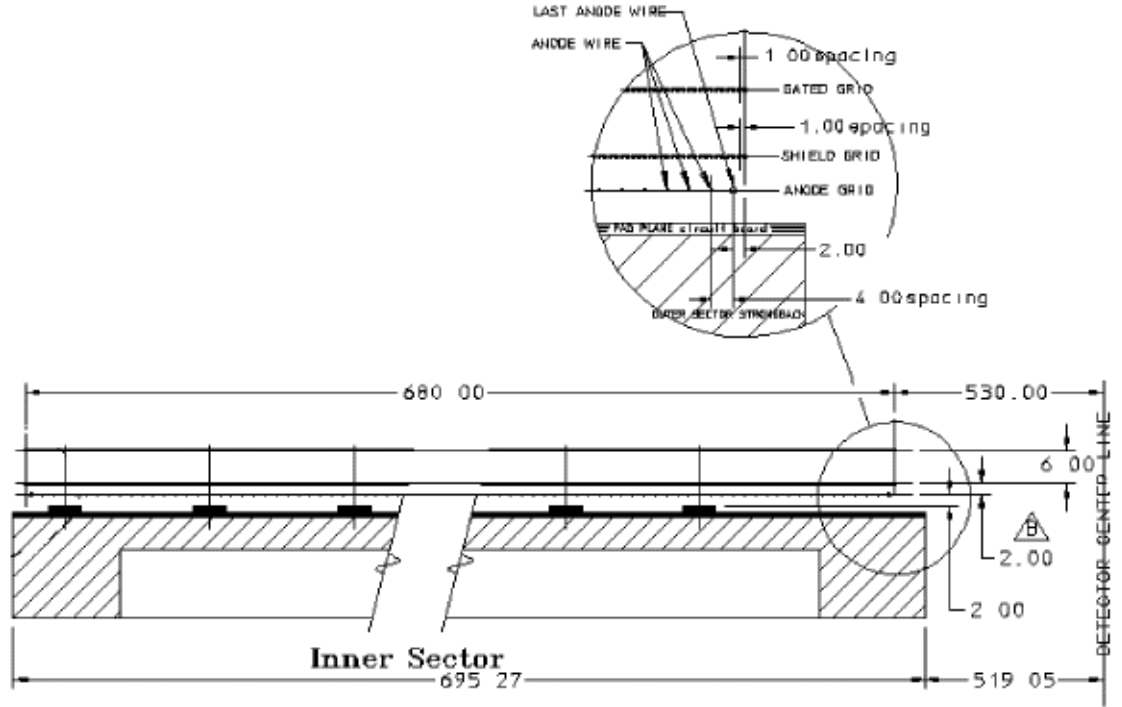
Figure 3.6: Inner sector wire geometry.

positively charged ions, and the readout pads image its charge.

The readout pads are organized into 12 super sectors on each side of the TPC (Figure 3.5). Each super sector is divided into an inner and outer sector (Figure 3.8). There are 13 pad rows in each inner sector and 32 pad rows in each outer sector.

The outer radius sectors have no space between the pad rows to optimize the dE/dx resolution. This is optimal because the full track ionization signal is collected and more ionization electrons improve statistics on the dE/dx measurement.

The inner sectors are in the region of highest track density and thus are optimized for good two-hit resolution. The inner sectors have smaller pads. The anode wires are located closer to the pad plane in order to match the induced signal width to 3 pads.

The primary purpose of the ground grid is to terminate the field in the avalanche region. The grid can also be pulsed to calibrate the pad electronics.
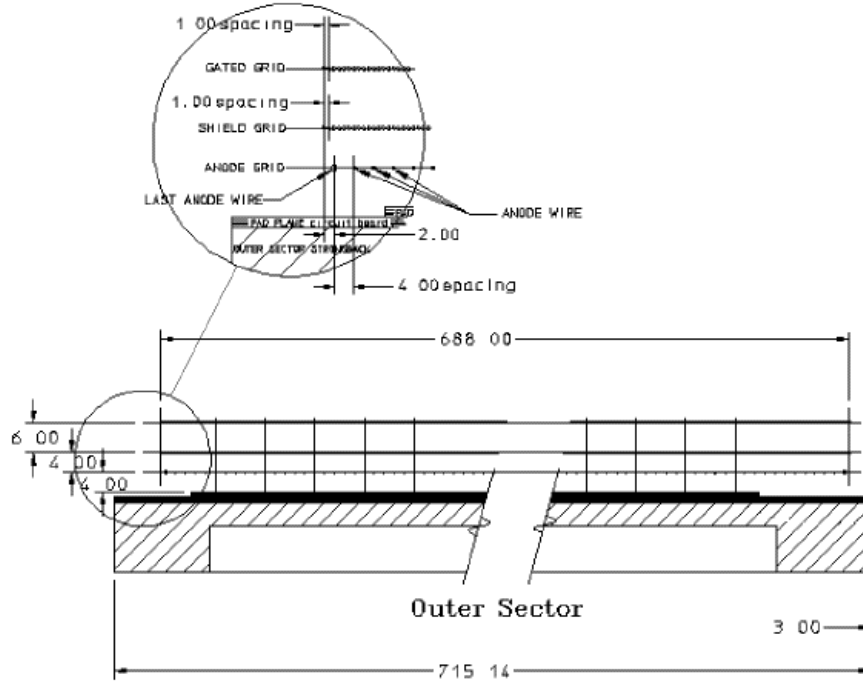
Figure 3.7: Outer sector wire geometry.

The amplification region is separated from the drift region by the gating grid. This grid controls the entry of electrons from the TPC drift volume into the MWPC. The gating grid is 'open' and allows the drift electrons to pass through while the event is being recorded. It is 'closed' the rest of the time. The grid is 'open' when all of the wires are biased to the same potential (~ 110 V). The grid is 'closed' when the voltages alternate ± 75 V from the nominal value. The positive ions move too slowly to escape the MWPC region during the open period and get captured during the closed period.

3.2.2   STAR Barrel EMC

The STAR Barrel EMC consists of sampling towers, shower maximum detector, and a preshower detector. The description of these components is given in the following sections.
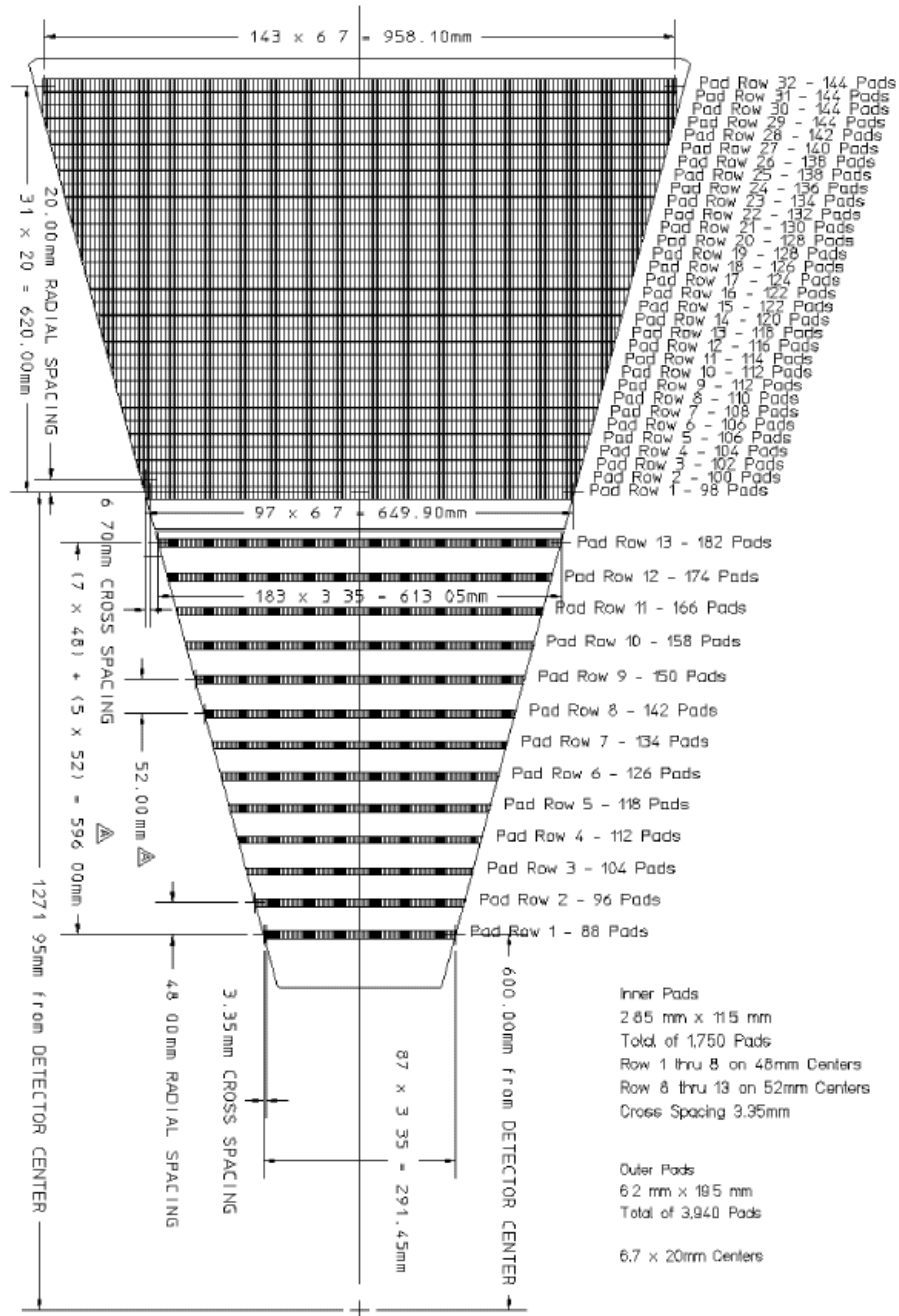
Figure 3.8: The anode pad plane with one full sector shown. The inner sub-sector has small pads arranged in widely spaced rows. The outer sub-sector is densely packed with larger pads.
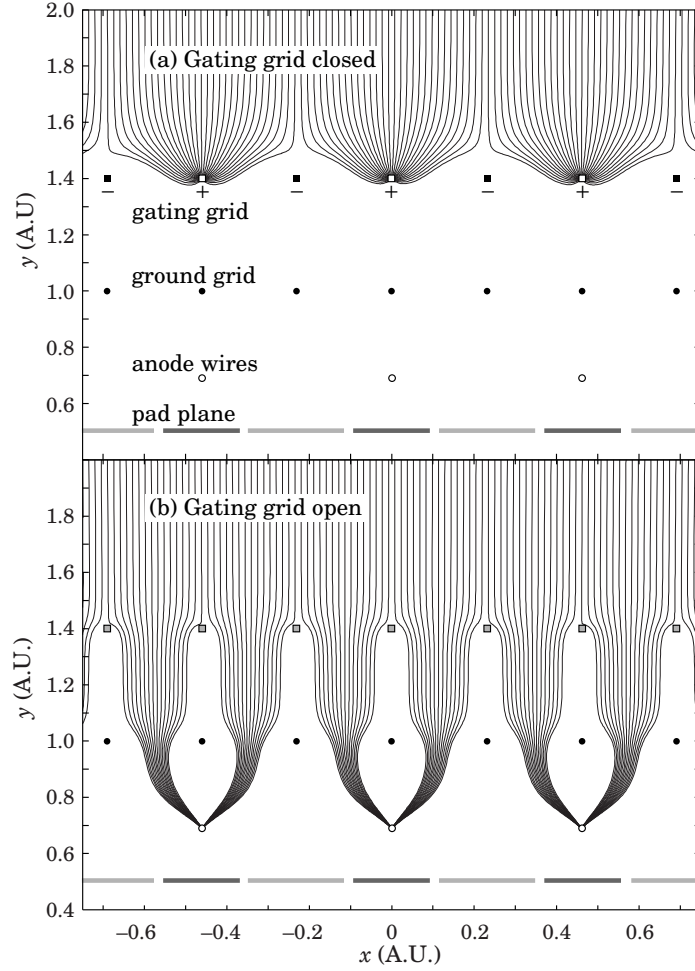
Figure 3.9: Drift field lines in a typical multi-wire proportional chamber (MWPC). The three wire planes, the gating grid, the ground grid, and the anode grids are shown as well as the pad plane. (a) Drifting electrons are collected on the gating grid until gated open by a triggering event. A shielding grid at ground potential is used to terminate the drift region. Electrons drift through an open gating grid (b) pass through to the amplification region around the anode wires. The motion of positive ions generated in the avalanche induces a signal on the segmented pad plane to provide precise measurements of ionization along the wire. The slow positive ions are blocked from entering the drift region by closing the gating grid after the electrons have drifted through. Figure was taken from the Particle Data Book [2].
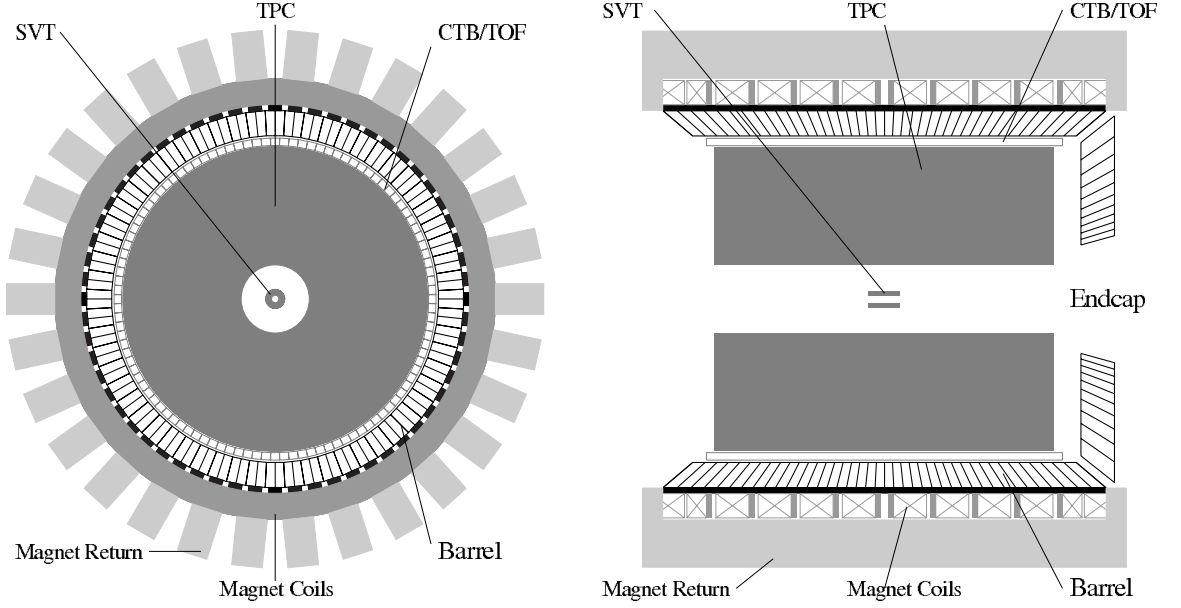
Figure 3.10: Cross sectional view of the STAR detector. The barrel EMC covers $|\eta| < 2$ and 2π in azimuth.

Mechanical Structure

The STAR Barrel EMC (BEMC) is a sampling calorimeter and consists of layers of lead and scintillator (a complete description can be found in [37]). It covers more than 100 m^2 of area outside the TPC for $|\eta| < 1$. The Barrel calorimeter includes a total of 120 calorimeter modules, each subtending 6^0 in ϕ (0.1 radian) and 1.0 unit in η. The modules are mounted 60 in ϕ by 2 in η (Figure 3.10). Each module is about 26 cm wide by 293 cm long with an active depth of 23.5 cm or 21 radiation lengths (X_0) and about 6.6 cm in structural plates (of which 1.9 cm lies in front of the detector). A module is further divided into 40 towers, 2 in ϕ and 20 in η, with each tower being 0.05 in $\Delta\phi$ by 0.05 in $\Delta\eta$. The calorimeter thus is physically segmented into a total of 4800 towers, each of which is projective and pointing back to the interaction diamond. Figure 3.11 shows a side view of a module illustrating the projective nature of the towers in η-direction.

Each module consists of a lead-scintillator stack and shower maximum detectors located about 5 radiation lengths from the front of the stack (Figure 3.11). There
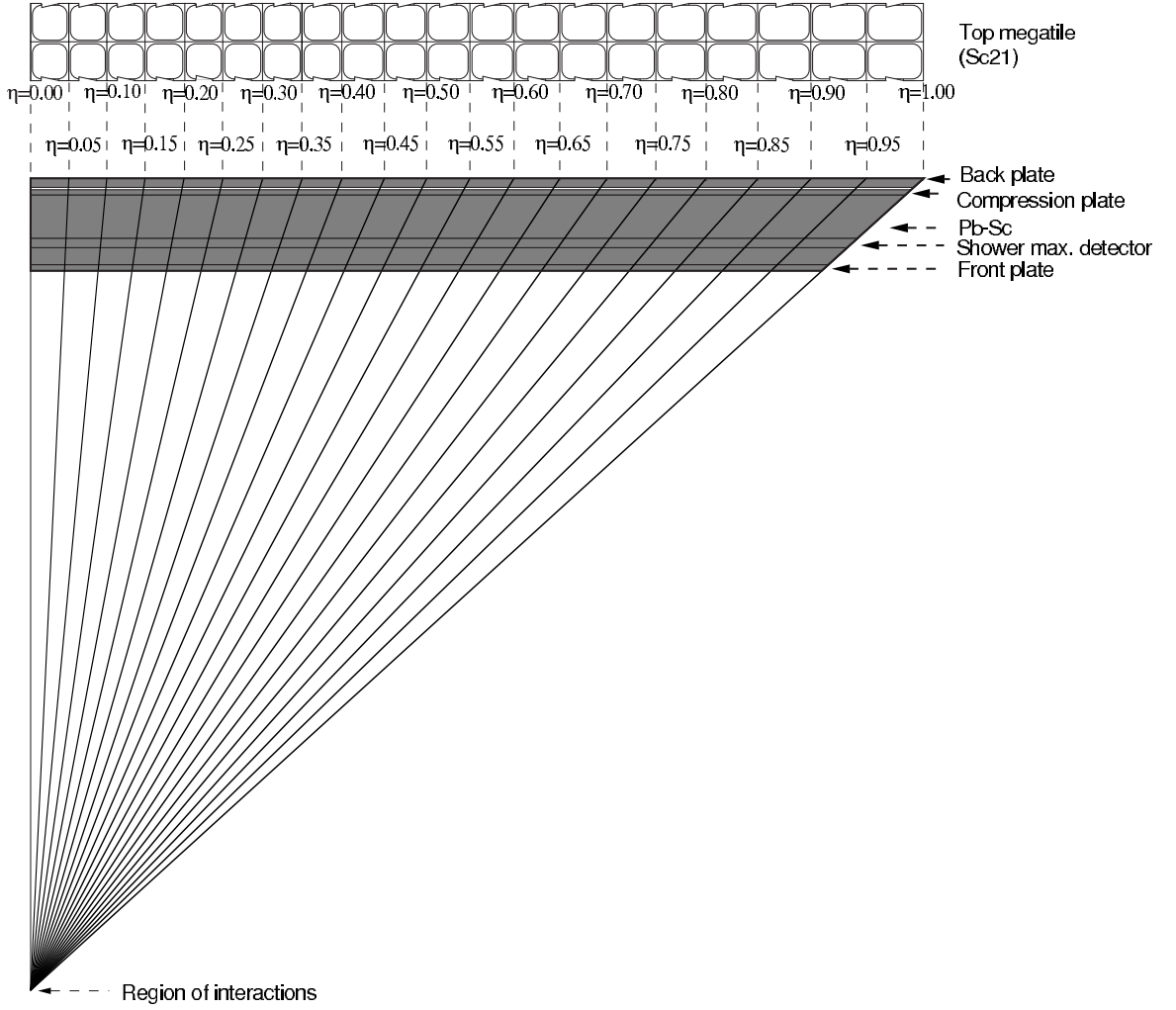
Figure 3.11: Side view of a calorimeter module showing the projective nature of the towers. The 21st megatile layer is also shown.

are 20 layers of lead and 21 layers of scintillator. Lead layers are 5 mm thick; 2 layers of scintillator located in front of the stack and used in the preshower detector are 6 mm thick, and the remaining 19 scintillator layers are 5 mm thick. The stack is held together by 30 straps connecting the non-magnetic front and back plates of a calorimeter module. Figure 3.12 shows an end view of a module along with the mounting system and the compression components.

259.92mm

193.04mm

r=2629.99mm

linear bearing track

69.85mm

33.44mm

91.99mm

linear bearing carriage

back plate-carriage interface plate

24.99mm

back plate

compression plate key

compression plate

Belleville washers

Sc 21
Pb 20
Sc 20
Pb 19
Sc 19
Pb 18
Sc 18
Pb 17
Sc 17
Pb 16
Sc 16
Pb 15
Sc 15
Pb 14
Sc 14
Pb 13
Sc 13
Pb 12
Sc 12
Pb 11
Sc 11
Pb 10
Sc 10
Pb 9
Sc 9
Pb 8
Sc 8
Pb 7
Sc 7
Pb 6
Sc 6

strap

Lead plate

Scintillator tile

302.99mm

SMD

Pb 5
Sc 5
Pb 4
Sc 4
Pb 3
Sc 3
Pb 2
Sc 2
Pb 1
Sc 1

front plate

r=2235

228.16mm

Figure 3.12: End view of a calorimeter module showing the mechanical assembly including the compression components and the rail mounting system. Shown is the location of the two layers of shower maximum detector at a depth of approximately $5X_0$ from the front face at $\eta = 0$.

Optical Structure

There are 21 active scintillating layers in the barrel calorimeter. The scintillator layers alternate with 20 layers of lead absorber plates. The plastic scintillator layers are manufactured in the form of "mega-tile" sheets with 40 optically isolated area segments ("tiles") in each layer. The layout of the 21st mega-tile sheet is illustrated in figure 3.11. The signal from each scintillating tile is read-out with a wavelength shifting (WLS) fiber embedded in a "σ-groove" that is machined in the tile (Figure 3.13). The optical isolation between individual tiles in a given layer is achieved by carving 95% of the depth through the scintillator sheet and filling the resulting groove with opaque, silicon dioxide loaded epoxy. The potential optical cross talk between adjacent tiles as a result of the remaining 5% of the scintillator thickness is cancelled to the level of $< 0.5\%$ by a thin black line painted at the location of the isolation grooves on the uncut scintillator surface.

A total of 840 different tile shapes (420 plus their mirror image) were machined in the layers of each module. The machined, unpolished mega-tile edges are painted white with Bicon BC620 reflective paint. White bond paper, which has good diffuse reflectivity and, most important, a high coefficient of friction, is used on both surfaces of the mega-tile as a diffuse reflector between calorimeter layers.

After exiting the scintillator the WLS fiber is routed along the outer surface of the lead scintillator stack, under the module's light tight cover and terminate in a multi-fiber optical connector at a back-plate of the module. A 2.1 m long multi-fiber optical cable of clear fibers connected with mating optical connectors, carries the light from the optical connector through the magnet structure to decoder boxes mounted on the outer surface of the STAR magnet, where the light from 21 tiles composing a single tower is merged onto a single photo multiplier tube (PMT).

The photo multiplier tubes used for the EMC towers are Electron Tube Inc. model 9125B. PMT's are powered by Cockroft-Walton bases that are remotely controlled
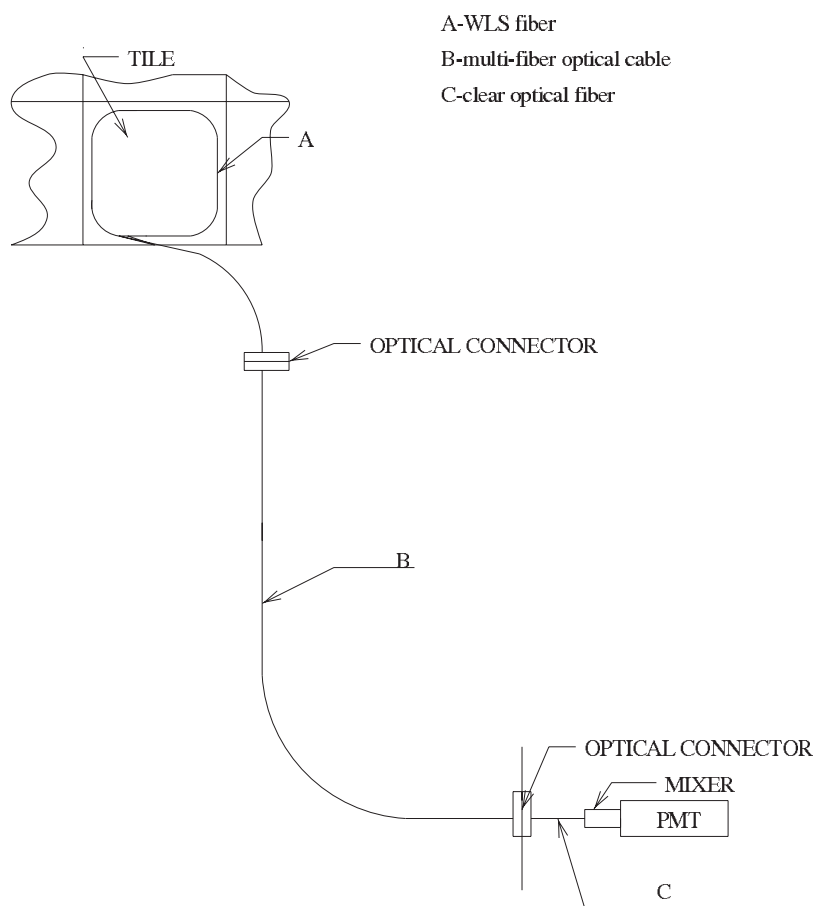
Figure 3.13: A diagram of tile/fiber optical read-out scheme of Barrel EMC.

by the slow control software written in LabView.

3.2.3   STAR Barrel SMD

A shower maximum detector (SMD) is used to provide fine spatial resolution in a calorimeter which has segmentation (towers) significantly larger than an electromagnetic shower size. While the barrel EMC towers provide presice energy measurements for isolated electromagnetic showers, the high spatial resolution provided by the SMD is essential for π^0 reconstruction, direct γ identification, and electron identification. Information on shower position, shape, and, from the signal amplitude, the electromagnetic shower longitudinal development are provided.

Figure 3.14 shows the conceptual design of the STAR BEMC SMD. It is located about 5 radiation lengths deep in the calorimeter modules at $\eta = 0$ including all material immediately in front of the calorimeter[1]. A two sided aluminum extrusion provides ground channels for two independent planes of proportional wires. Independent printed circuit (PC) board cathode planes with strips etched in the η and ϕ directions respectively allow reconstruction of a two dimensional image of the shower as shown schematically in Figure 3.14.

The SMD is a wire proportional counter – strip readout detector using gas amplification. The basic structure of the detector is an aluminum extrusion with 5.9 mm wide channels running in the η direction. A cross sectional view of the detector is shown in Figure 3.15 and the design parameters are summarized in table 3.3.

In the center of the extrusion channels are 50 μm gold plated tungsten wires. The detector strips sense the induced charge from the charge amplification near the wire. Strips perpendicular to the wires provide an image of the shower spatial distribution in the η direction. The other set of strips is parallel to the wires; these provide shower coordinate measurements in the ϕ direction. Signals from the cathodes propagate

---

[1]The depth of the shower maximum detector varies from $4.6X_0$ to $7.1X_0$ counting only the calorimeter material as η varies from 0 to 1.
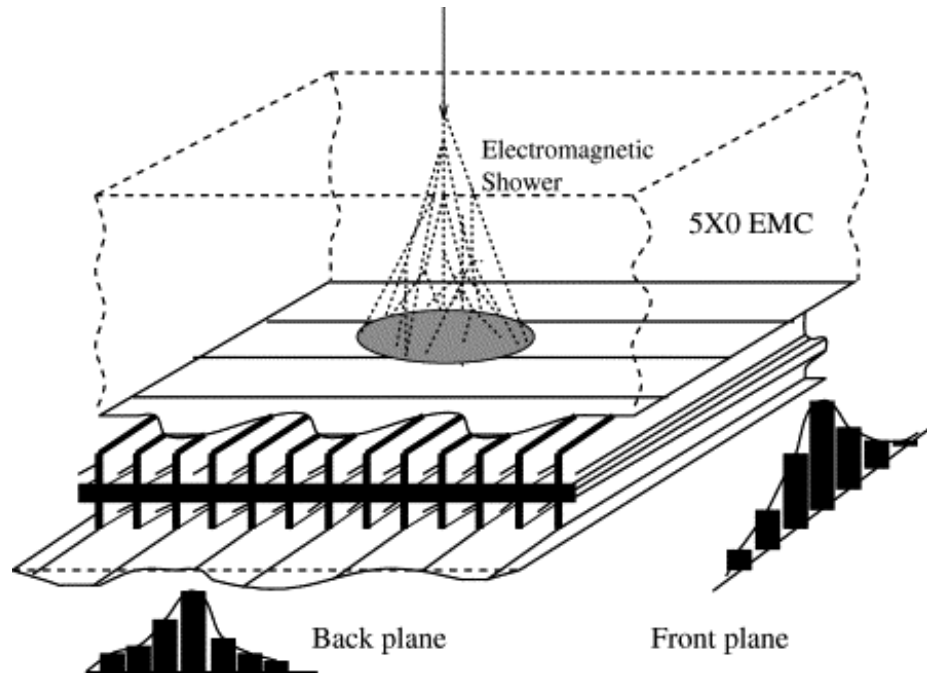
Figure 3.14: Schematic illustration of the double layer STAR BEMC SMD. Two independent wire layers separated by an aluminum extrusion image electromagnetic showers in the η and ϕ directions on corresponding pad layers.
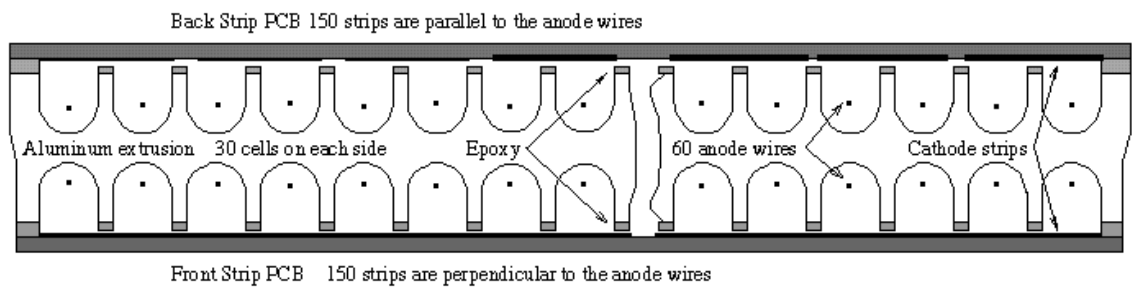
Figure 3.15: Cross sectional view of the SMD showing the extruded aluminum profile, the wires and cathode strips.

SMD Design Parameters	
Chamber Position Inside EMC	$\sim 5X_0$ at $\eta = 0$
Rapidity Coverage (Single Module)	$\Delta\eta = 1.0$
Azimuthal Coverage (Single Module)	$\Delta\phi = 0.105$ (6^0)
Occupancy (pp)	$\approx 1\%$
Occupancy (Au+Au)	> 5 to $\sim 25\%$
Chamber Depth (Cathode to Cathode)	20.6 mm
Anode Wire Diameter	50 μm
Gas Mixture	90%-Ar / 10%-CO_2
Gas Amplification	~ 3000
Signal Length	110 ns
Strip Width (Pitch) in η for $|\eta| < 0.5$	1.46 (1.54) cm
Strip Width (Pitch) in η for $|\eta| > 0.5$	1.88 (1.96) cm
Strip Width (Pitch) in ϕ	1.33 (1.49) cm
Number of Strips per Module	300
Total Number of Modules	120
Total Number of Readout Channels	36000

Table 3.3: STAR Barrel EMC SMD Design Parameters.

along a transmission line plane in the printed circuit boards to reach the front end electronics (FEE) board. At the FEE board, amplified cathode strip signals are buffered in a switched capacitor array before being multiplexed 80 : 1 to external digitizer crates mounted outside the STAR magnet.

3.2.4 Preshower Detector

The first two scintillating layers of the calorimeter have separate readout fibers. The scintillation light from these two layers of each tower is brought to the multi-anode phototubes located in the PMT decoder boxes. A total of 300, 16 pixel multi-anode PMT's are used to read 4800 fiber pairs providing the tower preshower signals. Preshower readout electronics were not installed until RHIC physics run IV.

3.2.5 Barrel EMC Electronics

The BEMC electronics includes trigger, readout of phototubes and SMD, high voltage system for the phototubes, low voltage power, calibration controls, and inter-

faces to the STAR trigger, DAQ and slow controls. Front end electronics including signal processing, digitization, buffering, formation of trigger primitives, and the first level of readout is located in custom EMC crates located on the outside of the magnet iron. SMD front end electronics including preamplifiers and switched capacitor arrays reside on the EMC modules inside the STAR magnet. Schematic view of the BEMC electronics installed on the magnet steel is shown in Figure 3.16.

3.3   STAR Trigger Detectors

In the STAR trigger hierarchy, level-0 (L0) consists of that detector information available, without dead time, at each RHIC crossing. L0 is different from all higher levels in that it selects events for processing while all other trigger levels only function as event aborts.

In STAR, L0 is the only trigger level which does not incur large dead times associated with the opening of the gated grid in the TPC. For all practical purposes L0 is deadtimeless and capable of selecting events on each RHIC beam crossing. The TPC grid cycling rate is limited which makes it very important to concentrate as much functionality as possible in the L0 trigger.

3.3.1   Zero Degree Calorimeters (ZDC)

High energy collisions of nuclei and deuteron-nuclear collisions lead to the emission of evaporation neutrons from the nuclei. At the RHIC beam energy of 100 GeV per nucleon, evaporation neutrons diverge by less than 2 milliradians from the beam axis [39]. Neutrons can be detected downstream of the RHIC collision regions, past the accelerator dipole magnets (Figure 3.17). At this distance from the interaction region (about 18 m), charged fragments follow the beam trajectory closely. In the 'zero degree' region produced particles and other secondaries deposit negligible energy when compared with that of beam fragmentation neutrons.
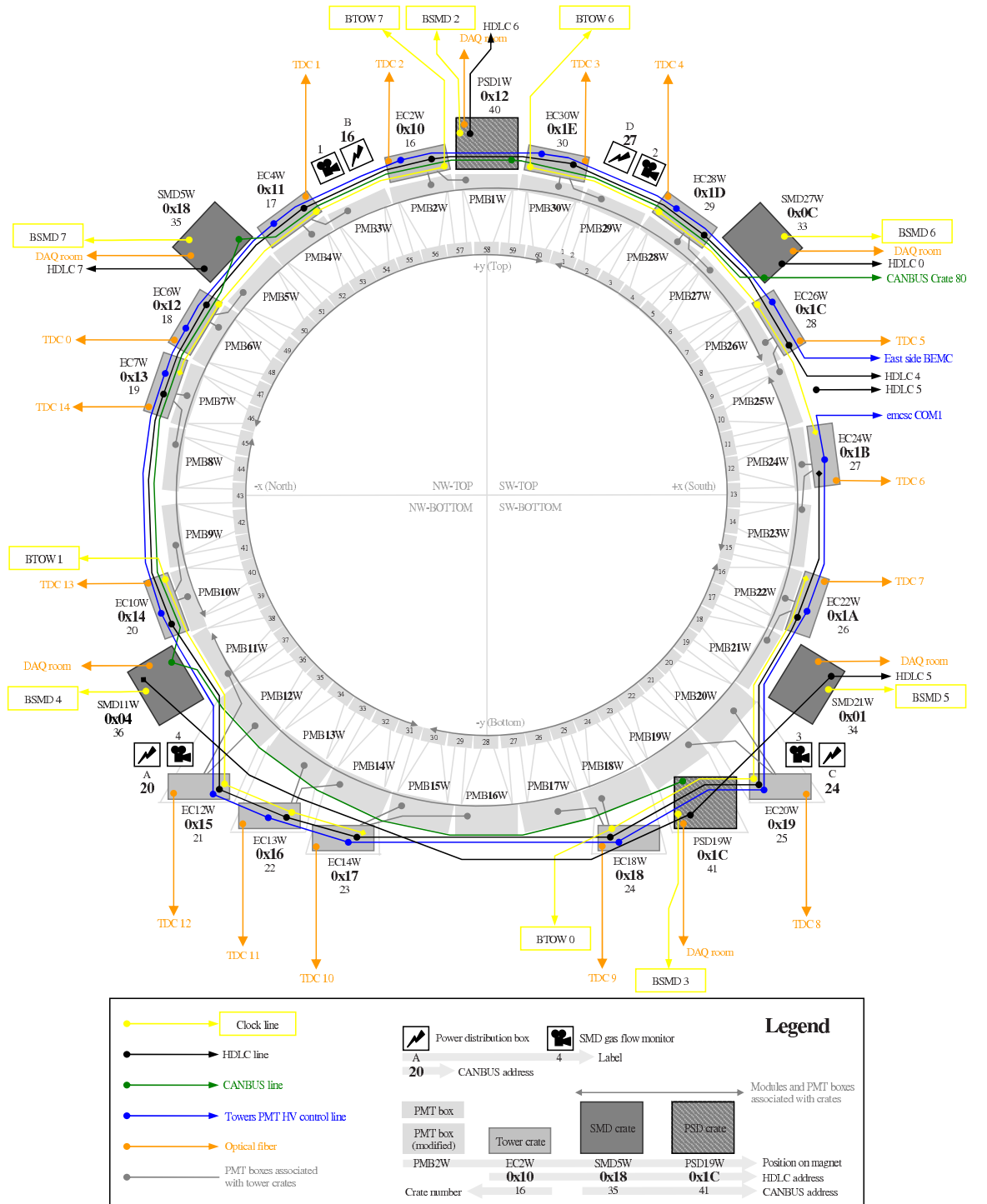
Figure 3.16: Schematic view of the BEMC electronics as seen from the West (positive z direction). During d+Au 2003 and p+p 2004 runs West half of the barrel was fully instrumented. Figure taken from [38].
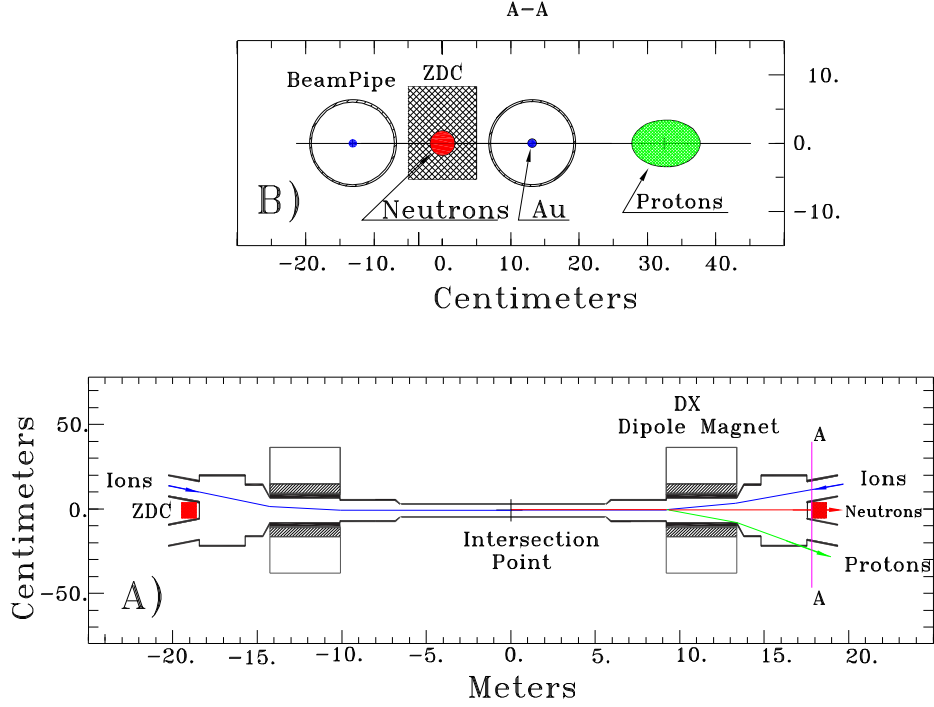
Figure 3.17: Plan view of the collision region and "beam's eye" view (section A-A) of the ZDC location indicating deflection of protons and charged fragments downstream of the dipole magnet.

The purpose of the STAR zero degree calorimeters is to detect neutrons emitted within the cone $|\theta| < 2$ milliradians along both beam directions and measure their total energy. The energy measured by the ZDC's is proportional to the neutron multiplicity, which is known to be correlated with the event geometry and can be used to measure collision centrality.

The minimum bias trigger for d+Au collisions was defined by requiring that at least one beam-rapidity neutron impinge the Zero Degree Calorimeter in the Au beam direction. The measured minimum bias cross section amounts to $95 \pm 3\%$ of the total d+Au geometric cross section. The distribution of the reconstructed primary vertex position along the z-axis for ZDC-triggered minimum bias d+Au events is shown in Figure 3.18.
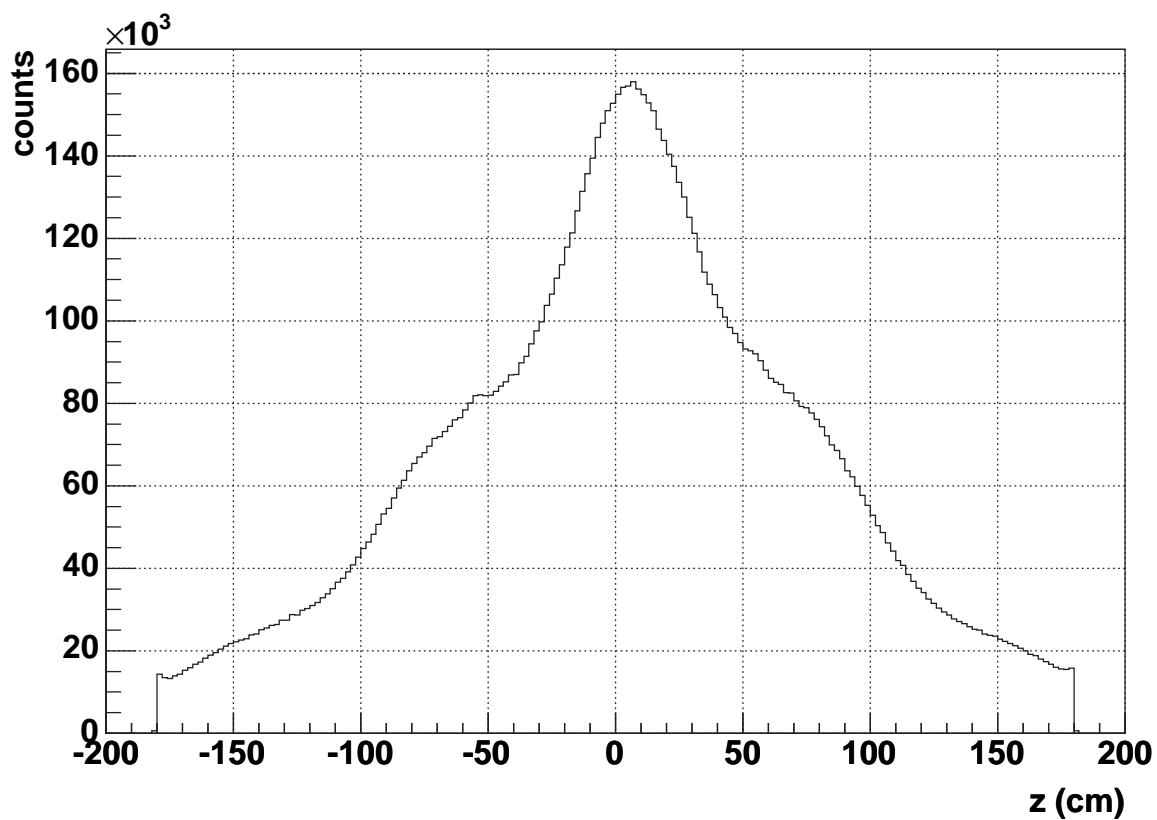
Figure 3.18: Primary vertex position along the z-axis, reconstructed in the TPC, for ZDC-triggered minimum bias d+Au events.

3.3.2 Beam-Beam Counters (BBC's)

The STAR Beam-Beam Counters consist of large and small hexagonal scintillator tiles as shown in Figure 3.19 [40]. They are mounted around the beam pipe on the East and West sides outside the pole-tip of the STAR magnet at ± 3.7 m from the interaction point. The 2×18 arrays of small hexagonal tiles cover a full ring of 9.6 cm inner and 48 cm outer diameter, corresponding to the pseudorapidity region of $3.4 < |\eta| < 5.0$. The small hexagon in the center of the BBC (marked "B" in Figure 3.19) is reserved for the beam pipe. The 2×18 arrays of large hexagonal tiles span a ring of 38 cm to 193 cm in diameter, corresponding to the pseudorapidity region of $2.1 < |\eta| < 3.6$. Each of the scintillator tiles has four wavelength shifting (WLS) optical fibers inserted into circular grooves inscribed within the hexagonal scintillator to collect scintillation light. The WLS fibers are grouped into optical connectors to mate the WLS fibers to clear optical fibers for light transport to the PMT's. PMT output voltages are digitized by Analog to Digital Converters (ADC's).

The BBC's mainly provide a minimum bias trigger for p+p collisions. In terms of the trigger, the main difference between p+p and Au+Au collisions is the multiplicity. A typical central Au+Au event produces about 4000 charged particles, and a minimum bias trigger can be implemented based on the many mid-rapidity tracks and spectator neutrons. Both of these signatures are absent in the p+p collisions.

Charged particles traversing the BBC's produce light in their scintillator tiles. Both BBC's were required to fire to trigger on minimum bias p+p collisions. Due to the dual-arm configuration of the BBC's, the trigger is sensitive to the non-singly diffractive (NSD) cross-section which is the sum of the non-diffractive and doubly diffractive cross-section[2]. The inelastic cross-section is the sum of the NSD and singly

---

[2]The constituent partons of incoming protons may be so little influenced by the interaction that they recombine into the same proton with slightly reduced momentum. Or the incoming hadron may be excited to a more massive state with the same quantum numbers which subsequently decays, such as $p \rightarrow N^* \rightarrow p\pi$. This is called *diffraction scattering*, and the π is a fragment of the incoming p [1].
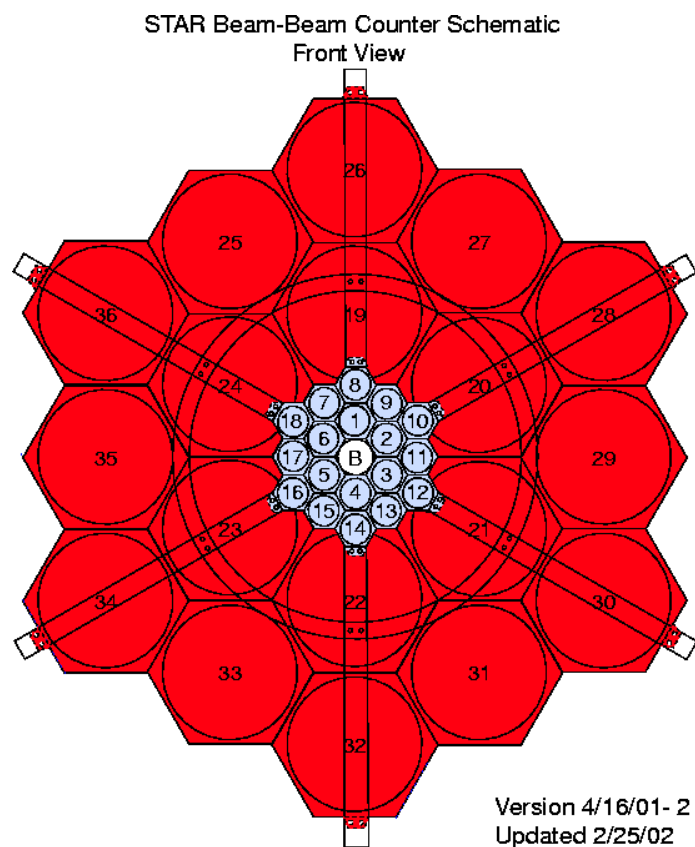
Figure 3.19: Schematic front-view of the Beam-Beam Counters.
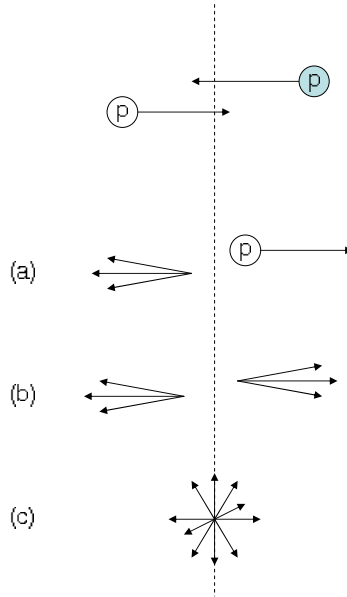
Figure 3.20: Illustration of p+p cross-sections. Non-singly diffractive (NSD) cross-section is the sum of the non-diffractive (c) and doubly diffractive (b) cross-section. The inelastic cross-section is the sum of the NSD and singly diffractive cross-section (a).

diffractive cross-section as illustrated in Figure 3.20.

Apart of providing a minimum bias trigger for p+p collisions, BBC coincidences were used to reject beam-gas events, to measure the absolute beam luminosity $\mathcal{L}$ with 15% precision, and to measure the relative luminosities R for different proton spin orientations with high precision.

3.3.3 Barrel EMC High Tower Triggers

BEMC is an important part of the STAR L0 trigger, capable of triggering on high p_T physics through its electromagnetic component. The STAR jet trigger relies largely on leading π^0's in the BEMC with some contribution from the significantly smaller energy deposition of hadronic showers.

The STAR L0 trigger must provide a trigger to the TPC within 1 μsec (about 10 RHIC beam crossings) and to the STAR L0 trigger processors within about 700 ns, including cable delays. For reasons of speed and limited bandwidth, the EMC trigger

uses trigger primitives instead of the full EMC data. There are two kinds of trigger primitives formed by the EMC front end electronics. The first set of primitives called "high tower trigger" consists of 300 high tower values of 6 bits from the single largest tower ADC within each 4×4 patch of 16 towers. The second set of primitives called "patch trigger" is 300 tower sums, digitized to 6 bits each, from patches of 4×4 towers. These primitives are processed to make a trigger decision on total E_T, jet triggers, γ triggers, etc. These results are then passed to STAR L0 in 700 ns to participate as a component of the final L0 decision. The trigger-DAQ electronics chain for the BEMC is shown in Figure 3.21.

The BEMC tower data is processed via a separate patch. The PMT signals from the towers are integrated and digitized in the front-end cards on every RHIC crossing. These data are pipelined until L0 trigger time, and if a trigger occurs are transferred to a token-addressable memory on the card to await readout.

The logic inside the BEMC digitizer crates that creates the 6-bit "high tower" and "patch" trigger data to be sent to the Data Storage and Manipulation (DSM) boards is presented in Figure 3.22. The "Mask" logic is controlled by the user-accessible registers and is used to zero out specific input channels. The "Ped Sub" logic subtracts a pedestal value from each ADC value. If the ADC value is less than the pedestal value then the result is set to zero. The pedestal value is set individually for each of the 32 channels via a user-accessible register. The "MUX" logic (part of the High Tower algorithm only) is controlled by two user-accessible registers: one for the first set of 16 channels and the other for the second set of 16 channels. The user selects which group of 6 contiguous bits, out of 10, are passed to the "High Tower" selection logic. The "LUT" (*look-up table*, part of the Sum algorithm only) is also user-accessible. It is used to compress the 12-bit sum down to a 6-bit value by whatever mapping the user may chose to load into the "LUT".

The signals from the pads of the SMD are amplified by the FEE cards before
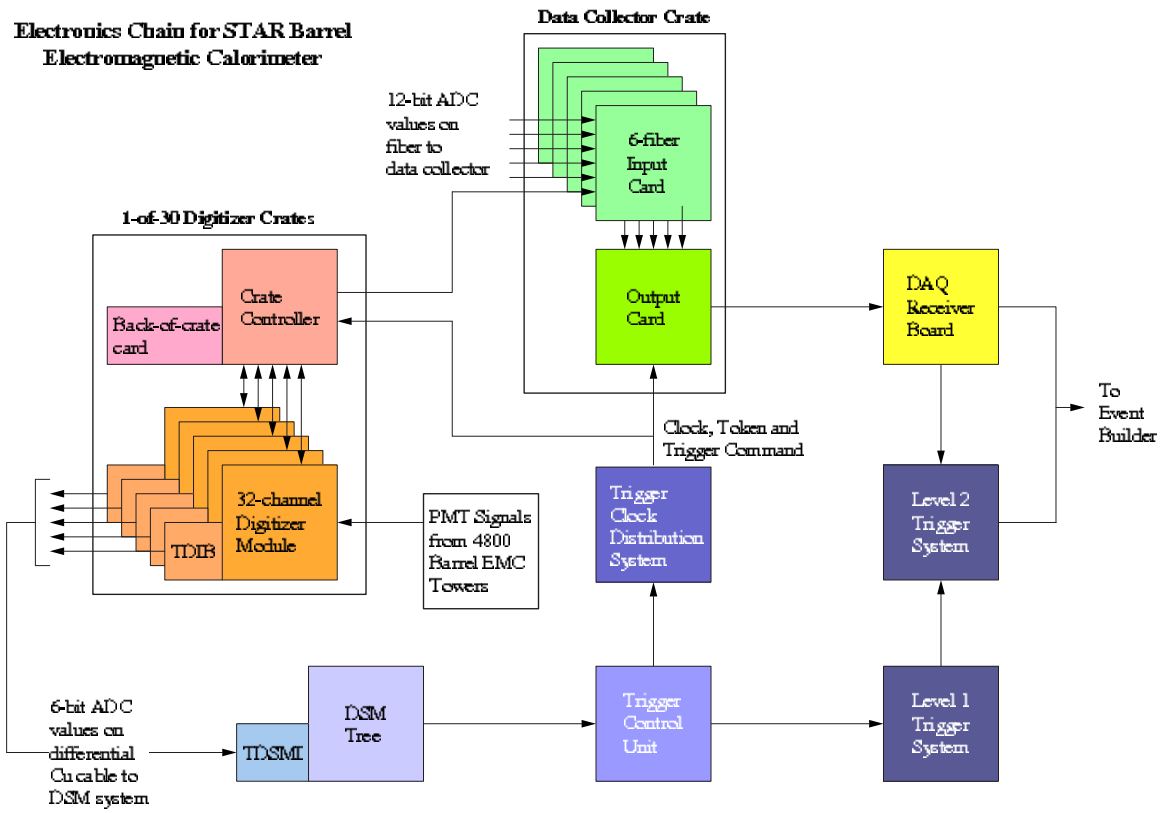
Figure 3.21: Trigger and DAQ electronics chain for the STAR BEMC [41].
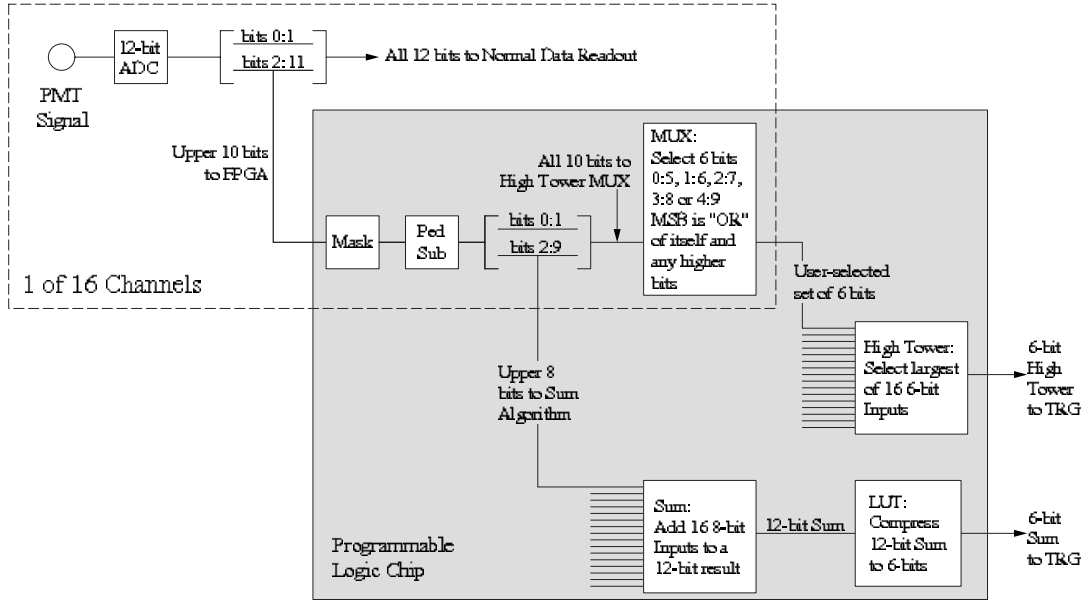
Figure 3.22: Block diagram of trigger logic for the BEMC digitizer board [41]. Note that only half of the logic, *i.e.* 16 channels is shown. Each Digitizer board has 32 channels, and there are 5 digitizer boards in each of the BEMC crates.

entering an analog pipeline composed of switched capacitor arrays to await the L0 trigger. Upon L0 trigger, the SMD analog signals are queued with multiplexing ratio of $80 : 1$ to the 10 bit SMD digitizer crates located outside the STAR magnet. SMD digitized signals are available in STAR L2 trigger processors after $\sim 200~\mu$sec, well ahead of digital information from the TPC.

CHAPTER 4

ANALYSIS AND RESULTS

This chapter is dedicated to a detailed description of the π^0 analysis and presentation of the results. The analysis description includes π^0 reconstruction, yield normalization, and corrections based on simulations. Fully corrected results are used to calculate the p_T dependence of the nuclear modification factor (R_{dA}). Different sources of systematic uncertainties are discussed.

4.1 Neutral Pion Reconstruction

While charged particles are detected using tracking detectors, π^0's are detected using electromagnetic calorimetry via the $\pi^0 \rightarrow \gamma\gamma$ decay channel. A neutral pion decays into a pair of photons with a branching ratio 98.8%, making it the most convenient decay channel for π^0 reconstruction. Positions and energies of the daughter photons are determined using the Barrel EMC, and the production vertex ("primary vertex") is determined by finding the common origin of the TPC tracks. This information completely describes the kinematics of the π^0 decay. The invariant mass of the π^0 is given by:

$$m_{\gamma\gamma} = \sqrt{2E_1 E_2(1 - \cos\theta)}, \tag{4.1}$$

where E_1, E_2 are the energies of the daughter photons, and θ is the opening angle.

When a particle hits the BEMC, it deposits a fraction (possibly all) of its en-

ergy in different parts of the calorimeter: preshower[1], SMD, and sampling towers. Hits, that appear to be produced by the same particle, are grouped into clusters. Clustering is done independently for towers and SMD η- and ϕ-planes. Clusters are then matched together to form BEMC *points*, from which energies and coordinates of photon candidates are determined. In order to improve the coordinate resolution, the BEMC points were required to have clusters in both SMD η- and ϕ-planes. The tracks of charged particles from the TPC were projected on the BEMC, and the track-to-point associations were made. The BEMC points associated with one or more TPC tracks were rejected in order to reduce hadronic contributions to the combinatoric background. All possible pairs of the BEMC points within each event were formed.

Opening angle θ was reconstructed using positions of the BEMC points and the primary vertex position. Only events with reconstructed primary vertex position within 60 cm of the center of the TPC were used for this analysis.

The probability for a decay photon to carry a fraction x of the π^0 energy is the same for all values of x, which is evident from simple kinematic considerations (Appendix A.4). This translates into the uniform energy asymmetry distribution

$$\epsilon_{\gamma\gamma} \equiv \frac{|E_1 - E_2|}{E_1 + E_2} \qquad (4.2)$$

for π^0 daughter γ's. The asymmetry distribution is not flat for random combinations of BEMC points because the energy spectrum of all BEMC points is steeply falling, and the combinations of points with different energies are more likely to occur. An energy asymmetry cut $\epsilon_{\gamma\gamma} < 0.7$ was applied to reduce the contributions from the combinatoric background to the π^0 invariant mass distributions.

For every pair of BEMC points, passing the cuts, $m_{\gamma\gamma}$ and p_T were calculated. The invariant mass distributions were accumulated for different p_T intervals.

In order to increase the sample of events with high-p_T particles, a *high tower*

---

[1]Preshower information was not available for p+p and d+Au runs and is not used in this analisys.

trigger was employed during the data taking. The high tower trigger condition was based on the minimum bias trigger, with the additional requirement of a BEMC tower with the energy above the high tower trigger threshold. For proper normalization, the invariant mass distributions were accumulated independently for minimum bias, HighTower-1, and HighTower-2 triggered events.

4.1.1 High Tower Trigger in d+Au

During the d+Au experimental run, two different high tower thresholds were used, and the corresponding trigger conditions were labeled HighTower-1 and HighTower-2. The minimum bias trigger was suppressed by a *prescale factor* in order to accept less frequent HighTower-1 and HighTower-2 triggers. The HighTower-1 trigger was also prescaled, by a smaller prescale factor. The prescale factors changed from run to run, and were recorded for use in the off-line analysis. The thresholds for HighTower-1 and HighTower-2 triggers were set at 8 (turning on at 9) and 13 (turning on at 14) trigger ADC counts respectively. Tower ADC, which is a 12-bit number used for the regular tower readout, was converted to a 6-bit trigger ADC by dropping the 5 least significant bits (LSB) and replacing the first bit (zeroth bit being the most significant (MSB)) with the result of logical "or" of itself and the MSB. A more detailed description of the BEMC trigger logic is found in section 3.3.3. One trigger ADC count was equivalent to approximately 0.4 GeV in transverse energy during the d+Au run.

4.1.2 High Tower Trigger in p+p

Prior to the experimental run 4, the Data Acquisition System (DAQ) was upgraded to enable higher event acquisition rates. As a consequence of this upgrade, it became possible to record all high-tower-triggered events.[2] This resulted in HighTower-2

---

[2]The prescale factors for HighTower-1 and HighTower-2 triggers were set to 1 during p+p 2004 run.

```
// hiTowerAdc12bit and ped12bit are given as input
int hiTowerAdc10bit = hiTowerAdc12bit / 4;
int operationBit = 1; // subtract: +1 (default)
                      //      add:  0
const int pedestalTargetValue = 8;
int val12bit = ped12bit - pedestalTargetValue;
if(val12bit < 0)
   {
     val12bit  = -val12bit;
     operationBit = 0;
   }
int val10bit = val12bit / 4;
if(val12bit - val10bit * 4 > 2)
  val10bit += 1;
if(val10bit > 15)
  val10bit = val10bit - 4 * ((val10bit - 11) / 4);
if(operationBit == 1)
  hiTowerAdc10bit -= val10bit;
else
  hiTowerAdc10bit += val10bit;
int hiTowerAdc6bit = ((hiTowerAdc10bit  >> 3) & 63) |
                     (((hiTowerAdc10bit >> 3) & 64) >> 1);
// hiTowerAdc6bit value is compared
// against the HighTower trigger threshold
```

Figure 4.1: The algorithm for conversion of 12-bit tower ADC to 6-bit trigger ADC, presented as a sequence of C++ statements. The names of the variables are self-explanatory. The algorithm is identical to that used in the trigger logic during the p+p run.

data set being a sub-set of HighTower-1 triggered data. The threshold for HighTower-1 trigger was set at 10 ADC counts (turning on at 11). In order to remove the effects of the pedestal jitter in the "patch trigger" sum[3], which is defined in section 3.3.3, tower trigger pedestals were set to values near $8(2n+1)$, where n was a non-negative integer. The algorithm for conversion of 12-bit tower ADC to 6-bit trigger ADC, identical to that used in the trigger logic, is shown in Figure 4.1. It is not meant to be intuitive, and is provided for documentation. One trigger ADC count was equivalent to approximately 0.27 GeV in transverse energy during the p+p run.

---

[3] "Patch trigger" was not used in this analysis.

4.2   Neutral Pion Yields

Both neutral pions and combinatoric background from random combinations of BEMC points contribute to the invariant mass distributions accumulated in different p_T bins. These contributions must be separated in order to extract the π^0 yield. This may be accomplished with a *mixed events* technique, or by fitting the $m_{\gamma\gamma}$ distributions with a function, assuming a certain shape of the background and the π^0 peak. Fitting the background is a more straightforward method but has the disadvantage of ambiguity in choosing the fitting function and the subrange to fit. The mixed events method is based on the idea that the BEMC points in two different events are uncorrelated, thus the background may be reproduced by building invariant mass distributions using points taken from different events of similar multiplicity. While reproducing the background accurately at $m > 0.3$ GeV, this method fails to reproduce the lower part of the invariant mass spectrum ($m < 0.1$ GeV), where the background shape is influenced by "split clusters" (Figure 4.2). Cluster splitting occurs when the energy of a single tower cluster is split between two SMD clusters proportionally to their energies. Signal from the split clusters cannot be reproduced by constructing an invariant mass distribution using pairs of BEMC points taken from different events. The mixed events method produces an invariant mass spectrum of *uncorrelated* pairs of points. All features of the $m_{\gamma\gamma}$ distribution due to the correlations are lost, including the low-mass background due to split clusters. Therefore, we selected the method of fitting the $m_{\gamma\gamma}$ spectra to extract signals.

The invariant mass distributions were fitted with the following function:

$$f(p_T) = A \exp\left(-Bp_T\right) + \frac{CW}{E\sqrt{2\pi}} \exp\left(-\frac{(p_T - D)^2}{2E^2}\right) + F + G\left(p_T - H\right)^2 + Ip_T, \ (4.3)$$

where parameters $A \ldots I$ were allowed to vary, and W was set equal to the bin

width of the $m_{\gamma\gamma}$ histogram. Parameters C, D, E describe the Gaussian shape of the π^0 peak, and can be identified with the π^0 yield, mass and peak width, respectively. Other parameters describe the combinatoric background. Invariant mass distributions for minimum bias triggered d+Au events are shown in Figure 4.2.

The method of yield extraction from the fits to the invariant mass spectra works well in p_T bins with sufficient statistics, and begins to fail at higher p_T, where the π^0 peak shape (as well as the background shape) is not well defined due to the limited statistics. The invariant mass spectra were not fitted above a certain p_T chosen individually for each of the trigger conditions (minimum bias, HighTower-1, and HighTower-2). The yield for these high-p_T bins was extracted by integrating the $m_{\gamma\gamma}$ distributions in the signal region, and subtracting the background contribution. The background was estimated by calculating the average values of the $m_{\gamma\gamma}$ distribution in the regions adjacent to the signal region. The background shape was approximated by a linear function.

The neutral pion yield was normalized to the number of minimum bias events passing the event cuts. The normalization factor for the π^0 yield extracted from the minimum bias data is given by

$$F_{MB} = \frac{1}{\sum\limits_{i} N_{MB}^i}, \tag{4.4}$$

where N_{MB}^i is the number of minimum bias events satisfying the event selection criteria in run i, and the summation is carried over all runs. The normalization factors for HighTower-1 and HighTower-2 are given by

$$F_{HT_k} = \frac{1}{\sum\limits_{i} N_{MB}^i} \cdot \frac{\sum\limits_{i} \left(\frac{P_{HT_k}^i}{P_{MB}^i} \cdot N_{HT_k}^i \right)}{\sum\limits_{i} N_{HT_k}^i}, \tag{4.5}$$

where index k takes values 1 or 2 to label HighTower-1 and HighTower-2 triggers, $P_{HT_k}^i$
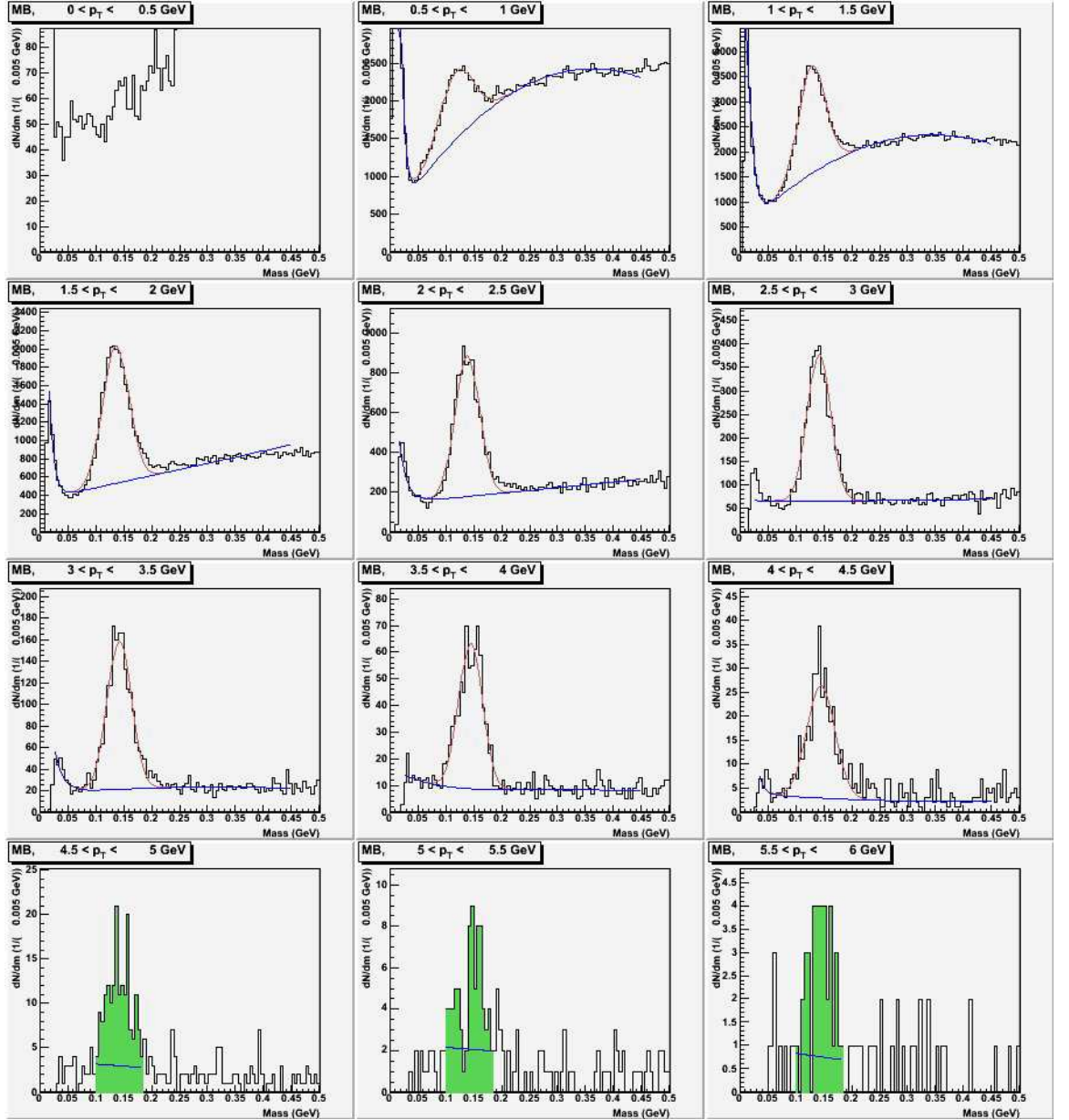
Figure 4.2: Invariant mass distributions for minimum bias triggered d+Au events in different p_T bins. Fit functions are also shown. Due to limited statistics above 4.5 GeV the π^0 yields were extracted by integrating the $m_{\gamma\gamma}$ distributions in the signal region.

is the prescale factor for trigger HT_k in run i, $N^i_{HT_k}$ is the number of HighTower-k triggered events in run i, and the summation index i goes over all runs with HighTower-k triggers.

Figure 4.3 shows the π^0 yield from d+Au collisions for different triggers, plotted as a function of p_T, normalized by the number of minimum bias events using normalization factors (Eq. 4.4) and (Eq. 4.5). Points with $p_T < 1.5$ GeV from the minimum bias data set are affected by the energy thresholds of the cluster finder. Lowest points in p_T from HighTower-1 and HighTower-2 data sets are affected by the high tower trigger thresholds. A number of corrections remain to be applied to these yields to extract invariant cross section. These corrections will be discussed further in this chapter.
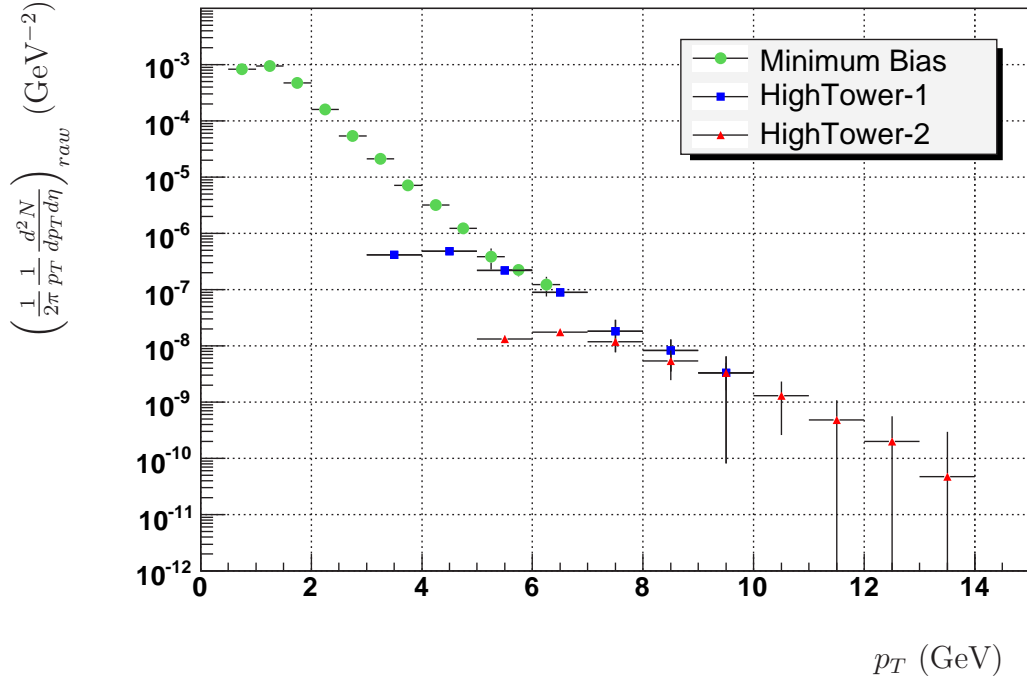
Figure 4.3: Uncorrected π^0 yield, normalized to the number of d+Au minimum bias events passing the event cuts, as a function of p_T. Data points are plotted in the centers of p_T bins.

4.3   Monte Carlo Simulations

The raw π^0 spectrum must be corrected to account for different factors that affect the π^0 reconstruction probability. These factors can be subdivided into two categories: those having to do with the detector acceptance, and those due to the reconstruction efficiency.

The acceptance of the BEMC is not continuous in pseudorapidity η and azimuthal angle ϕ, but is a complicated structure due to cracks between the modules, dead areas, noisy or dead channels, etc. The acceptance does not remain constant through the experimental run. It changes in time due to failures and repairs that occur in the detector hardware and readout electronics during the running period.

The fficiency of π^0 reconstruction is affected by both hardware and software. Hardware factors are related to the probability of a daughter photon to deposit energy in a BEMC tower and SMD layers, as well as being selected by the trigger. Software factors include calibration accuracy, cluster finder and point maker efficiencies, and primary vertex reconstruction efficiency.

Efficiency and acceptance effects are so tightly interrelated that it is practically inconceivable to distinguish the two. It is possible however to estimate the gross factor of efficiency and acceptance effects using Monte Carlo simulations. The method of Monte Carlo simulations is a powerful tool capable of giving the answer to the question of interest, namely, given a π^0 with known coordinates and momentum, what is the probability that it will be detected and recognized as a π^0 in the invariant two-photon mass spectrum constructed from many events?

4.3.1   GEANT Detector Simulation

The passage of particles through the detector material is simulated using the "industry" standard GEANT software package developed and maintained by the CERN Application Software Group. GEANT is a highly developed library that models

electromagnetic and nuclear interactions of particles with matter. Along with the capability to track particles through the experimental setup for simulation of the detector response, GEANT also provides tools for graphical representation of the detector geometry and particle trajectories.

The STAR detector is described by a highly detailed three dimensional model that is built using pre-defined geometrical primitives of specified material. The GEANT model of STAR is organized in a tree-like structure allowing for easy navigation along an arbitrary trajectory. GEANT models the propagation of particles through the detector representation by simulating multiple scattering, energy loss, conversion, and particle decay along each step of the particle trajectory. The output of GEANT is a full simulation of the propagation of a given particle type through the detector volume. More information on GEANT can be found in Ref. [42].

4.3.2   Status Tables

The acceptance of the Barrel Electromagnetic Calorimeter was not constant in time during the data taking. There are several factors that influence the detector acceptance, such as individual electronics channel failures and occasional crate failures, when a significant part of the detector was affected. The changes in the detector acceptance are reflected in the time-stamped status tables containing the status of every channel (EMC towers or SMD strips) of the BEMC [38]. The status tables were constructed using the information from the individual channel spectra, accumulated on a run-by-run[4] basis. A status is assigned to each channel based on the pedestal shape and position, fraction of the signal above the pedestal, and signal shape, summarized in Table 4.1. Figure 4.4 displays a graphical representation of the run-by-run status tables of all 2400 BEMC towers that were operational during the d+Au and p+p running periods of years 2003 and 2004. Similar tables were constructed for the

---

[4]In this context the term "run" refers to one RHIC fill.

SMD [43].

BEMC status assignment criteria	
Description	Criterion
Fitted pedestal peak mean is outside the allowed ADC range	$\mu_{ped} < 10$ or $\mu_{ped} > 80$
Fitted pedestal peak mean is too broad	$\sigma_{ped} > 3$
Insufficient statistics	pedestal height < 10
Fitted position is too far from the position of the maximum	$|\mu_{ped} - ADC_{maximum}| > 2\sigma_{ped}$
Tower ADC is zero for some events	$N_{ADC=0} > 0$
Signal fraction is too low	$signal/total < 0.001$
Signal fraction is too high	$signal/total > 0.1$

Table 4.1: BEMC status assignment criteria for d+Au run 2003. Each tower was assigned a status code. Zero code was assigned to towers that did not match any of the above criteria. For this analysis all towers with non-zero status code were considered bad.

The purpose of constructing the status tables was two-fold: to exclude the bad channels from the analysis, and to account for the imperfections in the detector acceptance in the Monte-Carlo simulations. All channels with non-zero status code were dropped (ADC set to zero) from both real and simulated data.

4.3.3 Embedding

In order to estimate the effects of the background on reconstruction efficiency, π^0's are embedded into a real events. Embedding is done by first simulating the kinematics of a π^0 decay using the primary vertex position taken from the real event. The detector response is then simulated using a realistic detector geometry and electronics characteristics (digitization algorithm, noise etc.).

Changes in the detector acceptance are reflected in the sets of time-stamped status tables constructed using the information obtained from the real data. In the status tables, each channel of the BEMC and SMD detectors is assigned a numeric code representing the channel status during the period of validity of a particular status table. Simulated and real hits were preserved by the reconstruction code only in
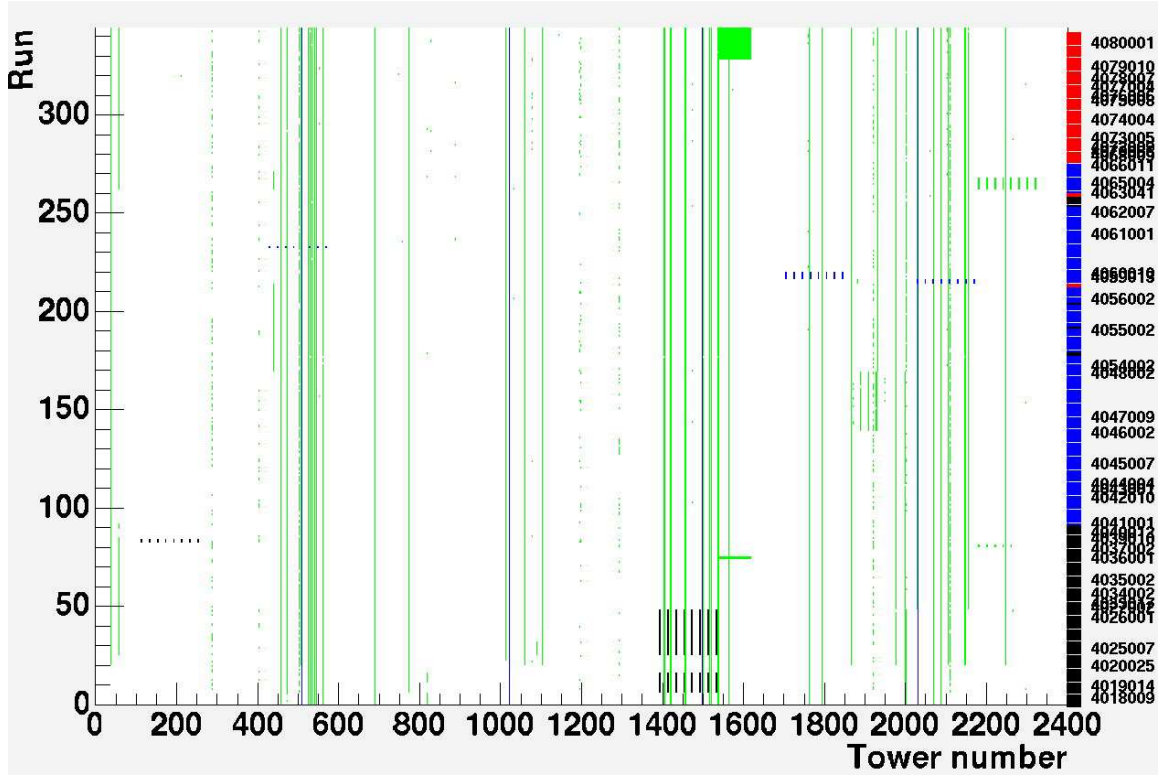
Figure 4.4: Run-by-run status of the BEMC towers during the d+Au 2003 run. Towers with zero status are marked with white color. Average number of good towers throughout the d+Au 2003 run was 2290 (95.4%).

cases where the corresponding channel was marked as good in the appropriate status table. Energies for all other channels were set to zero. This procedure prevented simulated and real hits from being found in the dead, noisy, or otherwise problematic channels of the detector.

Simulated signals from all the detectors are then superimposed on the detector signals obtained from the real event. The event constructed this way is put through the same reconstruction chain used for real data. All information about the embedded π^0 and its decay products is stored separately and is available for further analysis. The essential assumption of this method is that the background event remains undisturbed by the introduced (embedded) signal, meaning the shapes of various distributions characteristic of the event are preserved.

For this analysis, 7.07×10^5 d+Au minimum bias events with a reconstructed vertex position $|z| < 60$ cm were embedded with one π^0 per event with the following kinematic constraints:

- Uniform pseurorapidity window, $-0.3 < \eta < 1.2$ covering the detector acceptance for primary vertex positions $|z| < 60$ cm

- Full azimuthal coverage $-\pi < \phi < \pi$

- Flat p_T distribution from 0 to 15 GeV

In order to account for the "p_T smearing" effect, the flat p_T spectrum of embedded π^0's was scaled according to the steeply falling charged hadron p_T spectrum $\left(\frac{h^+ + h^-}{2} \right)$ measured by STAR [30]. The p_T smearing effect mentioned above can be illustrated with help of the following example. A π^0 of a given p_T can be reconstructed with transverse momentum greater or lesser than its actual p_T. The π^0 spectrum is steeply falling with p_T, thus leading to a substantial "leakage" of lower-p_T π^0's to higher-p_T bins, whereas the leakage to lower-p_T bins is negligible. To simulate this effect, each

π^0 was associated with a weight calculated according to the $\frac{h^+ + h^-}{2}$ p_T spectrum shown in Figure 4.5.

4.3.4 π^0 Simulation

In low-multiplicity collisions, such as p+p, distortions of cluster energies due to the background are negligible. For acceptance and efficiency studies, it is sufficient to simulate a single π^0 per event. The reconstruction procedure is identical to that described in Section 4.3.3, except that the detector signals, resulting from the simulated π^0, are not merged with the signals from real events. Using the following criteria, 2×10^5 events were simulated.

- Gaussian distribution of the vertex position, centered at zero, with $\sigma_z = 60$ cm.

- Uniform pseurorapidity window, $-0.5 < \eta < 1.5$

- Full azimuthal coverage $-\pi < \phi < \pi$

- Flat p_T distribution from 0 to 20 GeV

4.3.5 Photon-To-Point Association

Each of the π^0 daughter photons was matched to the BEMC point (if any) within a cone of radius 0.05 radians in η and ϕ around the "γ track" (information about the π^0 daughter photons is known from the simulations). Angle of 0.05 radians is equal to the angular size of one BEMC tower viewed from the center of the TPC. In case more than one point lies within the specified cone, the photon track was matched to the closest point in η and ϕ, .

4.3.6 Detector Acceptance

For a single-particle analysis, the acceptance of a detector is determined by the number of particles reaching the detector surface relative to the number of particles
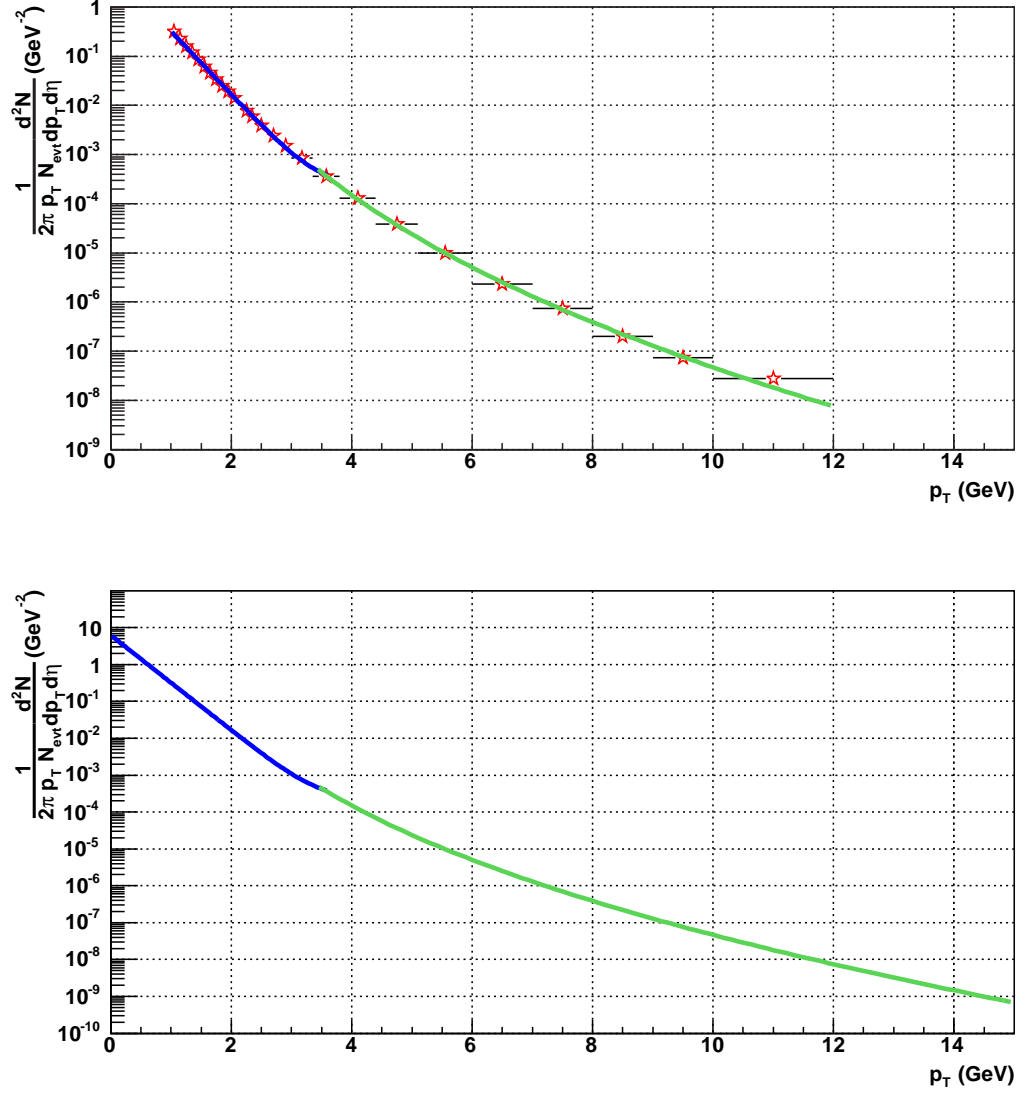
Figure 4.5: Inclusive charged hadron p_T distribution $1/(2\pi p_T)d^2N/dp_T d\eta \mid_{\eta=0}$ for minimum bias d+Au collisions measured by STAR [30]. Solid lines are fits to the data points (top panel). The data points were fitted with 2 functions of arbitrary nature. For the purpose of scaling the π^0 spectrum it is essential that the fit follows the data points closely. Fit functions plotted in the full range of simulated π^0 p_T are shown in the bottom panel.

emitted into the phase-space segment in which the measured quantity (e.g. particle yield) is determined. One-half of the full barrel of the electromagnetic calorimeter, that was used for data-taking during the d+Au and p+p experimental runs, covered one unit of rapidity and full azimuthal angle ($0 < \phi < 2\pi$). Since neutral pions are reconstructed via the two-photon decay, we re-define the acceptance as the ratio of the number of π^0's emitted into the continuous phase-space segment, $\Delta\eta \times \Delta\phi = 1 \times 2\pi$, covering the BEMC surface, to the number of π^0's that produced 2 points in the BEMC. Defined this way, the acceptance becomes dependent on cluster-finder settings, point selection criteria, primary vertex position, etc. It is therefore unpractical for this analysis to calculate the detector acceptance as a stand-alone quantity. Instead, acceptance convoluted with the π^0 reconstruction efficiency is calculated.

A quantity sensitive to the the detector acceptance is the number of π^0 candidates per minimum bias event, calculated on a run-by-run basis (Figure 4.6). A fraction of the d+Au data taken before day 40 were affected by a corrupted SMD pedestal table during the off-line data production, resulting in partial loss of the SMD information. This is reflected in Figure 4.6 ($N_{pairs}/N_{MB} < 0.01$), since both BEMC points were required to have clusters in each of the SMD planes in order for this pair of points to be considered a π^0 candidate. A list of runs with the ratio $N_{pairs}/N_{MB} < 0.1$ was composed, and such runs were excluded from the analysis.

After the data runs with anomalous BEMC acceptance were filtered out, the remaining variations in the detector acceptance were accounted for in the simulations. In order to calculate the time-averaged efficiency and acceptance corrections, the Monte Carlo events were reconstructed with different status tables. The number of Monte Carlo events, reconstructed with each of the status tables, was set proportional to the number of real events taken during the time interval of validity of each particular status table. This was accomplished in several steps:

- The duration of the entire experimental run was divided in 1-hour intervals.
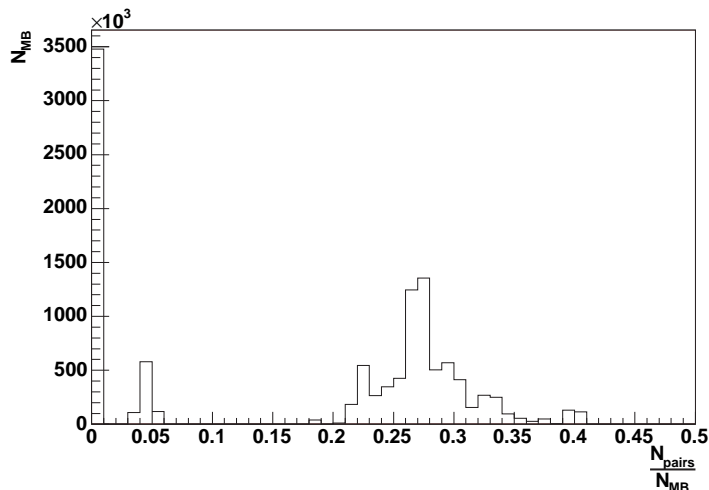
Figure 4.6: Distribution of the number of π^0 candidate pairs per one minimum bias triggered event in d+Au 2003 run, calculated on the run-by-run basis, and weighted by the number of minimum bias events.

- The number of events N_{events}, taken during each of the 1-hour intervals, was calculated.

- For each 1-hour interval, the time stamp, corresponding to the beginning of the hour, was tabulated, along with the number $N_{sim} \equiv N_{events}/n$, where n is a constant factor for the whole data set.

- For every entry in the table, constructed in the previous step, N_{sim} Monte Carlo events were reconstructed with the appropriate time stamp, which ensured that the relevant status tables were picked up from the database.

Since the trigger configurations[5] and the prescale factors for different triggers changed from run to run, the above procedure was performed independently for each trigger used in this analysis, namely minimum bias, HighTower-1, and HighTower-2. The HighTower-2 trigger was not used in p+p data analysis as described in Section 4.1.2.

---

[5]Each trigger configuration was labeled by the *trigger setup name*. Among other things, different trigger configurations defined which trigger conditions were present in the run ("trigger mix").

4.3.7 π^0 Reconstruction Efficiency

The invariant mass was constructed using pairs of BEMC points if both of the points were matched to π^0 daughter γ's. Event cuts and point-selection criteria were the same as the cuts used with the real data, described in Section 4.1. In addition, simulated events were required to satisfy the appropriate trigger condition. All simulated events were assumed to satisfy the minimum bias trigger conditions. HighTower-1 and HighTower-2 triggers for d+Au data were simulated by requiring a high tower in the event with trigger ADC greater than 8 and 13, respectively. HighTower-1 trigger condition for p+p data was simulated by requiring a high tower in the event with trigger ADC greater than 10. Each entry in the invariant mass histogram was weighted according to the spectrum shown in Figure 4.5. It is worth mentioning that the quantity plotted in Figure 4.5 has a factor of $1/p_T$ in it; weights calculated according to this distribution were multiplied by p_T. Invariant mass spectra for different p_T bins[6] were fitted with a Gaussian. The yield of the simulated π^0 for each p_T bin, calculated using the fit parameters, is shown in Figure 4.7. The number of events, passing the z-vertex cut, weighted according to the charged hadron p_T spectrum, with 3-momentum of the simulated π^0 pointing into the detector acceptance, is shown in Figure 4.8.

The π^0 reconstruction efficiency convoluted with acceptance for each p_T bin (Figure 4.9) was calculated as a ratio of the yield, shown in Figure 4.7, to the weighted number of events shown in Figure 4.8. The π^0 reconstruction efficiencies for HighTower-1 and HighTower-2 triggered events were calculated assuming π^0 as the trigger particle. Following this assumption, an additional event cut was introduced – at least one of the BEMC points, associated with one of the π^0 daughter γ's, must contain a tower with sufficient energy to satisfy the corresponding trigger condition.

The calculation of corrections for p+p data was carried out in the same way as it was done for the d+Au data. The resulting corrections are shown in Figure

---

[6]p_T bin widths and positions were set identical to those used in the real data analysis.
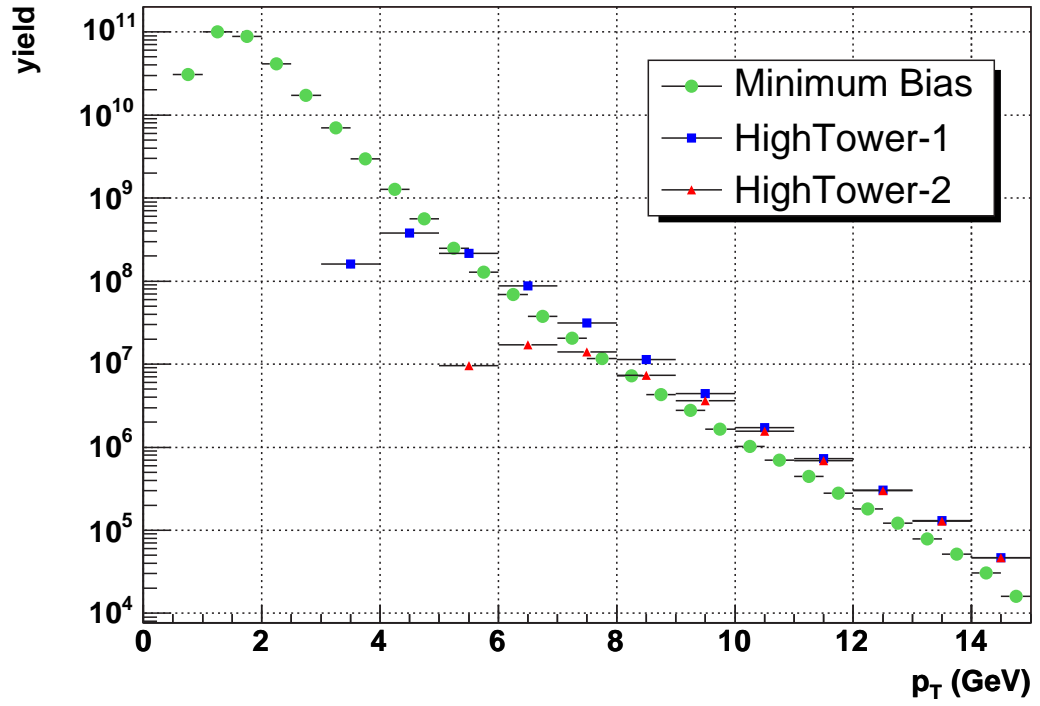
Figure 4.7: Simulated π^0 yield used for calculating efficiency and acceptance corrections to the raw (uncorrected) π^0 yield in d+Au.
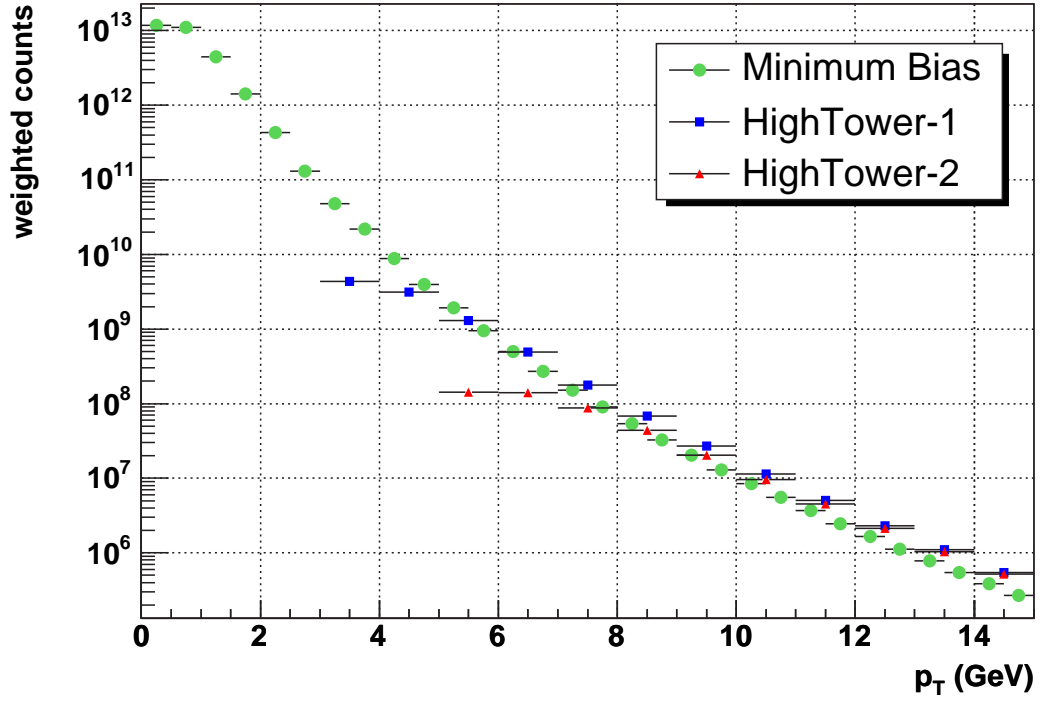
Figure 4.8: Number of events with simulated π^0, passing the z-vertex cut, weighted according to the charged hadron p_T spectrum, with 3-momentum vector of the simulated π^0 pointing into the detector acceptance. The plotted quantity was used as the denominator in the expression for calculating the efficiency and acceptance corrections to the raw d+Au yield.
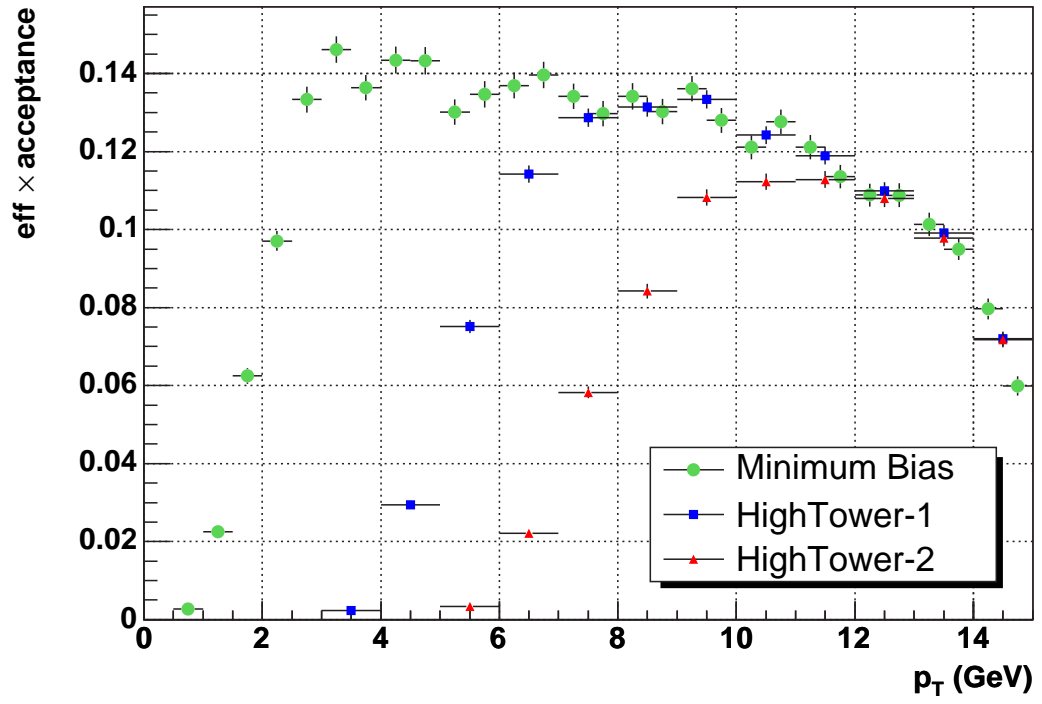
Figure 4.9: Efficiency and acceptance corrections to the raw π^0 yield in d+Au collisions.

4.10. Notice the systematic difference above approximately 10 GeV in p_T between minimum bias and HighTower-1 corrections (where HighTower-1 trigger efficiency is close to 100%) resulting from the difference in time-averaged acceptance for these two types of triggers.
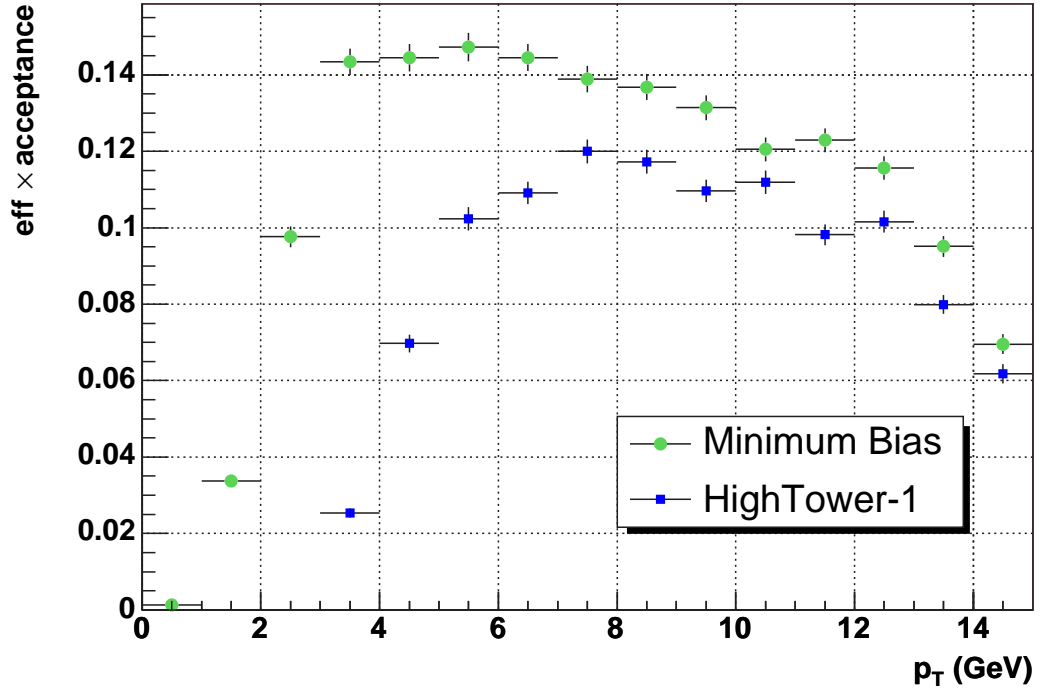
Figure 4.10: Efficiency and acceptance corrections to the raw π^0 yield in p+p collisions.

4.3.8 Comparison With Real Data

The quality of the Monte-Carlo simulations can be assessed by comparing the shapes of various distributions obtained from the simulations to those from the real data. If the detector response is simulated correctly, key features of the distributions will match those obtained from real data.

The distributions of BEMC points in η and ϕ, shown in Figure 4.11, demonstrate reasonable agreement between the real and the simulated detector acceptance.
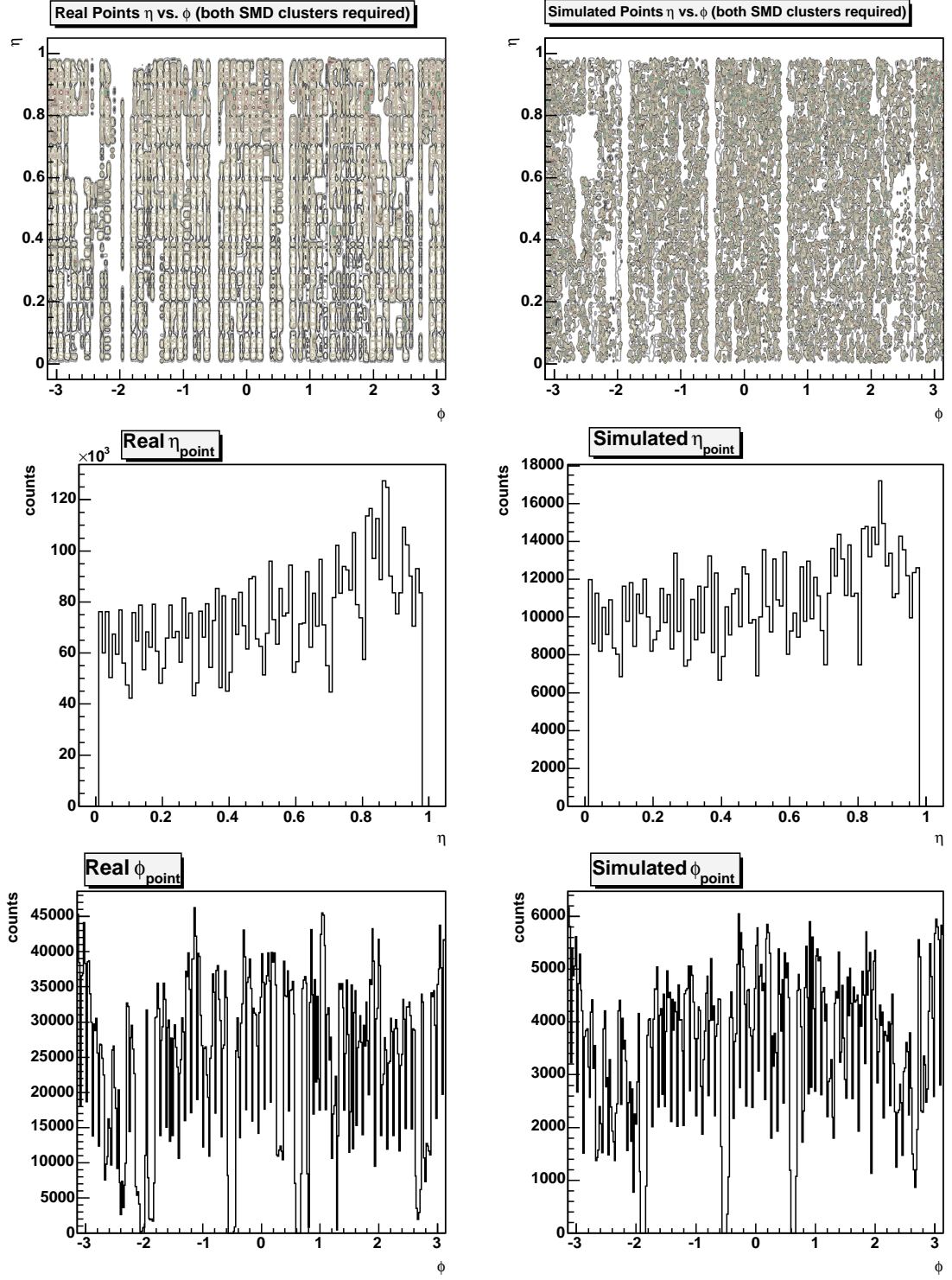
Figure 4.11: Distributions of the BEMC points in η and ϕ for real (minimum bias events from d + Au 2003 run) and simulated data. The plots in the top panel show the maps of the real (left) and simulated (right) detector acceptance.

The comparison of π^0 energy asymmetry $\epsilon_{\gamma\gamma}$ distributions was made between the minimum bias events and the embedded π^0 events for several different p_T intervals. To select as pure a sample of π^0's from the real data as possible, while maintaining nearly 100% efficiency, all pairs of BEMC points with $0.1 < m_{\gamma\gamma} < 0.2$ GeV were selected. This method inevitably results in the contamination of the π^0 sample by the pairs from combinatoric background, for which the selection criterion $0.1 < m_{\gamma\gamma} < 0.2$ GeV is satisfied. However the contributions from the combinatoric background become smaller at higher p_T, and the π^0 sample becomes more pure. All pairs of BEMC points with π^0 daughter γ's associated with them were selected from the embedded events. The resulting energy asymmetry distributions for different transverse momenta of the π^0 are shown in Figure 4.12.

Mean and RMS values were extracted from the Gaussian components of the fits to the invariant mass spectra for both real and embedded data. The p_T dependence of these quantities are shown in Figures 4.13 and 4.14. The reconstructed invariant mass of π^0's with $p_T \lesssim 3$ GeV is affected by the clustering algorithm. Parts of low-energy photon clusters are lost due to the cluster finder thresholds. This gives rise to the observed dependence of reconstructed π^0 mass peak centroid vs. p_T (Figure 4.13). At higher values of p_T, the reconstructed invariant mass is affected by the cluster finder thresholds, but to a lesser degree.

4.4   Fully Corrected π^0 Per-Event Yield

This section explains how fully corrected π^0 yield per minimum-bias-triggered event as a function of π^0 p_T, is calculated from the raw yield by applying corrections. Efficiency and acceptance corrections were described earlier in this chapter. All other corrections will be discussed.
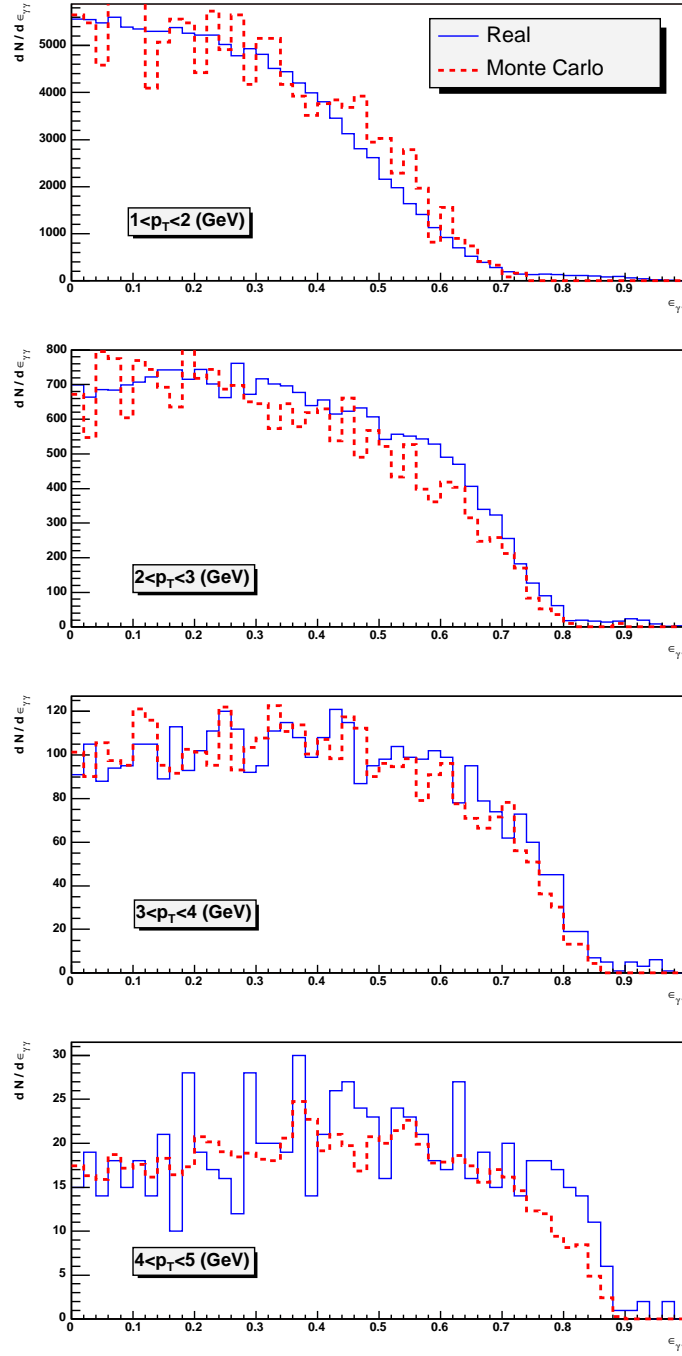
Figure 4.12: π^0 energy asymmetry distributions in several p_T intervals for real (minimum bias from d + Au 2003 run) and simulated data. π^0's from the real data were selected by making an invariant mass cut $0.1 < m_{\gamma\gamma} < 0.2$ GeV. The plots for the simulated data were scaled to match the statistics of the real data for easier comparison.
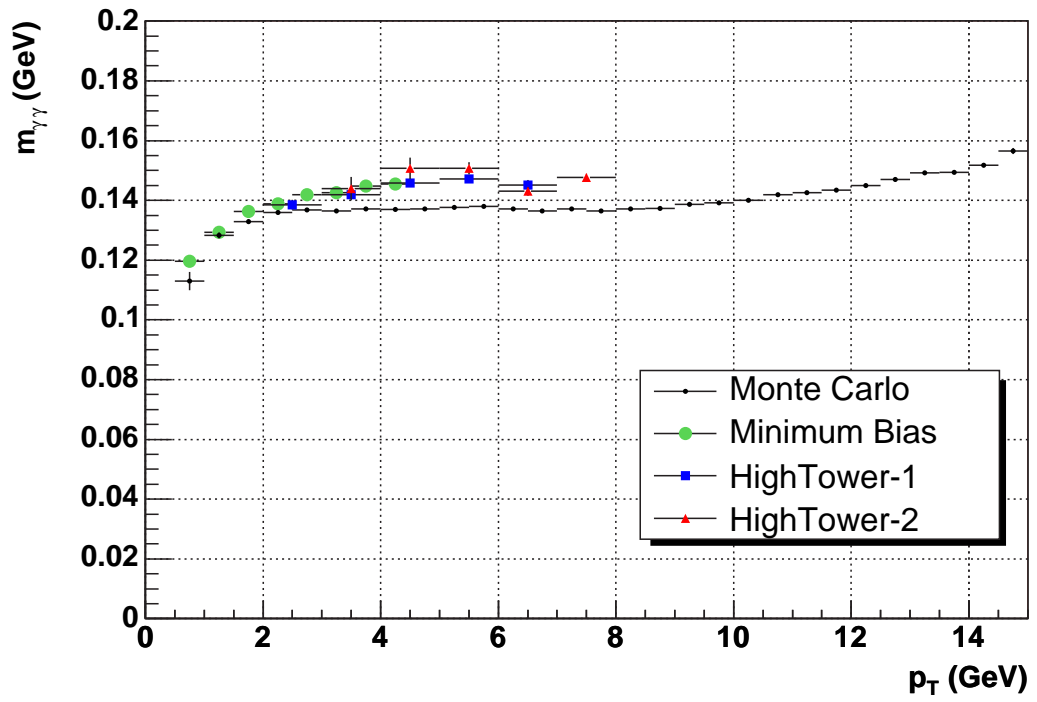
Figure 4.13: π^0 invariant mass peak position as a function of p_T for real (minimum bias, HighTower-1, and HighTower-2 from d+Au 2003 run) and simulated data.
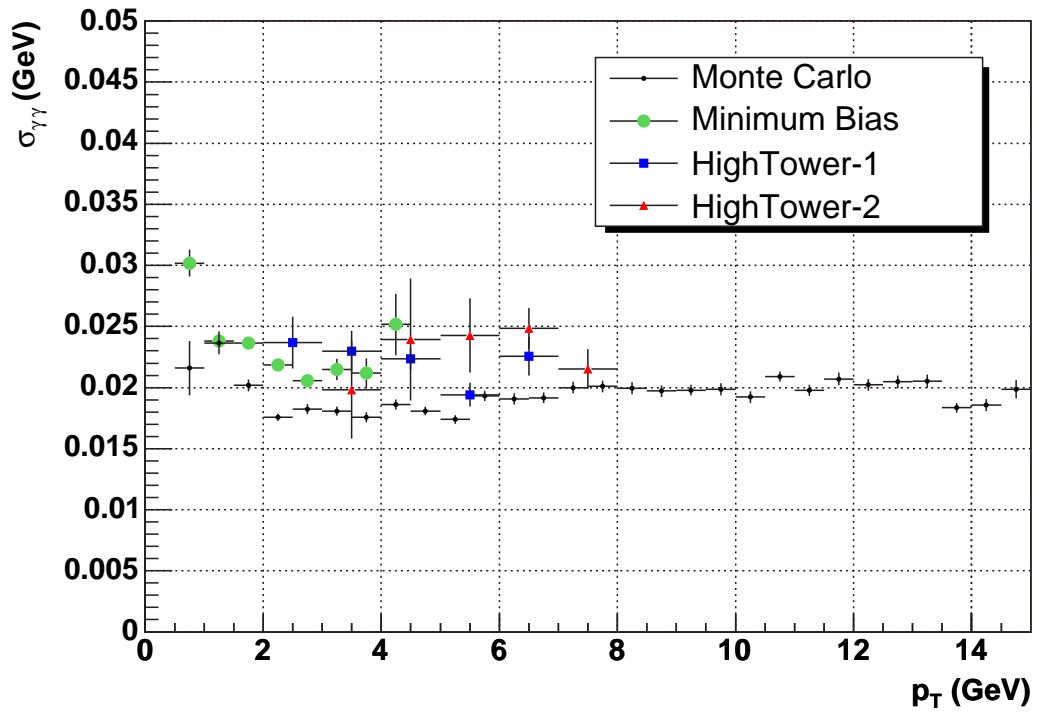
Figure 4.14: RMS of the π^0 peak as a function of p_T for real (minimum bias, HighTower-1, and HighTower-2 from d+Au 2003 run) and simulated data.

4.4.1   Mean-p_T Correction

Since the π^0 yield is calculated in p_T bins of finite width, the question arises, which p_T value from a given p_T interval is to be used to represent the corresponding data point on the plot. The centers of p_T bins do not correspond to the *mean p_T* of the particles in this bin. This is especially true for steeply falling spectra, such as a π^0 yield vs. p_T. As described in Section 4.2, the π^0 yield is extracted from the invariant mass distributions accumulated in different p_T bins. There is no single-particle identification involved, and therefore there is no way of knowing the momenta of the individual π^0's comprising this distribution.

The true shape of the π^0 p_T spectrum is unknown but, for the purpose of estimating the p_T corrections, can be approximated by the spectrum with π^0 yield values plotted in the centers of p_T bins. The spectrum is then fitted with a function

$$f\left(p_T\right) = A\left(1 + \frac{p_T}{B}\right)^{-n},\tag{4.6}$$

where parameters A, B, and n are allowed to vary. The corrected p_T value for a bin with $p_T^{low} < p_T < p_T^{high}$ is given by the average p_T, assuming the distribution given by Eq. 4.6:

$$\langle p_T\rangle = \frac{\displaystyle\int\limits_{p_T^{low}}^{p_T^{high}} p_T f\left(p_T\right) dp_T}{\displaystyle\int\limits_{p_T^{low}}^{p_T^{high}} f\left(p_T\right) dp_T}\ .\tag{4.7}$$

The integrals in Eq. 4.7 can be computed analytically and evaluated by substituting the coefficients obtained from Eq. 4.6. The described procedure is then repeated using the newly obtained $\langle p_T\rangle$ values instead of the centers of the bins, until the changes in $\langle p_T\rangle$ become negligible.

This method of p_T correction is based on the assumption that the local slope of the spectrum, with data points plotted in the centers of p_T bins, is very close to that

of the "true" (though unknown) spectrum. While not unreasonable, this assumption lacks formal justification, and as such remains purely empirical. The shortcomings of this method are especially obvious at large values of p_T, where, in order to achieve sufficient statistics, the p_T bins are chosen to be wider, and the uncertainty of the measurement is large, resulting in substantial uncertainty in the estimate of the slope value, which is critical for this method to work.

4.4.2 Vertex Finding Inefficiency

The primary vertex is not guaranteed to be found in every event. The efficiency of the vertex finding algorithm decreases steeply with decreasing event charged multiplicity. Over 80% of the events where the primary vertex was not found had fewer than three tracks in the TPC [44]. The vertex was reconstructed in $93 \pm 1\%$ of triggered minimum bias d+Au events [30]. In p+p collisions the average multiplicity is lower, resulting in approximately 14% of events without a reconstructed primary vertex [44].

Since most of the events without a primary vertex are very low charged multiplicity events, it is assumed that the contribution to the π^0 yield from such events is negligible. The resulting correction changes the normalization for the π^0 yield in all p_T bins by a constant factor.

4.4.3 Application of the Corrections

Corrections to the raw π^0 yield are summarized by the following expression:

$$\frac{1}{2\pi p_T} \cdot \frac{d^2N}{dp_T d\eta} = \frac{N_{raw}(p_T, \eta)}{\Delta p_T \Delta \eta} \times \frac{1}{2\pi p_T} \times F \times \frac{1}{\epsilon_{reco}} \times \frac{1}{\epsilon_{vtx}} \times \frac{1}{\Gamma_{\gamma\gamma}/\Gamma}, \qquad (4.8)$$

where the quantity on the left-hand side of the expression is the fully corrected π^0 per-event yield, $\frac{N_{raw}(p_T,\eta)}{\Delta p_T \Delta \eta}$ is the raw yield of π^0's with transverse momentum

$(p_T^* - \Delta p_T/2) < p_T < (p_T^* + \Delta p_T/2)$, where p_T^* is the bin center, F stands for the normalization factor F_{MB} (Eq. 4.4) or F_{HT_k} (Eq. 4.5) for the appropriate trigger condition, ϵ_{reco} is the π^0 reconstruction efficiency convoluted with acceptance, ϵ_{vtx} is the primary vertex finding efficiency, and $\Gamma_{\gamma\gamma}/\Gamma = 0.98798 \pm 0.00032$ is the branching ratio of the neutral pion into two photons [45]. The correction for losses of π^0's due to conversion of one or both daughter photons is included in ϵ_{reco}. p_T values are taken at the centers of the bins, and then replaced by mean-p_T values calculated according to the prescription given in Section 4.4.1.

Fully corrected π^0 yield per minimum bias triggered event in p+p and d+Au collisions is shown in Figure 4.15 and listed in tables presented in Appendix B. The data are fitted with functions of the following form:

$$f\left(p_T\right) = A \left(1 + \frac{p_T}{p_0}\right)^{-n},\tag{4.9}$$

where parameters A, p_0, and n are allowed to vary.

4.5 Systematic Uncertainties

For this analysis, an attempt was made to place an upper limit on the systematic uncertainty.

4.5.1 Invariant Mass Peak Fitting Uncertainties

The main contribution to the systematic error comes from the fitting uncertainties. Due to the statistical fluctuations in the shape of the invariant mass distributions, the fit function does not reproduce their precise shape; this inaccuracy being one source of the fitting uncertainties. Another source is the unknown shape of the combinatoric background in the peak region. It is assumed that the background can be estimated by fitting the $m_{\gamma\gamma}$ distributions in the regions outside the π^0 peak and extending
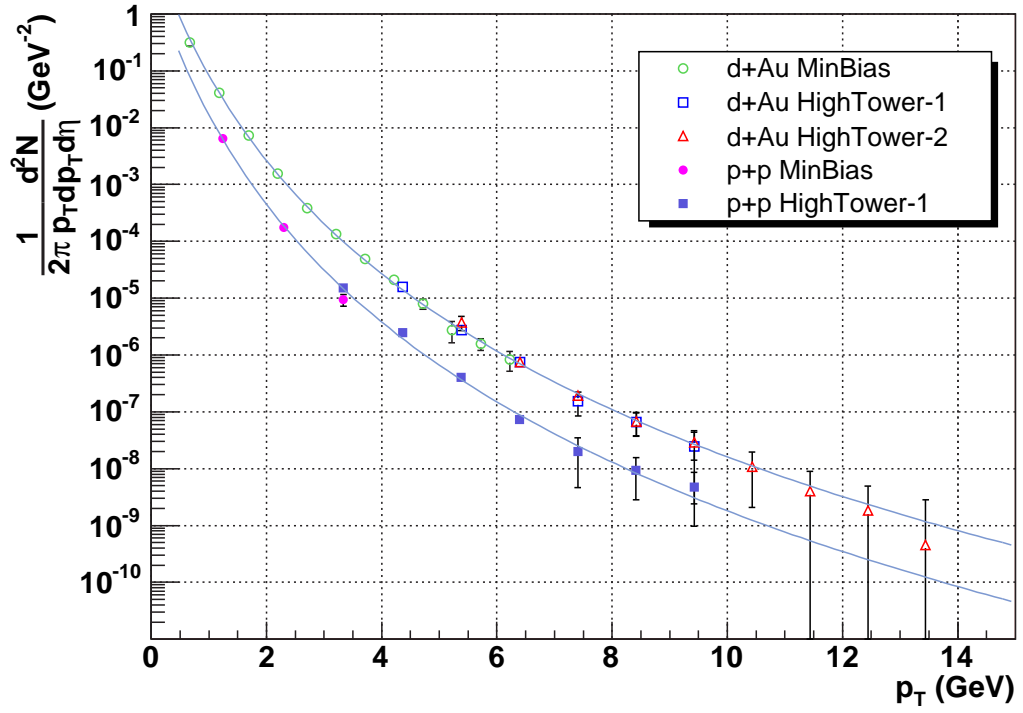
Figure 4.15: Fully corrected π^0 yield per minimum bias triggered event in p+p and d+Au collisions plotted as a function of π^0 transverse momentum. Fits to the data are shown to guide the eye and help distinguish between p+p and d+Au data points.

the fit functions into the peak region. This is in part justified by the shape of the high-mass combinatoric background, which is known from the mixed-event analysis [38]. The remaining low-mass background from the split clusters is well fitted by a decaying exponential at low and intermediate p_T, while at higher p_T this method suffers from low statistics and lack of "clean" low-mass background, necessary to make a reliable fit. An upper limit on the systematic uncertainty of the π^0 yield at high-p_T is estimated to be about 50% of the amount of the background in the signal region, which translates to over $\sim 100\%$ uncertainty for $p_T > 10$ GeV for d+Au data set. Such a large systematic error is deemed necessary due to the ambiguity in estimating the background shape.

Uncertainties from the fits to the simulated invariant mass distributions, used in the calculation of the corrections to the raw yield, were also estimated and propagated to the end results.

4.5.2 Analysis-Related Uncertainties

Early in the analysis an approximately 20% systematic mismatch in the π^0 yield was seen between the minimum bias triggered and HighTower-1 triggered d+Au events in the same p_T bins, whereas the data points from HighTower-1 and HighTower-2 were in a good agreement. This mismatch was removed by rejecting runs where the number of π^0 candidate pairs per minimum bias triggered event was substantially lower than the average. The problem was tracked down to the corrupt SMD pedestal table affecting the off-line production of the data from the beginning of the d+Au experimental run. The high-tower trigger was in the commissioning stage in the beginning of the run, and was rarely used in the data-taking. This explains why the high-tower triggered data was less affected by the corrupt SMD pedestal table.

The remaining variations in the N_{pairs}/N_{MB} ratio (Figure 4.6) are attributed to the changes in the detector acceptance; their effect was absorbed into the efficiency
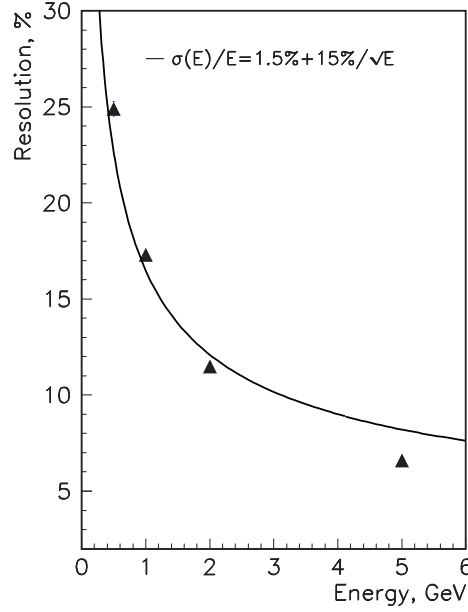
Figure 4.16: Energy dependence of the Barrel EMC energy resolution.

× acceptance corrections calculated using the time-dependent status tables.

4.5.3 Detector-Related Uncertainties

The BEMC tower energy resolution was estimated from the test beam measurements [46]. In these tests, the prototype of the BEMC module performance was studied with 0.5 GeV, 1 GeV, 2 GeV, and 5 GeV electron beams. The energy resolution was estimated to be about $16\%/\sqrt{E}$, where E is the energy of the electron in GeV. The energy dependence of the resolution, $\sigma(E)/E$, is shown in Figure 4.16. Applied to the π^0 analysis, this resolution results in an uncertainty on the reconstructed π^0 transverse momentum. The BEMC energy resolution is taken into account in the Monte Carlo simulations of the detector response. Since the energy resolution affects the π^0 invariant mass peak width, the peak width from the simulations should be consistent with the data if the detector response is simulated accurately. Figure 4.14 demonstrates good agreement between the real data and the simulations. The uncertainty, resulting from the energy resolution, is absorbed into the uncertainty of π^0 reconstruction efficiency.

4.6   Nuclear Modification Factor

The effects of nuclear medium on high-p_T particle production are quantified by the nuclear modification factor R_{dA}. It was already introduced in Section 2.2, but we will rewrite it here for convenience, with the only difference from Eq. 2.8 that the normalization factor $1/N_{dA}^{evt}$ is absorbed into N_{dA}:

$$R_{dA}(p_T) = \frac{d^2 N_{dA}/d\eta dp_T}{\left(\langle N_{coll}\rangle/\sigma_{pp}^{inel}\right) \times d^2\sigma_{pp}/d\eta dp_T},$$ (4.10)

where $\langle N_{coll}\rangle$ is the average number of inelastic nucleon-nucleon collisions per event in minimum bias d+Au collisions, and $\langle N_{coll}\rangle/\sigma_{pp}^{inel}$ is the nuclear overlap function $\langle T_{dA}(b)\rangle$. The quantity in the numerator is the π^0 yield per minimum bias triggered d+Au event. $d^2\sigma_{pp}/d\eta dp_T$ is the π^0 differential cross section in inelastic p+p collisions. $\langle N_{coll}\rangle$ is estimated using a Monte Carlo Glauber calculation[7] incorporating Hulthèn wave function of the deuteron [48, 49]. The Glauber calculation was performed with $\sigma_{pp}^{inel} = 42 \pm 1$ mb [50]. We used $\langle N_{coll}\rangle = 7.5 \pm 0.4$, quoted in [30], which is the "official" number used in the publications by the STAR Collaboration. An extended review of Glauber model and further references can be found in [51] and [6].

A brief discussion of the normalization and why the quantity R_{dA} is constructed in such a way seems to be appropriate here. The purpose of constructing R_{dA} is to compare the particle yield in d+Au collisions to that in p+p. If the outcome of an average d+Au collision could be represented by the superposition of $\langle N_{coll}\rangle$ uncorrelated inelastic p+p collisions, then R_{dA} would be equal to one. Deviations from unity indicate the presence of nuclear effects. We arrive at the following intuitive definition of nuclear modification factor:

$$R_{dA} = \frac{d^2 N_{dA}/d\eta dp_T}{\langle N_{coll}\rangle d^2 N_{pp}^{inel}/d\eta dp_T},$$ (4.11)

---

[7]A group of approximations for calculating cross sections in nuclear collisions (Glauber theory) stems from original work by R. J. Glauber [47].

where $d^2 N_{pp}^{inel}/d\eta dp_T$ is the yield per inelastic p+p collision. We notice that Eq. 4.11 becomes identical to Eq. 4.10 by making the substitution:

$$\frac{d^2 N_{pp}^{inel}}{d\eta dp_T} = \frac{1}{\sigma_{pp}^{inel}} \cdot \frac{d^2\sigma_{pp}}{d\eta dp_T}. \tag{4.12}$$

All that is left to do, is to relate $d^2\sigma_{pp}/d\eta dp_T$ to the measured quantity, which is the yield per triggered collision, $d^2 N_{meas}/d\eta dp_T$. First, we make an assumption that $d^2\sigma_{inel}/d\eta dp_T = d^2\sigma_{NSD}/d\eta dp_T$, where σ_{NSD} is the p+p non-singly diffractive cross section defined in 3.3.2. On average, singly diffractive events have less than 1 charged track within $|\eta| < 1$ per event. The contribution from singly diffractive events to the particle spectra is estimated to be of order 1%. Since singly diffractive events lead to a softer spectrum than NSD events, this effect is expected to be even smaller at high p_T. Second, it is assumed that there is no background in the BBC from singly diffractive events, $\sigma^{BBC} = \sigma_{NSD}^{BBC}$. Third, we assume that the measured quantity $d^2 N_{meas}/d\eta dp_T$ is the yield per NSD event, $d^2 N_{NSD}/d\eta dp_T = d^2 N_{meas}/d\eta dp_T$. Now the differential inelastic cross section is given by:

$$\frac{d^2\sigma_{pp}}{d\eta dp_T} \approx \frac{d^2\sigma_{NSD}}{d\eta dp_T} \tag{4.13}$$

$$\approx \frac{d^2 N_{meas}}{d\eta dp_T} \times \sigma_{NSD}^{BBC} / \left(\frac{d^2\sigma_{NSD}^{BBC}}{d\eta dp_T} \middle/ \frac{d^2\sigma_{NSD}}{d\eta dp_T} \right)_{est}, \tag{4.14}$$

where $\sigma_{NSD}^{BBC} = 26.9 \pm 1.9$ mb, as measured by a van der Meer scan [52], and the expression in parentheses is the BBC acceptance correction – the ratio of differential cross section with and without the requirement of the BBC coincidence – which was estimated via Monte Carlo to be 0.87 ± 0.08 and independent of p_T.

We adopt the normalization uncertainty for d+Au data from [30], where it is estimated to be 10%. The p+p NSD differential cross section $d^2\sigma_{NSD}/d\eta dp_T$ (Eq. 4.13) has a normalization uncertainty of $\pm 14\%$ [53]. We add these uncertainties in quadra-
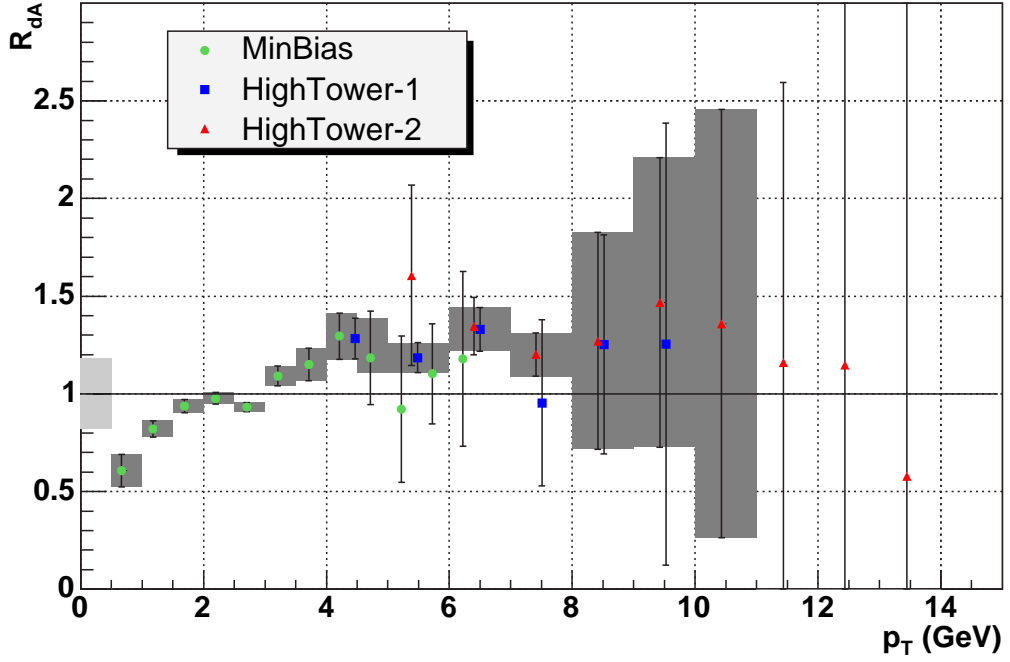
Figure 4.17: Nuclear modification factor (R_{dA}), defined as the ratio of invariant yield in d+Au to that of p+p. Error bars include both statistical and systematic uncertainties that vary from point to point in p_T. Systematic errors which are correlated from point to point are represented by the shaded band around unity at $p_T = 0$. Shaded bands are shown around data points with the smallest uncertainty in the corresponding p_T interval. HighTower-1 data points are shifted by 100 MeV for clarity.

ture to obtain the total normalization uncertainty $\pm 17\%$ for R_{dA}. Combined with the 5% uncertainty on the number of binary collisions $\langle N_{coll} \rangle$, the total uncertainty for R_{dA}, common for all values of p_T, is estimated to be $\pm 18\%$. This value of uncertainty does not include the uncertainties that vary point-to-point. The normalization uncertainties are highly correlated for different data points in p_T.

Transverse momentum dependence of the nuclear modification factor R_{dA} is shown in figure 4.17. The effect of applying the normalization uncertainty is to multiply each data point by a constant factor 1 ± 0.18.

CHAPTER 5

DISCUSSION

In this chapter we compare the results, presented in Sections 4.4 and 4.6, to theory and earlier experimental measurements. We also discuss the results in the broader context of RHIC physics.

5.1   Comparison to Theory

The cross sections for inclusive high p_T particle production in high energy p+p collisions can be calculated theoretically using the factorization approach discussed in Section 2.1. The factorization theorem states that reactions involving large momentum transfer may be factorized into long-distance and short-distance parts. The long-distance parts contain the information on the parton structure of the nucleon in terms of its structure functions $f_A^a(x_a)$, and information on how the partons fragment into final-state hadrons in terms of the fragmentation functions $D_c^C(z_c)$. The structure functions and the fragmentation functions are universal, i.e., they are independent of the process considered. The short-distance part deals with the hard interactions of the partons, and can be evaluated using perturbative QCD theory.

The factorization procedure requires that an arbitrary scale, of the order of the hard scale in the reaction, is introduced. The choice of the *factorization scale* is not specified by the factorization procedure. The factorization scale (μ_F) separates the hard (short-distance) partonic processes, calculable using pQCD, from the soft (long-

distance) processes. The soft processes are determined by $f_A^a(x_a, \mu_F)$ and $D_c^C(z_c, \mu_F)$, which are determined experimentally. In fact, the factorization scale for the initial-state partons (μ_F), does not have to match the scale (μ_F') for the absorption of long-distance effects into the fragmentation functions. In addition, there is a renormalization scale (μ_R) associated with the running of the strong coupling constant α_s.

Following the factorization theorem, we rewrite Eq. 2.5 for the process $pp \to \pi^0 X$ as follows:

$$E_{\pi^0}\frac{d\sigma_{pp \to \pi^0 X}}{d^3 p_{\pi^0}} = \sum_{abcd} \int\limits_0^1 dx_a \int\limits_0^1 dx_b f_p^a(x_a, \mu_F) f_p^b(x_b, \mu_F) \frac{1}{\pi z_c} \frac{d\sigma_{ab \to cd}}{d\bar{t}} D_c^{\pi^0}(z_c, \mu_F'). \quad (5.1)$$

The cross sections for the partonic sub-process $ab \to cd$ may be evaluated in pQCD. The leading-order (LO) approximation can generally only serve to give a rough description of the reaction under study [54]. The next-to-leading order (NLO) calculations are necessary in order to reduce the dependence of the result on the unphysical factorization and renormalization scales. The knowledge of the NLO corrections is also necessary to reliably extract the information on the parton distribution functions from the experimental data.

Ideally, the results of the calculations must be independent of the scale parameters. By varying the scales μ_F, μ_F' and μ_R, the stability of the calculations can be tested. Obtaining the result with different scale values is a common way of estimating the theoretical uncertainties of the calculation.

Figure 5.1 shows the invariant differential cross section for inclusive π^0 production, plotted together with the results from NLO pQCD calculations, in which fully analytical expressions for the underlying partonic hard-scattering cross sections were used [55, 54]. The theoretical curves are taken from [56]. These calculations were performed with equal renormalization and factorization scales of p_T, the structure
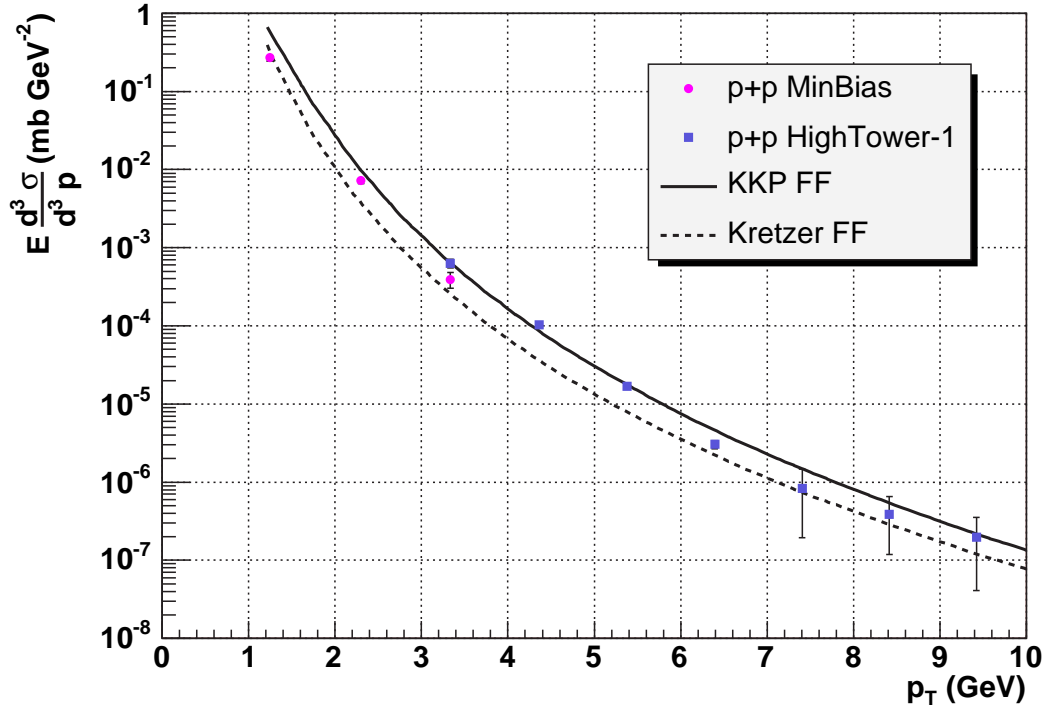
Figure 5.1: The invariant differential cross section for inclusive π^0 production, and the results from NLO pQCD calculations. The theoretical calculations were performed with equal renormalization and factorization scales of p_T, using the "Kniehl-Kramer-Pötter" (solid line) and "Kretzer" (dashed line) sets of fragmentation functions. The normalization uncertainty of 14% is not shown. The theoretical curves are taken from [56].

functions from the CTEQ6M collaboration [5], and two sets of fragmentation functions. Ref. [54] states that "the cross section for p_T values smaller than about 2 GeV is outside the domain of perturbative calculations". This statement is deduced from the relative size of the NLO corrections, which stays nearly constant at $p_T \gtrsim 4$ GeV, but increases rapidly at $p_T \lesssim 3$ GeV. Despite this warning, the theoretical calculations are consistent with the data even at relatively low p_T. According to Ref. [56], the calculations vary by about 15% with the choice of structure functions, whereas they change considerably with the choice of fragmentation functions. Theoretical calculations shown in Figure 5.1 were performed with the "Kniehl-Kramer-Pötter" (KKP) [11] and with "Kretzer" [7] sets of fragmentation functions. These sets differ mainly in that the gluon-to-pion fragmentation function (D_g^π) is greater in the KKP set [56]. Figure 5.2 shows the relative difference between the data and the theory using KKP and Kretzer fragmentation functions. The agreement is better with the KKP set. The normalization uncertainty of 14% is not shown.

5.2   Comparison to Earlier Experimental Measurements

Neutral pion production was previously measured by the PHENIX collaboration in p+p [56] and d+Au [20] collisions at center-of-mass energy $\sqrt{s_{NN}} = 200$ GeV per nucleon. These data provide an excellent opportunity to compare the results measured by two different experiments at the same center-of-mass energy.

The comparison of p+p and d+Au results is shown in Figures 5.3 and 5.4 respectively. In both cases, the relative difference between our results and the fits to the PHENIX data demonstrates good agreement. The nuclear modification factor (Figure 4.17) is in agreement, within errors, with R_{dA} measured by the PHENIX collaboration (Figure 2.10).
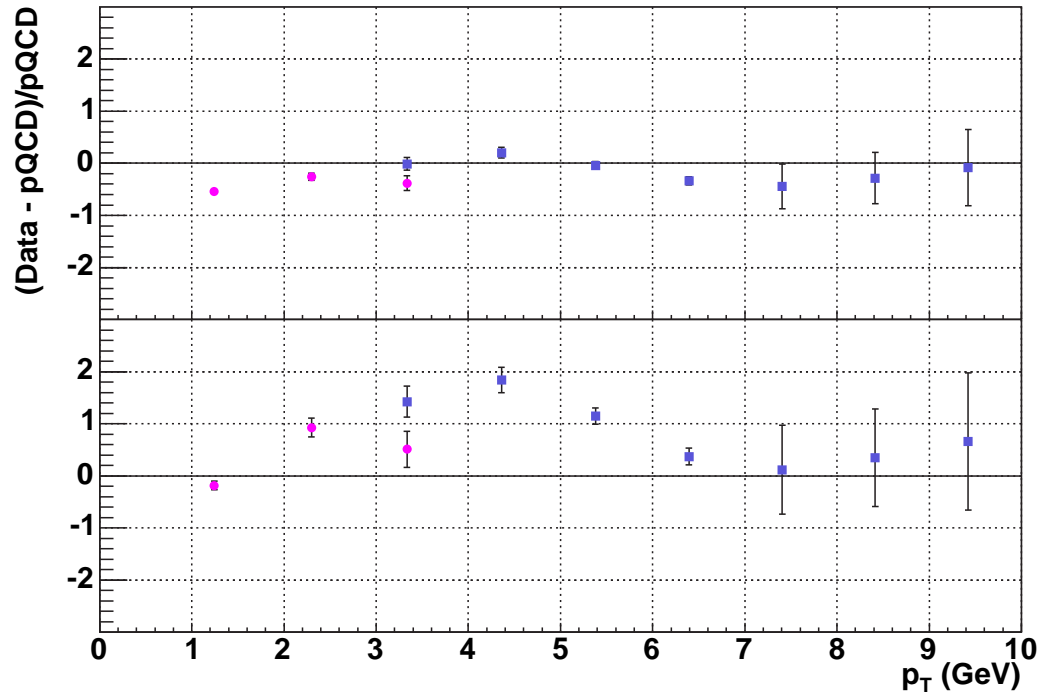
Figure 5.2: The relative difference between the data and the theory using KKP (upper panel) and Kretzer (lower panel) fragmentation functions. The normalization uncertainty of 14% is not shown.
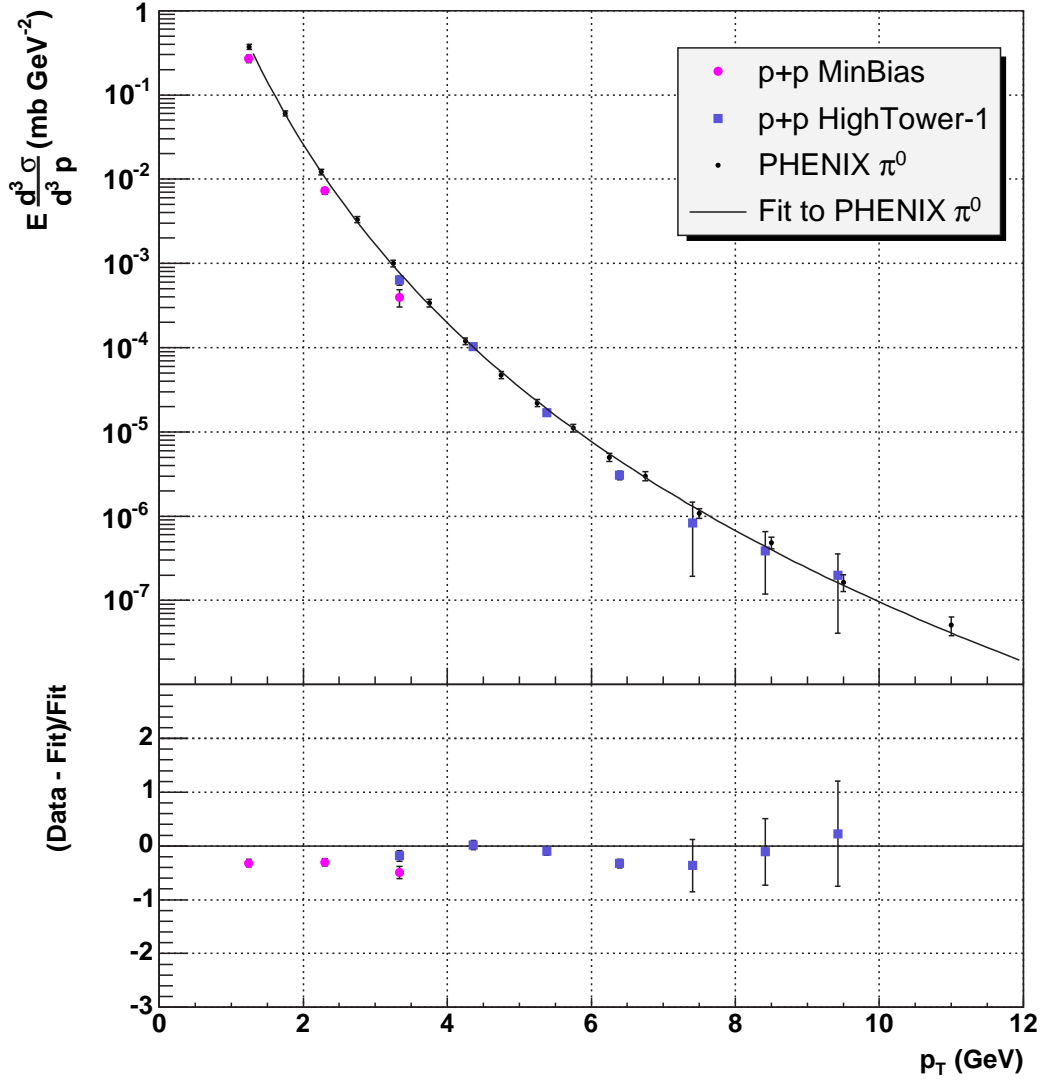
Figure 5.3: The STAR invariant differential cross section for inclusive π^0 production in p+p collisions, plotted together with results from the PHENIX collaboration [56] (upper panel). The relative difference between STAR data and the fit to the PHENIX results is shown in the lower panel. The normalization uncertainties are not shown.
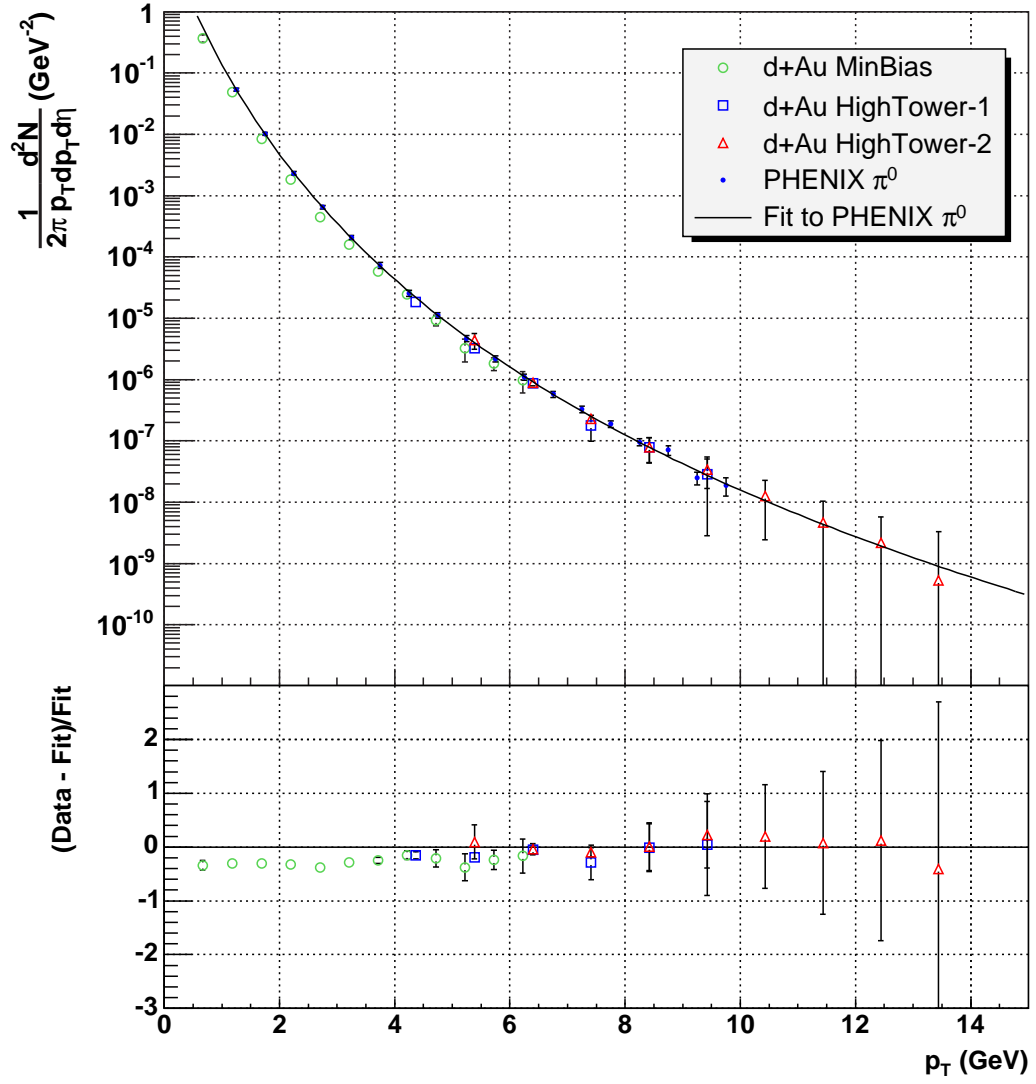
Figure 5.4: The π^0 invariant yield per event in d+Au collisions at STAR, plotted together with PHENIX results [20] (upper panel). The relative difference between STAR data and the fit to the PHENIX results is shown in the lower panel. The normalization uncertainties are not shown.

5.3 R_{dA}: the Implications of the Measurement

The main purpose of d+Au run at RHIC was to disentangle initial and final state effects of the Au+Au collisions. Of special interest was the interpretation of suppression of high p_T particle yields observed in central Au+Au collisions. Before the data from RHIC d+Au run were analyzed, several competing theoretical models attempted to explain the observed suppression of high p_T particle production in Au+Au collisions. Along with the "traditional" explanation[1] via *jet quenching* mechanism [25, 26], several "alternative" scenarios were suggested. These theoretical predictions, rather formally, can be divided into two categories: those employing initial-state, and those employing final-state mechanisms for explaining the high p_T hadron suppression. We will proceed with a brief review of some of these models.

It was suggested [57] that *gluon saturation*, occurring prior to hard scattering of the partons, could explain the observed suppression of particle production at high p_T. Gluon saturation is strong nuclear shadowing and arises from modification of parton structure functions of the nucleon within a nucleus, compared to a free nucleon at low x. It was already mentioned in Section 2.1 that the proton structure is dominated by gluons at $x \lesssim 10^{-1}$. When bound within a nucleus, the gluon wave functions overlap, and the probability of two-gluon fusion becomes large. The process of gluon fusion effectively limits the number of gluons in a nucleus. The calculations presented in [57] lead to the high p_T particle suppression in Au+Au as a consequence. Since gluon saturation is a property of the nuclear wavefunction, there should be a corresponding effect in d+Au collisions. The saturation model predicted about 30% *suppression* of high p_T particles in d+Au collisions at RHIC energies. Other theoretical models based on pQCD calculations predicted an *enhancement* of particle yields due to the Cronin effect [58, 59]. The data shown in Figure 2.7 and Figure 4.17 rule

---

[1]Jet quenching mechanism was originally [25] proposed more than a decade before the data from Au+Au collisions at RHIC became available.

out the suppression prediction and favor the pQCD predictions stemming from p_T broadening effects.

The idea behind jet quenching is that hard-scattered partons, responsible for high p_T particle production, lose energy via induced gluon radiation as they propagate in the dense colored medium. In this picture partons lose energy first and then hadronize outside of the dense medium in the same way as in the vacuum. The final fragmentation of the leading parton gives rise to particles with considerably lower energies. It is reasonable to ask whether leading hadrons from the jet fragmentation could have strong interaction with the medium and whether hadron absorption could be the main cause for the observed high p_T particle suppression. This question is closely related to the size of the medium produced in Au+Au reactions and to the time it takes for a parton to fragment into hadrons. While different theoretical models agree on the size of the medium, which is typically taken as about 10 fm, there is a substantial disagreement in the estimates of fragmentation time t_F, ranging from 10 to 50 fm/c for a hadron with $p_T \approx 10$ GeV [60, 61]. High theoretical uncertainty in the estimates of t_F arises from the fact that the hadronization process takes place in the non-perturbative regime, and therefore it is not directly accessible by pQCD calculations. The "border" between non-perturbative and perturbative regimes is defined by the (arbitrary) choice of the factorization scale Λ_{QCD}. By using different values of Λ_{QCD}, Gallmeister et al. [60] and Wang [61] arrive at different estimates of t_F. If the value of t_F is small enough, the hadronization occurs already *inside* the late stage hadronic fireball.

Gallmeister et al. [60] argue that the suppression of high-p_T hadrons in central Au+Au collisions at RHIC can be explained by energy loss via *hadronic* interactions of the partons fragmenting inside the medium. Theoretical considerations of this model require the density of hadrons in the late fireball to be changing from 1 fm^{-3} to 0.1 fm^{-3} in order to make the system opaque to the leading hadrons, so that

sufficient reduction in hadron momenta would result. These conditions are satisfied in d+Au collisions, where the density of nucleons within a Au nucleus is about 1 fm^{-3}. Therefore the mechanism of hadronic energy loss should result in suppression of high p_T particle spectra in d+Au. This is clearly in contradiction with results shown in Figure 4.17.

5.3.1 Final Remarks

The results presented in this dissertation are in agreement with NLO pQCD calculations and earlier measurements by STAR [30] and the other three RHIC experiments [20, 62, 63]. The invariant π^0 yield, measured in d+Au collisions at $\sqrt{s_{NN}} = 200$ GeV, does not show any suppression up to 8 GeV when compared to the π^0 yield in p+p at the same center-of-mass energy, scaled by the number of binary collisions. We conclude that the suppression of high p_T particle spectra, observed in Au+Au collisions at $\sqrt{s_{NN}} = 200$ GeV at RHIC, is best described by medium-induced radiative parton energy loss, leading to the modification of the jet fragmentation functions.

APPENDIX A

RELATIVISTIC KINEMATICS

A.1   Lorentz Transformations

The energy E and 3-momentum $\mathbf{p}$ of a particle of mass m form the 4-vector $p = (E,\mathbf{p})$, whose square $p^2 \equiv E^2 - |\mathbf{p}|^2 = m^2$. The velocity of the particle is $\beta = \mathbf{p}/E$. The energy and momentum $(E^*, \mathbf{p}^*)$ viewed from a frame moving with a velocity β_f are given by

$$\begin{pmatrix} E^* \\ p_\parallel^* \end{pmatrix} = \begin{pmatrix} \gamma_f & -\gamma_f \beta_f \\ -\gamma_f \beta_f & \gamma_f \end{pmatrix} \begin{pmatrix} E \\ p_\parallel \end{pmatrix} , \ p_t^* = p_t \tag{A.1}$$

where $\gamma_f = 1/\sqrt{1 - \beta_f^2}$ and $p_t(p_\parallel)$ are the components of $\mathbf{p}$ perpendicular (parallel) to β_f. Other 4-vectors, such as the space-time coordinates of events transform in the same manner. The scalar product of two 4-momenta $p_1 \cdot p_2 = E_1 E_2 - \mathbf{p}_1 \cdot \mathbf{p}_2$ is invariant (frame independent).

A.2   Kinematic Variables

The momentum components p_x and p_y are unchanged by a boost along z, so the transverse momentum of a particle defined as

$$p_T \equiv \sqrt{p_x^2 + p_y^2} \tag{A.2}$$

is boost-invariant.

The transverse mass of a particle of mass m is defined as

$$m_T \equiv \sqrt{p_T^2 + m^2}. \qquad (A.3)$$

The longitudinal variable commonly used is rapidity,

$$y \equiv \frac{1}{2} \ln \left(\frac{E + p_z}{E - p_z} \right), \qquad (A.4)$$

which is additive under Lorentz transformations along z.

Using m_T, the expression for rapidity may be written as

$$y \equiv \frac{1}{2} \ln \left(\frac{E + p_z}{m_T} \right). \qquad (A.5)$$

From the above definitions we obtain the following relationships:

$$p_z = m_T \sinh y, \qquad (A.6)$$

$$E = m_T \cosh y. \qquad (A.7)$$

Dividing these, we get

$$\beta_z = \tanh y, \qquad (A.8)$$

which is the longitudinal component of the velocity of a particle of rapidity y in the lab frame. Since rapidity is additive under Lorentz transformations, a change in rapidity corresponds to a boost along the z-direction. A particle of rapidity y in the lab frame will have a rapidity y' in a frame moving with a velocity β_z relative to the lab:

$$y' = y + \tanh^{-1} \beta_z. \qquad (A.9)$$

A related quantity is the pseudo-rapidity η, which is equal to rapidity y in the limit $\beta \to 1$. In order to obtain the expression for η, we first rewrite Eq. A.4 as

$$y = \frac{1}{2} \ln \left(\frac{1 + \beta \cos \theta}{1 - \beta \cos \theta} \right), \tag{A.10}$$

where θ is the angle between β and z in the lab frame. Taking the limit of Eq. A.10 as $\beta \to 1$, we obtain:

$$\eta = - \ln \tan \left(\frac{\theta}{2} \right). \tag{A.11}$$

A.3   Leading Hadron p_T

Consider an inclusive hadronic reaction $AB \to CX$, where hadrons A and B collide at the center-of-mass energy $\sqrt{s}$. The incoming hadrons A and B contain partons a and b which scatter and produce partons c and d which have a large transverse momentum component. Hadron C is a leading particle resulting from the fragmentation of parton c, and X represents all the other final-state particles produced in this reaction (Figure 2.1).

Before the collision, 4-momenta of partons a and b are given by:

$$p_a = \left(x_a \frac{\sqrt{s}}{2}, 0, 0, x_a \frac{\sqrt{s}}{2} \right), \quad p_b = \left(x_b \frac{\sqrt{s}}{2}, 0, 0, -x_b \frac{\sqrt{s}}{2} \right), \tag{A.12}$$

where x_a and x_b are fractional momenta of partons a and b within hadrons A and B. In Eq. A.12 we neglected the masses of partons a and b, and their transverse momentum components with respect to z-axis, which is chosen along the direction of motion of A in the center-of-mass frame. If we require that partons c and d are produced perpendicular to z, their 4-momenta will be given by:

$$p_c = (p_c, p_c, 0, 0), \quad p_d = (-p_d, p_d, 0, 0), \tag{A.13}$$

where p_c and p_d are x-components of momenta of partons c and d, and x-axis is chosen, with no loss of generality, along the direction of motion of parton c.

Energy and momentum conservation yield

$$\frac{\sqrt{s}}{2}(x_a + x_b) = p_c - p_d \tag{A.14}$$

and

$$\frac{\sqrt{s}}{2}(x_a - x_b) = 0, \quad p_c + p_d = 0. \tag{A.15}$$

Transverse momentum p_T of the leading hadron C can be roughly approximated by transverse momentum of parton c,

$$p_T \approx p_c. \tag{A.16}$$

Using Eq. A.14 and Eq. A.15, we readily obtain:

$$x_a = x_b \approx \frac{2p_T}{\sqrt{s}}, \tag{A.17}$$

which is an often-used approximation for leading hadron p_T.

A.4 π^0 Decay Kinematics

Consider a double-photon decay of a π^0 moving with a velocity β along the z-direction with respect to the lab frame. The energies of the decay photons in the π^0 rest frame are given by

$$E^*_{1,2} \equiv E^* = m/2, \tag{A.18}$$

where m is the π^0 mass, and the projections of their momenta on z are given by

$$p^*_{z(1,2)} = \pm E^* \cos\theta^*, \tag{A.19}$$

where and θ^* is the angle between the momentum vector of one of the γ's and z. The photon energies in the lab frame are found by applying the Lorentz boost (Eq. A.1):

$$E_{1,2} = \gamma E^* \pm \beta\gamma E^* \cos\theta^*. \tag{A.20}$$

The photon energy asymmetry (Eq. 4.2) is then given by

$$\epsilon_{\gamma\gamma} \equiv \frac{|E_1 - E_2|}{E_1 + E_2} = \beta\cos\theta^*. \tag{A.21}$$

Since the π^0 decay is isotropic in its rest frame, the decay rate into a solid angle segment $d\Omega^*$ is constant,

$$\frac{dN}{d\Omega^*} = const = \frac{d^2N}{\sin\theta^* d\theta^* d\phi^*}, \tag{A.22}$$

where ϕ^* is the azimuthal angle in the plane perpendicular to z. Integrating in ϕ,

$$\frac{dN}{\sin\theta^* d\theta^*} = \frac{dN}{-d\cos\theta^*} = const. \tag{A.23}$$

It immediately follows from Eq. A.21, that energy asymmetry distribution is flat.

APPENDIX B

TABULATED RESULTS

	p_T bin (GeV)	$\langle p_T \rangle$ (GeV)	inv. yield (GeV^{-2})	error (%)
Minimum Bias	1.0-2.0	1.24	0.00876	10.2
	2.0-3.0	2.30	0.000236	9.5
	3.0-4.0	3.34	1.27e-005	23
HighTower-1	3.0-4.0	3.34	2.04e-005	12.1
	4.0-5.0	4.36	3.32e-006	8.6
	5.0-6.0	5.38	5.48e-007	7.5
	6.0-7.0	6.39	9.85e-008	11.7
	7.0-8.0	7.41	2.68e-008	76.7
	8.0-9.0	8.42	1.25e-008	69.3
	9.0-10.0	9.42	6.43e-009	79.4

Table B.1: Fully corrected π^0 yield per minimum-bias-triggered p+p event. Errors are combined statistical and systematic uncertainties that vary from point to point in p_T. $\langle p_T \rangle$ is the average transverse momentum of π^0's reconstructed in a given p_T bin (see Section 4.4.1 for details).

	p_T bin (GeV)	$\langle p_T \rangle$ (GeV)	inv. yield (GeV^{-2})	error (%)
Minimum Bias	0.5-1.0	0.667	0.367	13.7
	1.0-1.5	1.18	0.0485	5.0
	1.5-2.0	1.69	0.00847	3.6
	2.0-2.5	2.2	0.00183	3.2
	2.5-3.0	2.7	0.000447	2.5
	3.0-3.5	3.21	0.000158	4.7
	3.5-4.0	3.71	5.73e-005	7.3
	4.0-4.5	4.21	2.46e-005	9.1
	4.5-5.0	4.72	9.32e-006	20.3
	5.0-5.5	5.22	3.23e-006	40.5
	5.5-6.0	5.72	1.83e-006	23.3
	6.0-6.5	6.22	9.73e-007	37.9
HighTower-1	4.0-5.0	4.37	1.85e-005	8.0
	5.0-6.0	5.38	3.23e-006	6.4
	6.0-7.0	6.4	8.7e-007	8.3
	7.0-8.0	7.41	1.79e-007	44.6
	8.0-9.0	8.42	7.78e-008	44.7
	9.0-10.0	9.42	2.88e-008	90.2
HighTower-2	5.0-6.0	5.38	4.37e-006	28.8
	6.0-7.0	6.4	8.81e-007	10.9
	7.0-8.0	7.41	2.26e-007	9.2
	8.0-9.0	8.42	7.9e-008	43.8
	9.0-10.0	9.42	3.37e-008	50.6
	10.0-11.0	10.4	1.26e-008	80.6
	11.0-12.0	11.4	4.69e-009	123.0
	12.0-13.0	12.4	2.15e-009	167.0
	13.0-14.0	13.4	5.31e-010	525.0

Table B.2: Fully corrected π^0 yield per minimum-bias-triggered d+Au event. See caption for Table B.1 for details.

APPENDIX C

THE STAR COLLABORATION

J. Adams[3], M.M. Aggarwal[29], Z. Ahammed[43], J. Amonett[20], B.D. Anderson[20],

D. Arkhipkin[13], G.S. Averichev[12], S.K. Badyal[19], Y. Bai[27], J. Balewski[17],

O. Barannikova[32], L.S. Barnby[3], J. Baudot[18], S. Bekele[28], V.V. Belaga[12],

R. Bellwied[46], J. Berger[14], B.I. Bezverkhny[48], S. Bharadwaj[33], A. Bhasin[19],

A.K. Bhati[29], V.S. Bhatia[29], H. Bichsel[45], A. Billmeier[46], L.C. Bland[4], C.O. Blyth[3],

B.E. Bonner[34], M. Botje[27], A. Boucham[38], A.V. Brandin[25], A. Bravar[4],

M. Bystersky[11], R.V. Cadman[1], X.Z. Cai[37], H. Caines[48],

M. Calderón de la Barca Sánchez[17], J. Castillo[21], D. Cebra[7], Z. Chajecki[44],

P. Chaloupka[11], S. Chattopadhyay[43], H.F. Chen[36], Y. Chen[8], J. Cheng[41],

M. Cherney[10], A. Chikanian[48], W. Christie[4], J.P. Coffin[18], T.M. Cormier[46],

J.G. Cramer[45], H.J. Crawford[6], D. Das[43], S. Das[43], M.M. de Moura[35],

A.A. Derevschikov[31], L. Didenko[4], T. Dietel[14], S.M. Dogra[19], W.J. Dong[8],

X. Dong[36], J.E. Draper[7], F. Du[48], A.K. Dubey[15], V.B. Dunin[12], J.C. Dunlop[4],

M.R. Dutta Mazumdar[43], V. Eckardt[23], W.R. Edwards[21], L.G. Efimov[12],

V. Emelianov[25], J. Engelage[6], G. Eppley[34], B. Erazmus[38], M. Estienne[38],

P. Fachini[4], J. Faivre[18], R. Fatemi[17], J. Fedorisin[12], K. Filimonov[21], P. Filip[11],

E. Finch[48], V. Fine[4], Y. Fisyak[4], K. Fomenko[12], J. Fu[41], C.A. Gagliardi[39],

L. Gaillard[3], J. Gans[48], M.S. Ganti[43], L. Gaudichet[38], F. Geurts[34],

V. Ghazikhanian[8], P. Ghosh[43], J.E. Gonzalez[8], O. Grachov[46], O. Grebenyuk[27],

D. Grosnick[42], S.M. Guertin[8], Y. Guo[46], A. Gupta[19], T.D. Gutierrez[7],

T.J. Hallman[4], A. Hamed[46], D. Hardtke[21], J.W. Harris[48], M. Heinz[2], T.W. Henry[39],

S. Hepplemann[30], B. Hippolyte[18], A. Hirsch[32], E. Hjort[21], G.W. Hoffmann[40],

H.Z. Huang[8], S.L. Huang[36], E.W. Hughes[5], T.J. Humanic[28], G. Igo[8], A. Ishihara[40],

P. Jacobs[21], W.W. Jacobs[17], M. Janik[44], H. Jiang[8], P.G. Jones[3], E.G. Judd[6],

S. Kabana[2], K. Kang[41], M. Kaplan[9], D. Keane[20], V.Yu. Khodyrev[31], J. Kiryluk[22],

A. Kisiel[44], E.M. Kislov[12], J. Klay[21], S.R. Klein[21], D.D. Koetke[42], T. Kollegger[14],

M. Kopytine[20], L. Kotchenda[25], M. Kramer[26], P. Kravtsov[25], V.I. Kravtsov[31],

K. Krueger[1], C. Kuhn[18], A.I. Kulikov[12], A. Kumar[29], R.Kh. Kutuev[13],

A.A. Kuznetsov[12], M.A.C. Lamont[48], J.M. Landgraf[4], S. Lange[14], F. Laue[4],

J. Lauret[4], A. Lebedev[4], R. Lednicky[12], S. Lehocka[12], M.J. LeVine[4], C. Li[36],

Q. Li[46], Y. Li[41], G. Lin[48], S.J. Lindenbaum[26], M.A. Lisa[28], F. Liu[47], L. Liu[47],

Q.J. Liu[45], Z. Liu[47], T. Ljubicic[4], W.J. Llope[34], H. Long[8], R.S. Longacre[4],

M. Lopez-Noriega[28], W.A. Love[4], Y. Lu[47], T. Ludlam[4], D. Lynn[4], G.L. Ma[37],

J.G. Ma[8], Y.G. Ma[37], D. Magestro[28], S. Mahajan[19], D.P. Mahapatra[15], R. Majka[48],

L.K. Mangotra[19], R. Manweiler[42], S. Margetis[20], C. Markert[20], L. Martin[38],

J.N. Marx[21], H.S. Matis[21], Yu.A. Matulenko[31], C.J. McClain[1], T.S. McShane[10],

F. Meissner[21], Yu. Melnick[31], A. Meschanin[31], M.L. Miller[22], N.G. Minaev[31],

C. Mironov[20], A. Mischke[27], D.K. Mishra[15], J. Mitchell[34], B. Mohanty[43],

L. Molnar[32], C.F. Moore[40], D.A. Morozov[31], M.G. Munhoz[35], B.K. Nandi[43],

S.K. Nayak[19], T.K. Nayak[43], J.M. Nelson[3], P.K. Netrakanti[43], V.A. Nikitin[13],

L.V. Nogach[31], S.B. Nurushev[31], G. Odyniec[21], A. Ogawa[4], V. Okorokov[25],

M. Oldenburg[21], D. Olson[21], S.K. Pal[43], Y. Panebratsev[12], S.Y. Panitkin[4],

A.I. Pavlinov[46], T. Pawlak[44], T. Peitzmann[27], V. Perevoztchikov[4], C. Perkins[6],

W. Peryt[44], V.A. Petrov[13], S.C. Phatak[15], R. Picha[7], M. Planinic[49], J. Pluta[44],

N. Porile[32], J. Porter[45], A.M. Poskanzer[21], M. Potekhin[4], E. Potrebenikova[12],

B.V.K.S. Potukuchi[19], D. Prindle[45], C. Pruneau[46], J. Putschke[23], G. Rakness[30],

R. Raniwala[33], S. Raniwala[33], O. Ravel[38], R.L. Ray[40], S.V. Razin[12], D. Reichhold[32],

J.G. Reid[45], G. Renault[38], F. Retiere[21], A. Ridiger[25], H.G. Ritter[21], J.B. Roberts[34],

O.V. Rogachevskiy[12], J.L. Romero[7], A. Rose[46], C. Roy[38], L. Ruan[36], R. Sahoo[15],

I. Sakrejda[21], S. Salur[48], J. Sandweiss[48], M. Sarsour[17], I. Savin[13], P.S. Sazhin[12],

J. Schambach[40], R.P. Scharenberg[32], N. Schmitz[23], K. Schweda[21], J. Seger[10],

P. Seyboth[23], E. Shahaliev[12], M. Shao[36], W. Shao[5], M. Sharma[29], W.Q. Shen[37],

K.E. Shestermanov[31], S.S. Shimanskiy[12], E Sichtermann[21], F. Simon[23],

R.N. Singaraju[43], G. Skoro[12], N. Smirnov[48], R. Snellings[27], G. Sood[42],

P. Sorensen[21], J. Sowinski[17], J. Speltz[18], H.M. Spinka[1], B. Srivastava[32],

A. Stadnik[12], T.D.S. Stanislaus[42], R. Stock[14], A. Stolpovsky[46], M. Strikhanov[25],

B. Stringfellow[32], A.A.P. Suaide[35], E. Sugarbaker[28], C. Suire[4], M. Sumbera[11],

B. Surrow[22], T.J.M. Symons[21], A. Szanto de Toledo[35], P. Szarwas[44], A. Tai[8],

J. Takahashi[35], A.H. Tang[27], T. Tarnowsky[32], D. Thein[8], J.H. Thomas[21],

S. Timoshenko[25], M. Tokarev[12], T.A. Trainor[45], S. Trentalange[8], R.E. Tribble[39],

O.D. Tsai[8], J. Ulery[32], T. Ullrich[4], D.G. Underwood[1], A. Urkinbaev[12], G. Van

Buren[4], M. van Leeuwen[21], A.M. Vander Molen[24], R. Varma[16], I.M. Vasilevski[13],

A.N. Vasiliev[31], R. Vernet[18], S.E. Vigdor[17], Y.P. Viyogi[43], S. Vokal[12],

S.A. Voloshin[46], M. Vznuzdaev[25], W.T. Waggoner[10], F. Wang[32], G. Wang[20],

G. Wang[5], X.L. Wang[36], Y. Wang[40], Y. Wang[41], Z.M. Wang[36], H. Ward[40],

J.W. Watson[20], J.C. Webb[17], R. Wells[28], G.D. Westfall[24], A. Wetzler[21], C. Whitten

Jr.[8], H. Wieman[21], S.W. Wissink[17], R. Witt[2], J. Wood[8], J. Wu[36], N. Xu[21], Z. Xu[4],

Z.Z. Xu[36], E. Yamamoto[21], P. Yepes[34], V.I. Yurevich[12], Y.V. Zanevsky[12], H. Zhang[4],

W.M. Zhang[20], Z.P. Zhang[36], R. Zoulkarneev[13], Y. Zoulkarneeva[13], A.N. Zubarev[12]

[1] *Argonne National Laboratory, Argonne, Illinois 60439*

[2] *University of Bern, 3012 Bern, Switzerland*

[3] *University of Birmingham, Birmingham, United Kingdom*

[4] *Brookhaven National Laboratory, Upton, New York 11973*

[5] *California Institute of Technology, Pasadena, California 91125*

[6] *University of California, Berkeley, California 94720*

[7] *University of California, Davis, California 95616*

[8] *University of California, Los Angeles, California 90095*

[9] *Carnegie Mellon University, Pittsburgh, Pennsylvania 15213*

[10] *Creighton University, Omaha, Nebraska 68178*

[11] *Nuclear Physics Institute AS CR, 250 68 Řež/Prague, Czech Republic*

[12] *Laboratory for High Energy (JINR), Dubna, Russia*

[13] *Particle Physics Laboratory (JINR), Dubna, Russia*

[14] *University of Frankfurt, Frankfurt, Germany*

[15] *Institute of Physics, Bhubaneswar 751005, India*

[16] *Indian Institute of Technology, Mumbai, India*

[17] *Indiana University, Bloomington, Indiana 47408*

[18] *Institut de Recherches Subatomiques, Strasbourg, France*

[19] *University of Jammu, Jammu 180001, India*

[20] *Kent State University, Kent, Ohio 44242*

[21] *Lawrence Berkeley National Laboratory, Berkeley, California 94720*

[22] *Massachusetts Institute of Technology, Cambridge, MA 02139-4307*

[23] *Max-Planck-Institut für Physik, Munich, Germany*

[24] *Michigan State University, East Lansing, Michigan 48824*

[25] *Moscow Engineering Physics Institute, Moscow Russia*

[26] *City College of New York, New York City, New York 10031*

[27] *NIKHEF, Amsterdam, The Netherlands*

[28] *Ohio State University, Columbus, Ohio 43210*

[29] *Panjab University, Chandigarh 160014, India*

[30] *Pennsylvania State University, University Park, Pennsylvania 16802*

[31] *Institute of High Energy Physics, Protvino, Russia*

[32] *Purdue University, West Lafayette, Indiana 47907*

[33] *University of Rajasthan, Jaipur 302004, India*

[34] *Rice University, Houston, Texas 77251*

[35] *Universidade de Sao Paulo, Sao Paulo, Brazil*

[36] *University of Science & Technology of China, Anhui 230027, China*

[37] *Shanghai Institute of Applied Physics, Shanghai 201800, China*

[38] *SUBATECH, Nantes, France*

[39] *Texas A&M University, College Station, Texas 77843*

[40] *University of Texas, Austin, Texas 78712*

[41] *Tsinghua University, Beijing 100084, China*

[42] *Valparaiso University, Valparaiso, Indiana 46383*

[43] *Variable Energy Cyclotron Centre, Kolkata 700064, India*

[44] *Warsaw University of Technology, Warsaw, Poland*

[45] *University of Washington, Seattle, Washington 98195*

[46] *Wayne State University, Detroit, Michigan 48201*

[47] *Institute of Particle Physics, CCNU (HZNU), Wuhan 430079, China*

[48] *Yale University, New Haven, Connecticut 06520*

[49] *University of Zagreb, Zagreb, HR-10002, Croatia*

BIBLIOGRAPHY

[1] P. D. B. Collins and A. D. Martin. *Hadron Interactions*. Adam Hilger Ltd, first edition, 1984.

[2] D. E. Groom et al. *Eur. Phys. Journal.*, C15:1, 2000.

[3] J. C. Collins and M. J. Perry. Superdense matter: Neutrons or asymptotically free quarks? *Phys. Rev. Lett.*, 34(777):1353, 1975.

[4] L. Bourhis, M. Fontannaz, J. P. Guillet, and M. Werlen. Next-to-leading order determination of fragmentation functions. *Eur. Phys. J.*, C19:89–98, 2001.

[5] J. Pumplin et al. New generation of parton distributions with uncertainties from global QCD analysis. *JHEP*, 07:012, 2002.

[6] M. L. Miller. *Measurement of Jets and Jet Quenching at RHIC*. PhD thesis, Yale University, 2004.

[7] S. Kretzer. Fragmentation functions from flavour-inclusive and flavour-tagged e^+e^- annihilations. *Phys. Rev.*, D62:054001, 2000.

[8] G. Altarelli and G. Parisi. Asymptotic freedom in parton language. *Nucl. Phys.*, B126:298, 1977.

[9] Yu. L. Dokshitzer. Calculation of the structure functions for deep inelastic scattering and e^+e^- annihilation by perturbation theory in quantum chromodynamics. (in Russian). *Sov. Phys. JETP*, 46:641–653, 1977.

[10] V. N. Gribov and L. N. Lipatov. e^+e^- pair annihilation and deep inelastic ep scattering in perturbation theory. *Sov. J. Nucl. Phys.*, 15:675–684, 1972.

[11] Bernd A. Kniehl, G. Kramer, and B. Potter. Fragmentation functions for pions, kaons, and protons at next-to-leading order. *Nucl. Phys.*, B582:514–536, 2000.

[12] R. Barate et al. Studies of quantum chromodynamics with the ALEPH detector. *Phys. Rept.*, 294:1–165, 1998.

[13] P. Mattig. The structure of jets in e^+e^- collisions. *Phys. Rept.*, 177:141, 1989.

[14] G. Altarelli, R. K. Ellis, G. Martinelli, and So-Young Pi. Processes involving fragmentation functions beyond the leading order in QCD. *Nucl. Phys.*, B160:301, 1979.

[15] P. J. Rijken and W. L. van Neerven. $O(\alpha_s^2)$ contributions to the longitudinal fragmentation function in e^+e^- annihilation. *Phys. Lett.*, B386:422–428, 1996.

[16] D. Buskulic et al. Inclusive $\pi^\pm$, $k^\pm$ and $(p, \bar{p})$ differential cross- sections at the z resonance. *Z. Phys.*, C66:355–366, 1995.

[17] P. Abreu et al. $\pi^\pm$, $K^\pm$, p and $\bar{p}$ production in $Z^0 \to q\bar{q}$, $Z^0 \to b\bar{b}$, $Z^0 \to u\bar{u}$, $d\bar{d}$, $s\bar{s}$. *Eur. Phys. J.*, C5:585–620, 1998.

[18] K. Abe et al. Production of π^+, K^+, K^0, K^{*0}, ϕ, p, and Λ^0 in hadronic Z^0 decays. *Phys. Rev.*, D59:052001, 1999.

[19] J. F. Owens, E. Reya, and M. Gluck. Detailed quantum chromodynamic predictions for high p_t processes. *Phys. Rev.*, D18:1501, 1978.

[20] S. S. Adler et al. Absence of suppression in particle production at large transverse momentum in $\sqrt{s_{NN}} = 200$ GeV d+Au collisions. *Phys. Rev. Lett.*, 91:072303, 2003.

[21] K. Adcox et al. Suppression of hadrons with large transverse momentum in central Au + Au collisions at $\sqrt{s_{NN}}$ = 130 GeV. *Physical Review Letters*, 88, 2002.

[22] K. Adcox et al. Centrality dependence of the high-p_t charged hadron suppression in Au + Au collisions at $\sqrt{s_{NN}}$ = 130 GeV. *Phys. Lett.*, B561:82–92, 2003.

[23] C. Adler et al. Centrality dependence of high-p_t hadron suppression in Au + Au collisions at $\sqrt{s_{NN}}$ = 130 GeV. *Physical Review Letters*, 89, 2002.

[24] S. S. Adler et al. Suppressed π^0 production at large transverse momentum in central Au + Au collisions at $\sqrt{s_{NN}}$ = 200 GeV. *Physical Review Letters*, 91, 2003.

[25] M. Gyulassy and M. Plumer. Jet quenching in dense matter. *Phys. Lett.*, B243:432–438, 1990.

[26] X. N. Wang and M. Gyulassy. Gluon shadowing and jet quenching in A+A collisions at $\sqrt{s_{NN}}$ = 200 GeV. *Phys. Rev. Lett.*, 68:1480–1483, 1992.

[27] M. H. Thoma and M. Gyulassy. Quark damping and energy loss in the high temperature QCD. *Nucl. Phys.*, B351:491–506, 1991.

[28] M. Arneodo et al. Shadowing in deep inelastic muon scattering from nuclear targets. *Phys. Lett.*, B211:493, 1988.

[29] J. W. Cronin et al. Production of hadrons with large transverse momentum at 200-GeV, 300-GeV, and 400-GeV. *Phys. Rev.*, D11:3105, 1975.

[30] J. Adams et al. Evidence from d + Au measurements for final-state suppression of high-p_T hadrons in Au + Au collisions at RHIC. *Physical Review Letters*, 91, 2003.

[31] D. Antreasyan et al. Production of hadrons at large transverse momentum in 200-, 300-, and 400-GeV pp and $p-$nucleus collisions. *Phys. Rev.*, D19:764, 1979.

[32] L. C. Bland. STAR results from polarized proton collisions at RHIC. *hep-ex/0403012*, 2004.

[33] C. Bourrely and J. Soffer. Do we understand the single-spin asymmetry for π^0 inclusive production in p p collisions? *hep-ph/0311110*, 2003.

[34] J. Letessier and J. Rafelski. *Hadrons and Quark-Gluon Plasma.* Cambridge University Press, Cambridge, UK, first edition, 2002.

[35] K. H. Ackermann et al. STAR detector overview. *Nucl. Instrum. Meth.*, A499:624–632, 2003.

[36] M. Anderson et al. The STAR time projection chamber: A unique tool for studying high multiplicity events at RHIC. *Nucl. Instrum. Meth.*, A499:659–678, 2003.

[37] M. Beddo et al. The STAR barrel electromagnetic calorimeter. *Nucl. Instrum. Meth.*, A499:725–739, 2003.

[38] O. Grebenyuk. *Private Communication*, 2004.

[39] C. Adler et al. The RHIC zero-degree calorimeters. *Nucl. Instrum. Meth.*, A461:337–340, 2001.

[40] J. Kiryluk. Relative luminosity measurement in STAR and implications for spin asymmetry determinations. *AIP Conf. Proc.*, 675:424–428, 2003.

[41] E. G. Judd. *Private Communication*, 2004.

[42] R. Brun, R. Hagelberg, M. Hansroul, and J. C. Lassalle. GEANT: Simulation program for particle physics experiments. User guide and reference manual. CERN-DD-78-2-REV.

[43] M. Russcher. *Private Communication*, 2004.

[44] J. Adams et al. Identified particle distributions in p+p and Au+Au collisions at $\sqrt{s_{NN}} = 200$ GeV. *Phys. Rev. Lett.*, 92:112301, 2004.

[45] K. Hagiwara et al. Review of particle physics. *Phys. Rev.*, D66:010001, 2002.

[46] S.S. Bennett et al. The electromagnetic calorimeter and shower maximum detector performance in 1997 testbeam run at BNL, 1997. *STAR NOTE SN-0351* http://www.star.bnl.gov/STAR/sno/ice/sn0351.html.

[47] R. J. Glauber. Cross sections in deuterium at high energies. *Phys. Rev.*, 100:242–248, 1955.

[48] C. Adler et al. Centrality dependence of high p_t hadron suppression in Au+Au collisions at $\sqrt{s_{NN}} = 130$ gev. *Phys. Rev. Lett.*, 89:202301, 2002.

[49] B. Choi. *High p_T Inclusive Charged Hadron Distributions in Au+Au Collisions at $\sqrt{s_{NN}} = 130$ GeV at RHIC*. PhD thesis, University of Texas, 2003.

[50] J. Adams et al. ϕ meson production in Au+Au and p+p collisions at $\sqrt{s_{NN}} = 200$ gev. *Phys. Lett.*, B612:181–189, 2005.

[51] D. Kharzeev, C. Lourenco, M. Nardi, and H. Satz. A quantitative analysis of charmonium suppression in nuclear collisions. *Z. Phys.*, C74:307–318, 1997.

[52] A. Drees and Z. Xu. Results from luminosity scans during the RHIC 2000 run. Presented at IEEE Particle Accelerator Conference (PAC2001), Chicago, Illinois, 18-22 Jun 2001.

[53] J. Adams et al. Transverse momentum and collision energy dependence of high p_t hadron suppression in Au+Au collisions at ultrarelativistic energies. *Phys. Rev. Lett.*, 91:172302, 2003.

[54] B. Jager, A. Schafer, M. Stratmann, and W. Vogelsang. Next-to-leading order QCD corrections to high-p_t pion production in longitudinally polarized p+p collisions. *Phys. Rev.*, D67:054005, 2003.

[55] F. Aversa, P. Chiappetta, M. Greco, and J. P. Guillet. QCD corrections to parton-parton scattering processes. *Nucl. Phys.*, B327:105, 1989.

[56] S. S. Adler et al. Midrapidity neutral-pion production in proton-proton collisions at $\sqrt{s_{NN}} = 200$ gev. *Phys. Rev. Lett.*, 91:241803, 2003.

[57] D. Kharzeev, E. Levin, and L. McLerran. Parton saturation and n_{part} scaling of semi-hard processes in QCD. *Phys. Lett.*, B561:93–101, 2003.

[58] Ivan Vitev. Initial state parton broadening and energy loss probed in d+Au at RHIC. *Phys. Lett.*, B562:36–44, 2003.

[59] A. Accardi. Cronin effect in proton nucleus collisions: A survey of theoretical models. 2002. hep-ph/0212148.

[60] K. Gallmeister, C. Greiner, and Z. Xu. Quenching of high p(t) hadron spectra by hadronic interactions in heavy ion collisions at rhic. *Phys. Rev.*, C67:044905, 2003.

[61] X. N. Wang. Why the observed jet quenching at RHIC is due to parton energy loss. *Phys. Lett.*, B579:299–308, 2004.

[62] B. B. Back et al. Centrality dependence of charged hadron transverse momentum spectra in d+Au collisions at $\sqrt{s_{NN}} = 200$ gev. *Phys. Rev. Lett.*, 91:072302, 2003.

[63] I. Arsene et al. Transverse momentum spectra in Au+Au and d+Au collisions at $\sqrt{s_{NN}} = 200$ gev and the pseudorapidity dependence of high p_t suppression. *Phys. Rev. Lett.*, 91:072305, 2003.

ABSTRACT

NEUTRAL PION PRODUCTION IN p+p AND d+Au COLLISIONS AT RHIC

by

ALEXANDER STOLPOVSKY

December 2005

Advisor: Dr. Thomas M. Cormier

Major: High Energy Nuclear Physics

Degree: Doctor of Philosophy

One of the most interesting results from the Relativistic Heavy Ion Collider (RHIC) at Brookhaven National Laboratory, is the suppression of high transverse momentum (high-p_T) particle production, observed in central Au+Au collisions. This suppression is consistent with theoretical calculations incorporating partonic energy loss via gluon bremsstrahlung in dense QCD matter. d+Au collisions provide an important reference for quantitative description of initial and final state effects on high-p_T particle production.

Neutral pion production in d+Au and p+p collisions at $\sqrt{s_{NN}} = 200$ GeV, measured by the STAR Barrel Electromagnetic Calorimeter, is presented. The p_T dependence of the π^0 yield is measured up to 10 GeV. The yields measured in d+Au are compared to those in p+p collisions, scaled by the average number of nucleon-nucleon collisions in d+Au. The yield ratio does not show the suppression of high-p_T particle production. This suggests that the suppression observed in central Au+Au collisions is due to final-state interactions with the dense medium produced in such collisions.

AUTOBIOGRAPHICAL STATEMENT

4 August, 1977	Born in Protvino Moscow Region, Russia
1995 – 1999	B.S. in Particle Physics Moscow State University Moscow, Russia
1999 – 2005	Graduate Research Assistant High Energy Nuclear Physics Group Wayne State University Detroit, MI, USA